UNIVERSITEIT·STELLENBOSCH·UNIVERSITY
jou kennisvennoot·your knowledge partner

Characterising failure of structural materials using digital images

Author:
Johannes Hendrik Conradie

Supervisors:
Dr. Daniel Z. Turner
Dr. Thorsten H. Becker

A thesis submitted in fulfilment of the requirements for the degree of

Masters of Engineering

Department of Civil Engineering, at Stellenbosch University

March 2015

Declaration of Authorship

By submitting this thesis electronically, I declare that the entirety of the work contained therein is my own, original work, that I am the authorship owner thereof (unless to the extent explicitly otherwise stated) and that I have not previously in its entirety or in part submitted it for obtaining any qualification.

Signed: _____

Date: _____

Abstract

The fracture of ductile materials is currently regarded as a complex and challenging phenomenon to characterise and predict. Recently, a bond-based, non-local theory was formulated called the peridynamic theory, which is able to directly solve solid mechanics problems that include fracture. The failure criterion is governed by a critical stretch relation between bonds. It was found in literature that the critical stretch relates to the popular fracture mechanics parameter called the critical energy release rate for predicting brittle linear-elastic failure. It was also proposed that the non-linear critical energy release rate or J-integral can be used to model ductile failure using peridynamics.

The aim of this thesis was to investigate the validity of using the J-integral to determine the critical stretch for predicting ductile failure. Standard ASTM fracture mechanics tests on Compact Tension specimens of Polymethyl methacrylate, stainless steel 304L and aluminium 1200H4 were performed to determine the critical energy release rates and non-linear Resistance-curves. Furthermore, a novel peridynamic-based algorithm was developed that implements a critical energy release rate based failure criterion and Digital Image Correlation (DIC) measured full surface displacement fields of cracked materials. The algorithm is capable of estimating and mapping both the peridynamic damage caused by brittle cracking and damage caused by plastic deformation. This approach was used to validate the use of an energy release rate based failure criterion for predicting linear-elastic brittle failure using peridynamics. Also, it showed a good correlation among the test results for detecting plastic damage in the alloys when incorporating the respective J-integral derived critical stretch values. Additionally, Modified Arcan tests were performed to obtain Mode I, Mode II and mixed Mode fracture load results of brittle materials. Mode I peridynamic models compared closely to test results when using the Mode I critical energy release rate, derived critical stretch and served as validation for the approach. Moreover, it was argued that Mode I failure criteria cannot in principle be used to model shear failure. Therefore, it was proposed to rather use the appropriate Mode II and mixed Mode critical energy release rates to predict the respective failures in peridynamics. Also, for predicting ductile failure loads it was found that using a threshold energy release rate derived from the R-curve yielded considerably more accurate failure load results compared to the usage of the critical energy release rate, i.e. J-integral.

In this thesis it was shown that there exists great potential for detecting and characterising cracking and failure by using a peridynamic-based approach through coupling DIC full displacement field measurements and the critical energy release rate of a particular structural material.

Opsomming

Duktiele breeking van materiale word tans beskou as 'n kompleks- en uitdagende fenomeen om te voorspel en te karakteriseer. 'n Binding-gebaseerde, nie-lokale teorie is onlangs geformuleer, genaamd die peridinamika teorie. Die laasgenoemde stel ons in staat om soliede meganiese probleme met krake direk op te los. Die falings kriterium word bemagtig deur die kritiese strekfaktor tussen verbindings. Daar was bewys dat die kritiese strekfaktor in verband staan met die populêre breek meganika parameter, genaamd die kritiese vrylatings-energie-koers vir die voorspelling van bros lineêre-elastiese faling. 'n Onlangse verklaring meen dat die kritiese strekfaktor vir duktiele falingsgedrag, bereken kan word met die nie-lineêre kritiese vrylatings-energie-koers, beter bekend as die J-integraal.

Die doel van hierdie tesis was om te meet hoe geldig die gebruik van die J-integraal is om die kritiese strekfaktor te bereken, om sodoende duktiele breking te ondersoek. Standaard ASTM breukmeganika toetse op Polimetilmetakrilat, vlekvrye staal 304L en aluminium 1200H4 is uitgevoer om die kritiese vrylatings-energie-koers en Weerstands-kurwes te bepaal. Verder was 'n nuwe peridinamies-gebaseerde algoritme ontwikkel. Die laasgenoemde implementeer die berekening van 'n kritiese strekfaktor, gebaseer op die kritiese vrylatings-energie-koers, sowel as Digitale Beeld Korrelasie (BDK) vol oppervlaks-verplasings veld metings van gebreekte materiale. Dit is in staat om die peridinamiese skade te bereken, tesame met die beeld wat veroorsaak was van bros krake en plastiese vervorming in duktiele materiale. Hierdie benadering is aangewend om die gebruik van 'n vrylatings-energie-koers gebaseerde falings kriterium vir bros lineêre-elastiese falings in peridinamika te bekragtig. 'n Goeie korrelasie tussen toets resultate is ook gevind vir die opsporing van skade wat veroorsaak is deur plastiese deformasie in die legerings waar die onderskeilike J-integrale gebruik was as falings kriteria. Daarbenewens, was Verandere Arcan toetse uitgevoer om die Modes I, Modes II en gemenge Modes falingsresultate te verkry. Die Modes I peridinamiese model het goed vergelyk met die toetsresultate en het gedien as bekragtiging vir die falingsbenaderings. Verder was dit aangevoer dat Modes I falings kriterium in beginsel nie gebruik kan word om skuiffaling te modelleer nie. Dus was dit voorgestel om eerder die toepaslike Modes II en gemengde Modes kritieke vrylatings-energie-koerse te gebruik om onderskeie falings te voorspel in peridinamiese modelle. Dit was ook gevind dat vir die voorspelling van duktiele falingslaste die drumpel vrylatings-energie-koers, wat verkrygbaar is vanaf die Weerstands-kurwe, aansienlik meer akkurate resultate gee, in vergelyking met die gebruik van die kritiese vrylatings-energie-koers, m.a.w. die J-integraal.

In hierdie tesis was dit gewys dat daar groot potensiaal bestaan vir die opsporing en karakterisering van krake en falings met 'n peridinamies-gebaseerde benadering, deur dit te skakel met BDK vol verplasings veld metings en die kritiese vrylatings-energie-koers van 'n bepaalde strukturele materiaal.

Acknowledgements

The author would like to express his sincere gratitude to his supervisors. Firstly to Dr. Daniel Z. Turner at the Civil Engineering Department of the University of Stellenbosch and Sandia National Laboratories for all the inspiration and motivation to commit to this Master's project. Also, for a scholarship and an exchange internship at the Computer Science Research Institute (CSRI) at Sandia National Laboratories, Albuquerque, NM, USA. Secondly to Dr. Thorsten H. Becker at the Mechanical and Mechatronic Department at Stellenbosch University, who took over as local supervisor, which allowed the project to continue when Dr. Turner returned to Sandia. I am particularly grateful for their combined academic input, advise, enthusiasm and both their example of being both great academic supervisors and outdoor adventurists.

The author would like to express his gratitude to his research group colleagues, Matt Malteno and Melady van Rooyen, for their support, designs, proofreading and friendship. I would also like to thank colleagues Callie van der Merwe and Leroi Pols, who shared many hours of work, laughs and cups of coffee.

The scholarship from the Technology and Human Resources for Industry Proramme (THRIP), the funding from the Institute of Structural Engineering at Stellenbosch for the internship at CSRI, which was an unforgettable experience, and the Eskom Power Plant Engineering Institute (EPPEI) program for their interest in our work, are all gratefully acknowledged. I would also like to thank the Department of Mechanical Engineering and Materials Science at the University of Cape Town for the use of their test facilities and espresso machine. In particular, I would like to thank Nur Mohamed Dhansay for countless hours of invaluable assistance during fatigue cracking specimens. Also, I would like to express my appreciation to the Mechanical workshop team at Mechanical Department of Stellenbosch University for their excellent craftsmanship and practical advise with the manufacture of all the test fixtures.

Finally, I would like to express my sincere gratitude to my family and friends for their love and support. Special mention go to Annemi Conradie for her support and proof read of this thesis.

Contents

List of Figures

List of Tables

Abbreviations

DIC	**D**igital **I**mage **C**orrelation
CZE	**C**ohesive **Z**one **E**lements
FEM	**F**inite **E**lemet **M**ethod
XFEM	e**X**tended **F**inite **E**lemet **M**ethod
MDS	**M**olecular **D**ynamics **S**imulations
LEFM	**L**inear-**E**lastic **F**racture **M**echanics
EPFM	**E**lastic-**P**lastic **F**racture **M**echanics
CTOD	**C**rack **T**ip **O**pening **D**isplacement
CT	**C**ompact **T**ension
SENT	**S**ingle **E**dge **N**otched **T**ension
DENT	**D**ouble **E**dge **N**otched **T**ension
SENB	**S**ingle **E**dge **N**otched **B**end
LVDT	**L**inear **V**ariable **D**ifferential **T**ransducer
MMB	**M**ixed **M**ode **B**ending
DLSP	**D**iagonally **L**oaded **S**quare **P**late
PMMA	**P**oly**m**ethyl **m**ethacrylate
CPU	**C**entral **P**rocessing **U**nit
CCD	**C**harged **C**oupled **D**evice
ZNSSD	**Z**ero **N**ormalised **S**um **S**quared **D**ifference
XDIC	e**X**tended **D**igital **I**mage **C**orrelation
NBG	**N**uclear **B**lock **G**raphite
BSI	**B**ritish **S**tandard **I**nstitute
ISO	**I**nternational **O**rganization for **S**tandardization
ASTM	**A**merican **S**ociety for **T**esting and **M**aterials
ASC	**A**dvanced **S**imulation and **C**omputing
SACAM	**S**outh **A**frican **C**onference on **C**omputational and **A**pplied **M**echanics
EPPEI	**E**skom **P**ower **P**lant **E**ngineering **I**nstitute

Symbols

Symbol	Description	Unit
	General parameters	
ρ	Mass density	kg/m^3
u	Displacement	m
$\ddot{u}$	Acceleration	m/s^2
t	Time	s
x	Position vector	m
	Continuum mechanics parameters	
∇	Divergence or Grad	
σ	Stress	MPa
σ_{ij}	Stress tensor	MPa
σ_{YS}	Von Mises stress	MPa
ϵ	Strain	
ϵ_{ij}	Strain tensor	
b	Body force density	N/m^3
	Peridynamic parameters	
f	Pairwise force function	N/m^3
$\mathscr{H}$	Neighbourhood	
$\mathscr{R}$	Peridynamic body	
x	Particle position under consideration	m
x'	Particle position connected to x within $\mathscr{H}$	m
V	Volume	m^3
$dV_{x'}$	Discrete volume of x'	m^3
T	Force-vector state	N/m^3
ξ	Relative position of two particles	m
η	Relative displacement of two particles	m
s	Stretch	
M	Unit vector in bond direction	m
t	Force scalar state	N/m^4
p	Peridynamic pressure	N/m^2
m	Weighted volume	m^3
e^d	Deviatoric extension	m
ω	Influence function	

θ	Dilatation	
y	Deformed length of bond	m
$\overline{\mu}$	History-dependent scalar value	
c	Micromodulus	N/m
s_c	Critical stretch	

Strength of materials parameters

E	Young's Modulus of Elasticity	GPa
ν	Poisson's ratio	
κ	Bulk modulus	GPa
μ	Shear modulus	GPa

Fracture mechanics parameters

Π	Potential energy	J
$d\Pi$	Change in potential energy	J
U	Strain energy	J
F	Work	J
A	Area	mm^2
B	Specimen thickness	mm
W	Specimen width	mm
b_o	Remaining material ahead of crack length	mm
a	Crack length	mm
a_c	Critical crack length	mm
da	Change in crack length	mm
R-curve	Resistance curve	J/mm^2
r	Radius from crack	mm
θ	Angle of r	rad
f_{ij}	Dimensionless function of θ	
g_{ij}	Dimensionless function of θ for higher order terms	
A_m	Geometry dependent higher order term	
K	Stress intensity factor	$MPa\sqrt{m}$
ΔK	Change in Stress Intensity Factor	$MPa\sqrt{m}$
ΔK_{th}	Change in threshold stress intensity factor	$MPa\sqrt{m}$
K_I	Stress intensity factor Mode I	$MPa\sqrt{m}$
K_{II}	Stress intensity factor Mode II	$MPa\sqrt{m}$
K_{III}	Stress intensity factor Mode III	$MPa\sqrt{m}$
K_c	Fracture toughness	$MPa\sqrt{m}$
K_{Ic}	Fracture toughness Mode I	$MPa\sqrt{m}$
K_{IIc}	Fracture toughness Mode II	$MPa\sqrt{m}$
G	Energy release rate	J/m^2
G_c	Critical Energy Release Rate	J/m^2
G_I	Energy release rate Mode I	J/m^2
G_{Ic}	Critical energy release rate Mode I	J/m^2
G_{IIc}	Critical energy release rate Mode II	J/m^2
J	Non-linear energy release rate	J/m^2
J_{Ic}	Critical non-linear energy release rate Mode I	J/m^2
J_{IIc}	Critical non-linear energy release rate Mode II	J/m^2
J_{el}	Elastic J	J/m^2

J_{pl}	Plastic J	J/m^2
J-integral	Critical non-linear energy release rate	J/m^2
w	Strain energy density	J/m^3
ds	Length increment	m
$\partial u_i/\partial x$	Change in length	m
Γ	Crack contour	
n_j	Vector normal to Γ	
N	Load cycles	
dN	Change in load cycles	
P_{max}	Maximum failure load	N
C	Compliance	mm/N
A_{pl}	Plastic area	mm^2
η	Dimensionless geometry constant	
γ	Dimensionless geometry constant	

Digital image correlation parameters

u	Displacement in x	mm
v	Displacement in y	mm
Δx	Change in x	mm
Δy	Change in y	mm
$\partial u/\partial x$	Gradient of x in x-direction	
$\partial u/\partial y$	Gradient of y in x-direction	
$\partial v/\partial x$	Gradient of x in y-direction	
$\partial v/\partial y$	Gradient of y in y-direction	
C_{ij}	Pixel correlation coefficient	
F	Reference greyscale pixel intensity value	
G	Deformed greyscale pixel intensity value	
$\overline{F}$	Average reference greyscale pixel intensity value	
$\overline{G}$	Average deformed greyscale pixel intensity value	

Dedicated to

Rita Conradie (10/11/1923 - 5/6/2014) and
Gerhard Roux (2/11/1932 - 12/10/2014).

Chapter 1

Introduction

Ductile failure is a complex and challenging phenomenon to characterise and predict. Designing new structures and components using new types of alloys as structural material typically requires material testing to characterise the behaviour and estimate at what point the material will yield or fail. However, an impediment of experimental evaluation is that it can be complex and expensive. Materials and test facilities are not always available and at the disposal of the experimentalist. Hence, numerical analyses are resorted to for estimating engineering problems with limited knowledge of the particular behaviour of a material (Boyce et al., 2011). However, relating the experimental and numerical analyses are often oversimplified and difficult. This is where full surface field measurements play an essential role of bridging the gap (Roux and Hild, 2006). The popular non-contact method called Digital Image Correlation (DIC) allows full kinematic field measurements using a series of digital images from an undeformed to a deformed surface of a material. This presents a powerful tool for experimentally characterising failure and further allows for post-processing using numerical methods to determine failure properties (McNeil et al., 1987).

Typically classical continuum mechanics and the Strength of Materials approach are used to model structures and estimate at what loads the structural materials will yield. However, when the problem arises to predict crack initiation or estimate whether an existing crack is stable in a structure, these methods are inherently incapable of predicting failure (Hjelmstad, 2005). The field of fracture mechanics was thus developed to allow one to characterise an existing crack with the knowledge of the fracture toughness of

a material, which is regarded as a material property (Anderson, 2005). The fracture toughness of ductile materials can be determined with standardised tests in accordance with the British Standard Institute (BSI), International Organization for Standardization (ISO) or American Society for Testing and Materials (ASTM).

Initial development of linear-elastic fracture mechanics (LEFM) used an energy release approach developed by Irwin (1956). Thereafter, a single parameter was developed that describes the displacements and stresses around a crack tip. This is called the stress intensity factor, K, which relates to the energy release rate (Irwin, 1957). However, for ductile materials in particular it is not always possible to characterise the fracture behaviour using LEFM due to the non-linear plastic behaviour. Henceforth, elastic-plastic fracture mechanics (EPFM) was introduced, where the essential parameter called the J-integral was developed by Rice (1968). The J_{Ic} is also regarded as the fracture toughness of a material and is used to characterise the non-linear critical elastic energy release rate of a material and can be determined with standardised tests for Mode I normal failure.

In contrast to standardised experimental evaluation, numerical modelling of cracking is currently regarded as a complex problem. Especially with classical continuum mechanics, where the constitutive formulation is based on spatial partial derivatives, which is inherently incapable of solving discontinuities. Methods such as the extended Finite Element Method (XFEM) (Belytschko and Black, 1999) and Cohesive Element Method (CEM) (Hillerborg et al., 1976) have been developed to address this problem. However, these methods require external crack growth criteria and the location of the crack. Recently, an alternative method was developed called the peridynamic theory, which is a reformulation of continuum mechanics (Silling, 2000). As opposed to using spatial partial derivatives, an integral formulation is used. This allows the direct application of crack modelling without external criteria or knowledge of the crack position. Peridynamics have been successfully used to analyse fracture in brittle materials, such as concrete and graphite (Askari et al., 2006, Gerstle, Sau and Aguilera, 2007, Ha and Bobaru, 2011).

In peridynamics, a solid is represented by particles, which are connected to other distant particles within a material radius, called the horizon, therefore the theory is classified as non-local. On loading of a peridynamic material the bonds between particles stretch

and the forces within the bonds reach equilibrium. Moreover, when bonds exceed a critical stretch value the bonds are irreversibly broken. The critical stretch was related to a measurable quantity by considering the energy required to break all bonds between two brittle material spheres (Silling and Askari, 2005). This energy was related to the same critical energy release rate found in LEFM, where the K_{Ic} value was used to determine the critical stretch (Foster et al., 2011). Simulations using this relationship have shown potential in modelling linear-elastic brittle cracking (Madenci and Oterkus, 2014). At this point in time, however, modelling ductile failure in peridynamics presents a complex problem. This was recently experienced in the ductile failure X-price held by Sandia National Laboratories, funded by Advanced Simulation and Computing (ASC) (Boyce et al., 2011). The subject of the exercise was to test the computational capabilities of several numerical methods in simulating ductile failure. The intent was identifying key aspects of discrepancy of the particular numerical methods and to carry fracture-modeling capabilities forward. It was found that peridynamics was incapable of simulating accurate failure loads when providing the K_{Ic} of the particular alloys under consideration. It was argued that the impediment was due to using a linear-elastic failure criterion for describing elastic-plastic failure. It was stated that using a J_{Ic} value would be more appropriate (Boyce et al., 2011). Foster et al. (2011) also argued that if the J_{Ic} is possessed, it can be used as input in order to model elastic-plastic failure in a straightforward manner. However, Madenci and Oterkus (2014) recently stated: "*For complex material behavior, there is no simple approach for determining the critical stretch or critical energy*".

The aim of this thesis is to show that the critical non-linear energy release rate, i.e. J_{Ic}, can be obtained from standard fracture mechanics tests and be used to determine the critical stretch, which can be used to predict ductile failure loads. Also, it is planned to validate the energy based failure criterion to determine the critical stretch for linear-elastic brittle materials, as proposed by Foster et al. (2011).

Furthermore, a novel peridynamic-based algorithm is presented here. The algorithm implements full field surface displacements obtained from Digital Image Correlation (DIC) analyses of digital images of cracked materials. It was found that the full displacement fields naturally fitted the peridynamic material points and allowed for accurately detecting and mapping cracks. Initial work has shown great potential for brittle crack

detection of Nuclear Block Graphite (NBG) (Conradie et al., 2014). The aim is to further develop the algorithm and implement the J_{Ic} derived critical stretch for mapping crack damage of brittle materials and detect damage caused by plastic deformation in ductile materials.

1.1 Background

This thesis is for the fulfillment of a masters degree in structural engineering at the University of Stellenbosch. The project was funded by the Technology and Human Resources for Industry Programme (THRIP). Also, this work relates to interests of the Eskom Power Plant Engineering Institute (EPPEI) Program. The program was establish to serve as a platform between Eskom and South African Universities, with the intent to strengthen the competence in key aspects currently of concerned in power plants (*Eskom EPPEI*, 2014). This work relates through establishing experimental techniques using non-intrusive measuring techniques such as DIC to charaterise material degradation caused by cracking. Furthermore, relating numerical methods with the experimental evaluation through full field measurements and obtaining modelling input properties are of interest.

1.2 Project scope

This thesis sets out to perform fracture experiments to obtain the critical energy release rates required to determine the critical stretch values of brittle and ductile materials required as input for peridynamic modelling. The results are projected to validate the critical energy based failure criterion for modelling linear-elastic brittle failure and the validity of implementing a non-linear critical energy release rate, i.e. J_{Ic} for modelling ductile failure.

It is also planned to acquire digital images of the cracked surfaces of the materials during testing. The images will subsequently be used for DIC anaylses to determine the full displacement fields of the cracked materials to implement in the peridynamic-based algorithm. Through further development of the algorithm, it is aimed to qualitatively validate the critical energy release rate derived critical stretch. In other words, the focus

was on predicting and mapping the crack path using the peridynamic-based algorithm from the full field displacement measurements and using the critical energy release rate as input.

1.3 Thesis layout

The following chapter provides a general literature review on the peridynamic theory, fracture mechanics and DIC method. Background information and formulations are provided. Chapter 3 defines the hypothesis, the motivation and provides specific objectives. Chapter 4 and 5 provides the experimental methods and results, respectively. Chapter 6 presents the peridynamic modelling and results. The respective results are discussed in each chapter. However, Chapter 7 provides further discussions on the key aspects found in the subsequent chapters and respective recommendations for future work are provided. Chapter 8 is the concluding chapter. The reference list follows the final chapter and Appendix A contains the design drawings of the test specimens and fixtures.

Chapter 2

Literature Review

This chapter provides a literature review of numerical and experimental mechanics that are relevant to characterising the cracking behaviour of materials. The chapter begins by introducing numerical solid mechanics, where background on failure analysis of classical continuum mechanics is discussed. The following section introduces the peridynamic theory, where the background, formulations and failure models are discussed, particularly in the application of material cracking behaviour and failure criteria. Thereafter, the well established field of fracture mechanics is covered, where the different approaches and experimental methods thereof are given. The link between peridynamics and experimental fracture mechanics is also made evident, where both relate through a critical energy release rate. The standards and experimental methods to determine fracture mechanics failure parameters for elastic and elastic-plastic materials are discussed. Furthermore, mixed Mode testing methods are discussed, where the advantages of using the Modified Arcan test are given.

The final section is focused on Digital Image Correlation (DIC), where the background and advantages of full field measurements above conventional experimental techniques are given. Furthermore, the basic principles of the method, specimen preparation and test conditions are discussed. Thereafter, DIC methods for failure analysis and inherent limitations of crack measurement with DIC are discussed.

Finally, conclusions are drawn from previous studies where peridynamics and fracture mechanics have been successfully used in material cracking models. Test standards and experimental methods for characterising cracking behaviour are identified. Lastly, the

DIC method is identified as the essential bridge to the gap between experimental and numerical mechanics.

2.1 Classical continuum mechanics and crack modelling

In classical continuum mechanics a body is defined to be in equilibrium through the balance of external and internal forces. Internally, all materials are made up of elementary particles, which are held together by molecular bonds. When a body is loaded, these bonds stretch and particles are allowed to move relative to one another. The relative movement of particles at the microscopic level is observed as macroscopic deformation. Continuum mechanics captures the macroscopic behaviour resulting from the interaction of particles at the microscopic level with the intent to homogenise the whole material behaviour. The mathematical framework that covers a whole class of material behaviours, with the distinction of only changing material properties, is generally referred to as constitutive modelling. Among these classes are elastic and plastic material behavioural models.

Modelling constitutive behaviour in classical mechanics occurs on a local level, where the stress at a point depends upon the strain at a point. The constitutive models give useful results that are widely used in the engineering community. There are, however, several limitations such as modelling highly concentrated deformations causing strain localizations and discontinuities such as cracks (Hjelmstad, 2005). One resolution mentioned by Hjelmstad is to extend the locality from a single point to a neighbourhood of a point. The classical theory is formulated with spatial partial derivatives. This is illustrated with the Cauchy equation of motion as:

$$\rho\ddot{u}[x,t] = \nabla\sigma[x,t] + b[x,t] \tag{2.1}$$

where, ρ is mass density, $\ddot{u}$ is acceleration, where the displacement vector is twice derived with respect to time, $\nabla\sigma[x,t]$ is the divergence of the stress tensor, which is a symmetric second-order tensor commonly called the first Piola-Kirchoff stress tensor. The stress tensor consists of partial derivatives of displacement. b is a body force density, x is a position vector in the reference configuration and t is time.

The partial derivatives cannot hold when discontinuities appear in the displacement field and special techniques are required to address this issue. Special techniques include using Cohesive Zone Elements (CZE), where cracks in materials are modelled through a traction-separation law, when the opening displacement or separation reaches a critical value the tractions are zero (Hillerborg et al., 1976). Another method developed in the realm of the Finite Element Method (FEM), called eXtended Finite Element Method (XFEM), which involves modelling crack growth without requiring re-meshing. It uses additional degrees of freedom, which capture the displacement discontinuity across a crack (Belytschko and Black, 1999). The problem with these techniques is that external criteria for crack growth prediction and modelling are required. Some of the problems encountered in continuum mechanics can be overcome by using atomistic lattice models or Molecular Dynamics Simulations (MDS), the atomic models are the most detailed and realistic for predicting fracture (Schlangen and van Mier, 1992). However, due to the degree of detail and the amount of atoms in a model, the simulations are computationally expensive.

Damage Mechanics can be applied to determine the energy dissipation within a material (Lemaitre, 1971, 1984), however, it was found that strain-softening caused strain localization with finite element solutions (Belytschko et al., 1986). Non-local damage theory, which is based on finite elements, have been applied by averaging the energy release rate within a characterising length coinciding with the center of each element. However, formulations from non-local damage theory are inherently incapable of characterising the entire material degradation process until complete failure (Pijaudier-Cabot and Bazant, 1987).

2.2 The peridynamic theory

The peridynamic theory is a relatively new theory formulated by Silling (2000) and is derived from classical continuum mechanics. As opposed to using spatial partial derivatives to determine stresses and strains within a body, an integral formulation is used to determine displacements and forces within a body. The integral formulation allows peridynamics to solve for discontinuities, such as cracks. Numerous problems involving crack initiation and propagation have been accurately modelled. The dynamic fracture and crack branching of brittle materials were accurately simulated compared to

experiments (Ha and Bobaru, 2011). Peridynamics has also been successfully applied to simulating material and structural failure of composites, mainly graphite-epoxy laminates, where the crack direction and failure Mode were predicted (Askari et al., 2006). The method has also been successful in modeling cracking in concrete structures (Gerstle, Sau and Silling, 2007) and paired with conventional finite element methods to aid in the regions where cracking occurred (Gerstle, Sau and Aguilera, 2007). Furthermore, multiscale material behaviour and failure were effectively modelled, such as the fracture behaviour of polycrystals and nanofiber networks. Peridynamics is ideally suited to describing damage propagation with the advantage of modeling crack propagation without the knowledge of the crack path (Askari et al., 2008). The successful implementation of peridynamics for failure modelling motivates further study in its application in characterising structural failure.

Peridynamics is a non-local theory, where particles have an influence on other non-connecting distant particles within a radius known as the material horizon, which has many similarities to MDS (Seleson et al., 2009). The balance of forces is between the applied loading and forces developed between particles. Particles are connected by bonds within the horizon and the relationship between bond forces and extension is characterised by a micromodulus. The classical formulation can be recovered as the horizon shrinks to zero (Bobaru et al., 2009).

Figure 2.1 illustrates a peridynamic body and the influence of a particle x on neighbouring particles x' within the horizon. Between every infinitesimally small particle x and x' a force density function exists, called the pairwise force function. There is a reaction if the particles are within the material horizon. The pairwise force function is a function of the relative displacements between the interacting particles and the relative position of the particles. The original form of the peridynamic model, which is called the bond based theory, uses a two-particle force function f to describe the interaction between material particles (Silling, 2000):

$$\rho\ddot{u}[x,t] = \int_{\mathscr{H}} f(u[x',t] - u[x,t], x' - x)dV_{x'} + b[x,t] \tag{2.2}$$

where $\mathscr{H}$ is the neighbourhood of a particle x, u is the displacement vector field, b is a prescribed body force density field, ρ is the mass density in the reference configuration and f is a pairwise force function whose value is the force vector (per unit volume

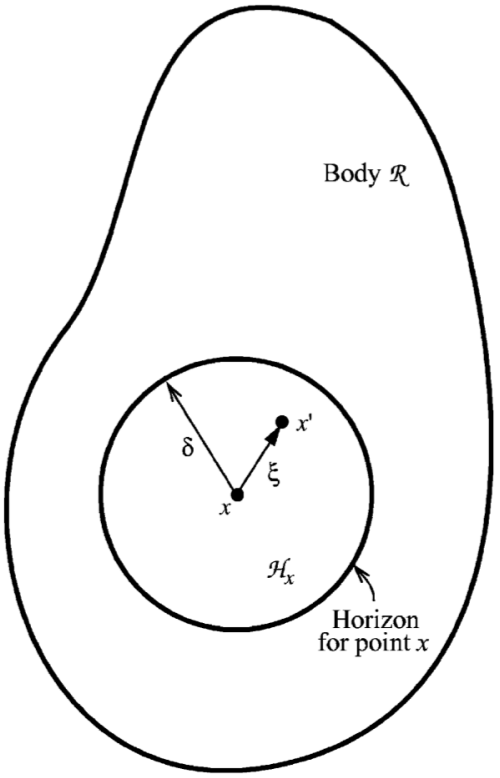

FIGURE 2.1: Peridynamic body $\mathscr{R}$, where a point x interacts with each point x' within the material horizon (Silling and Askari, 2005)

squared) that the particle x' exerts on the particle x (see Figure 2.2). When a load is applied to a body all the particles rearrange relative to each other to account for the internal forces to remain in equilibrium. The relation to the classical theory can be seen that the divergence of the stress tensor term on the left of Equation 2.1 is substituted with the integral of the pairwise force function between particles.

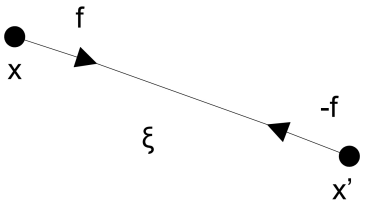

FIGURE 2.2: Pairwise forces of two particles

The original formulation shown in Equation 2.2 has a few shortcomings. Firstly, it is an oversimplification assuming that any pair of particles interact through a central force potential, which is independent of all other local conditions. An isotropic linear material

will effectively have a Poisson's ratio of $\frac{1}{4}$. Another shortcoming is the requirement to alter the constitutive material behaviour in terms of a pairwise force function, when in classical mechanics material behaviour is formulated in terms of a stress tensor. To address these issues the original equation was reformulated. This new formulation is called state-based peridynamics (Silling et al., 2007):

$$\rho\ddot{u}[x,t] = \int_{\mathscr{H}} \underline{T}[x,t]\left\langle x'-x\right\rangle - \underline{T}[x',t]\left\langle x-x'\right\rangle dV_{x'} + b[x,t] \tag{2.3}$$

where $\underline{T}$ is the peridynamic force-vector state and all the other definitions hold from Equation 2.2. The concept of a force-vector state is similar to that of a stress tensor, where both map vectors of vectors. A force-vector state consists of force densities, which exist between particles, the $\langle\rangle$ brackets indicate the vector on which the state operates and the desired force state can be extracted from the corresponding initial relative position vector (Madenci and Oterkus, 2014). The state based formulation allows for neighbouring bonds to interact and resolves the previously mentioned issues (Foster et al., 2009).

Within a continuum there exists infinite particles, therefore in order to solve engineering problems Equation 2.3 is simplified by discretizing a body into a finite amount of particles. Hence, the integral can be replaced with a finite sum. This is mathematically expressed as:

$$\rho\ddot{u}[x,t] = \sum_{j=1}^{k} \underline{T}[x_i,t]\left\langle x_i-x_j\right\rangle - \underline{T}[x_j,t]\left\langle x_i-x_j\right\rangle dV_j + b[x_i,t] \quad \forall i = 1,2,\ldots,\mathscr{N} \tag{2.4}$$

where x_i is a node or material particle under consideration, x_j is a node within the material horizon $\mathscr{H}$, k is the total number of nodes in $\mathscr{H}$, V_j is the volume of node x_j, and $\mathscr{N}$ is the total number of nodes in the body.

The relative position of two nodes in the reference configuration is defined as:

$$\xi = x' - x \tag{2.5}$$

The relative displacement:

$$\eta = u(x',t) - u(x,t) \tag{2.6}$$

$\eta - \xi$ represents the current relative position vector connecting nodes and the interaction between nodes is called a bond, which has a elastic interaction like a spring (Maceka and Silling, 2007). With Equation 2.5 and Equation 2.6 the extension or stretch, s of a bond can be calculated with the relative position vector between two nodes with:

$$s = \frac{\mid \eta + \xi \mid - \mid \eta \mid}{\mid \eta \mid} \tag{2.7}$$

2.2.1 Linear-elastic peridynamic material

In a linear-elastic isotropic peridynamic material the force acting on the bond between two particles is given by:

$$\underline{T} = t\underline{M} \tag{2.8}$$

where $\underline{M}$ is a unit vector pointing in the direction of the bond between x and x'. The force scalar state of a linear-elastic peridynamic material is formulated by:

$$t = \frac{-3p}{m}\omega x + \beta \omega e^d \tag{2.9}$$

where t is the force scalar state with force per unit volume squared, $p = -k\theta$ is the peridynamics pressure, x is the reference position, e^d is the deviatoric extension, ω is an influence function, m is the weighted volume, θ is the dilatation, k and $\beta = 15\mu/m$ are material parameters, where k is the bulk modulus and μ is the shear modulus. The diviatoric extension e^d can be expressed as:

$$e^d = e - \frac{\theta x}{3} \tag{2.10}$$

where $e = y - x$ and y is the particle position connected to x within the horizon.

2.2.2 Peridynamic failure model

As previously noted, in classical continuum mechanics special techniques and crack growth criteria are needed when discontinuities appear in a displacement field, due to the fact that a gradient does not exist over a discontinuous function. However, as a

result of the integral formulation in peridynamics, a function containing a discontinuity can be accurately captured. This advantage allows the same formulation to be applied on continuous and discontinuous displacement fields. In other words, peridynamics can naturally solve problems where cracks form and propagate without resorting to special criteria or knowledge of the location of crack nucleation.

Damage is incorporated in peridynamics by allowing bonds between nodes to irreversibly break. When a bond extends beyond a critical stretch, s_c, it regarded as broken. The forces are redistributed through the surrounding intact bonds. To illustrate this, consider the simplified force-extension relationship defined by:

$$f(\xi, \eta, t) = \overline{\mu}(\xi, \eta, t) sc \tag{2.11}$$

where c represents a spring constant or micromodulus of a bond and $\overline{\mu}(\xi, \eta, t)$ is a history-dependent scalar-valued function of boolean value that indicates the integrity of the bond (Silling and Bobaru, 2005):

$$\overline{\mu}(\xi, \eta, t) = \begin{cases} 1 & \text{if } s \leq s_c \\ 0 & \text{if } s > s_c \end{cases} \tag{2.12}$$

where a value of 1.0 indicates an intact bond and 0 a broken bond. A broken bond can no longer distribute tensile force and the onset of broken bonds causes material softening at a point. Moreover, the coalescence of broken bonds represent a fracture surface. Peridynamic damage can be expressed as:

$$D = \frac{\text{number of broken bonds}}{\text{initial bonds}} \tag{2.13}$$

where zero damage is pristine material and damage of 1.0 is complete disconnection of all bonds to a node, however damage of 0.5 and higher would indicate that a fracture surface has formed. The critical stretch can be related to a measureable value by considering a planar crack in a homogeneous body and to form this crack requires breaking all the bonds that originally connected the two halves of the body. Bond breakage can be related to the amount of energy required to create a new crack surface. The amount of

work required to break one bond is given as:

$$w(\xi) = \int_0^{s_c} sc\xi ds, \quad \xi = \mid \xi \mid \tag{2.14}$$

where the relationship $d\eta = \xi ds$ is used. The work, G_c required to create a new crack surface and break all the bonds connecting the two halves of material is expressed as (Silling and Askari, 2005) (refer to Figure 2.3 for the explanation of the formulation):

$$G_c = \int_0^{\delta} \int_0^{2\pi} \int_z^{\delta} \int_0^{\cos^{-1} z/\xi} (cs_c^2 \xi/2)\xi^2 \sin\phi d\phi d\xi d\theta dz \tag{2.15}$$

For every point A along the dashed line $0 \leq z \leq \delta$ the amount of work needed to break a bond connecting A to each node B in the spherical cap is summed by Equation 2.15 by using a spherical coordinate system with A as origin.

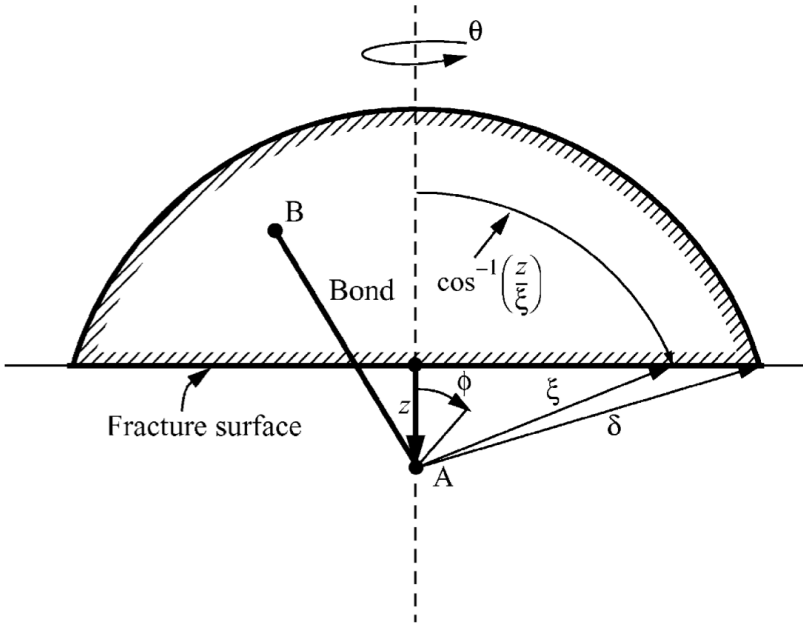

FIGURE 2.3: Evaluation of fracture energy, G_c (Silling and Askari, 2005)

The critical stretch can now be determined from G_c, also known as the critical energy release rate, by solving the integral in Equation 2.15 (the formulation for three dimensions and two dimensions are given) (Madenci and Oterkus, 2014):

$$s_c = \begin{cases} \sqrt{\dfrac{G_c}{(3\mu + (\frac{3}{4})^4(\kappa - \frac{5\mu}{3}))\delta}} & \text{three dimensions} \\ \sqrt{\dfrac{G_c}{(\frac{6}{\pi}\mu + \frac{16}{9\pi^2}(\kappa - 2\mu))\delta}} & \text{two dimensions} \end{cases} \tag{2.16}$$

The relationship provides the critical stretch for a brittle linear-elastic material. The critical energy release rate can be related to crack tip stress singularities or stress intensity factors from the well-established field of fracture mechanics, which will be discussed in the following section. As mentioned, peridynamics does not require any prior crack knowledge such as crack tip stress singularities, thus it is counter-intuitive resorting to classical fracture mechanics, however, to date peridynamics lacks experimental methods of determining critical stretch values. Fracture mechanics standard tests can be performed to determine failure properties with guidance from design standards. Consequently, for more complex material behaviour there does not exist a simple approach for determining the critical stretch (Foster et al., 2011, Madenci and Oterkus, 2014). The peridynamic theory is still in an early stage of development and implementation, and predicting, for example ductile tearing of metals is still as challenging as with other techniques, as found in the ductile failure x-prize held by Sandia National Laboratories (Boyce et al., 2011).

Validation tests were performed through testing the applicability of the critical stretch determined from fracture mechanics properties, i.e. K_{IC}. The tests showed good qualitative comparisons with numerical simulations compared to camera data and served as validation that a single K_{IC} value can be used as input for the failure model (Foster et al., 2011). However, the tests were lacking because strain gauges were used to measure displacements in front of the crack. The crack would propagate and break the strain gauge, which lead to erroneous measurements. This gives motivation to use better means of displacement measurements especially near crack tips, such as non-contact methods like DIC, which will be further discussed in this chapter.

Further tests were performed investigating different failure Modes (Mode I, II and mixed Mode loading, which will be discussed in the following section) and simulating the tests with peridynamics. The failure loads and the crack propagation paths were compared to the tests, where it was found that the crack growth initiations showed good comparison with the tests. The failure loads from the peridynamic simulations were within 15% the experimental results for all the crack inclination angles. Mode I and Mode II compared closely to the tests, however, the mixed Mode failure loads were higher in the simulations. Reasons for the discrepancies could be due to specimen preparation, where the specimens did not have sufficiently sharp cracks (Ayatollahi and Aliha, 2009, Madenci and Oterkus, 2014). The tests showed that there exists a close correlation between the peridynamic

simulation and the experiments, which further served as validation to determine the critical stretch with fracture mechanics failure properties.

2.3 Overview of fracture mechanics

The following section is focused on the field of fracture mechanics, its development, the design and analysis approach, and the ways in which it is used to evaluate cracking in different materials. Fracture mechanics is a well-established field and numerous publications, books and standards are available. The mechanics of fracture and cracking became an engineering discipline after the infamous failure of welded Liberty ships during World War II, where most failures where caused by cracks initiating at square hatch corners on the decks, which created local stress concentrations. Research done by Irwin (1956) led to the development of the energy release rate approach, which Griffith (1921) first proposed by analysing an applied stress to an elliptical hole that cracked and unstably propagated. The tests that Griffith analysed were performed by Inglis (1913). The theory suggests that crack growth occurs from an unstable flaw in a material when the strain energy is sufficient to overcome the surface energy of the material. Development was made on stress and displacement analysis ahead of sharp crack tip (Westergaard, 1939), which led to the approach that the stresses and displacement near a crack tip can be described by a single parameter that is related to the energy release rate, called the stress intensity factor, as stated by Irwin (1957).

In the conventional design approach based on traditional strength of materials, a material is assumed adequate when the strength of the material is greater than the applied stress. Fracture mechanics is based on the three factors: the applied stress; flaw size (crack); and the fracture toughness (critical stress intensity factor). Figure 2.4 illustrates this relationship. The critical combination of these parameters is quantified and when exceeded the crack will propagate and the material will fail.

There are two approaches in fracture mechanics analysis, i.e. the energy criterion and the stress intensity approach, where these two approaches relates in certain conditions. As previously mentioned, peridynamics can be related to the critical energy release rate for determining the critical stretch and it is therefore of importance to understand the

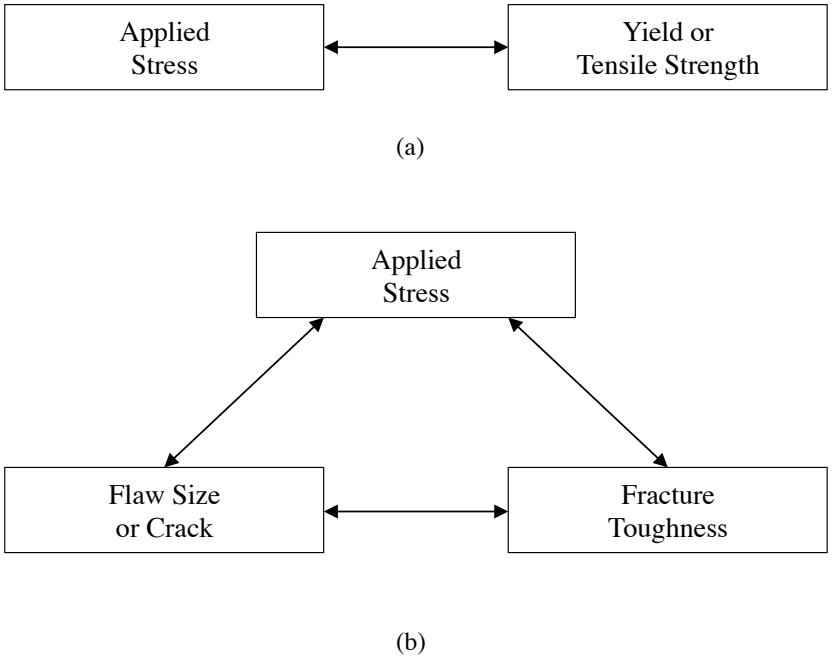

FIGURE 2.4: Comparison of strength of materials to fracture mechanics design approach: (a) Strength of materials approach and (b) fracture mechanics approach.

energy criterion in fracture mechanics, how it relates to the stress intensity approach and how it can be experimentally determined.

2.3.1 Energy criterion

The energy criterion states that a crack will propagate when the energy required for crack growth is sufficient to exceed the material resistance. The material resistance can include plastic work, surface energy, or other types of energy dissipation related to crack propagation (Griffith, 1921).

The present version of the energy approach uses the energy release rate, G, which describes the global material behaviour and quantifies the total change in potential energy of crack extension of a linear elastic material. The energy required for an increment of crack extension can be expressed as:

$$G = -\frac{d\Pi}{dA} \tag{2.17}$$

where $d\Pi$ is the change in potential energy in an elastic body, where $\Pi = U - F$, U is the strain energy stored in the body, F is the work done by external forces and dA is the change in area. The moment fracture occurs the energy release rate is equal to the critical energy release rate, G_c, and is a measure of the fracture toughness (Irwin, 1956). The energy release rate for an infinite plate with crack length $2a$, as illustrated in Figure 2.5, is given by:

$$G = \frac{\pi\sigma^2 a}{E} \tag{2.18}$$

where E is Young's Modulus of Elasticity, σ is applied stress and a is half the crack length.

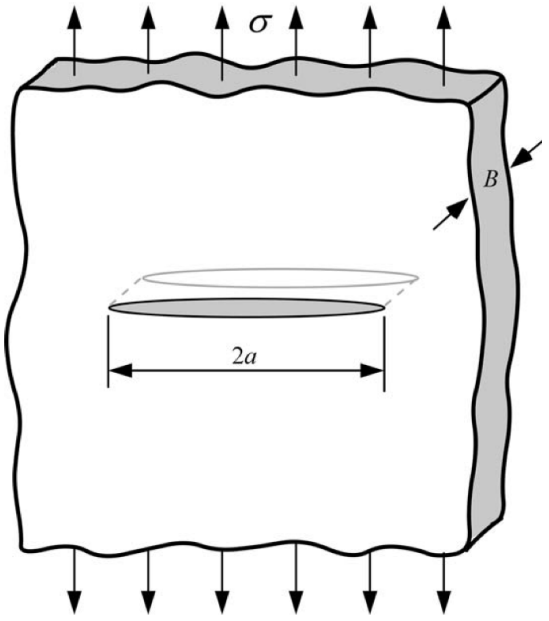

FIGURE 2.5: Through thickness crack in infinite (plate width >> $2a$) plate subjected to tensile stress (Anderson, 2005).

When fracture occurs $G = G_c$ and the critical combinations of flaw size and stress for failure is described as:

$$G_c = \frac{\pi\sigma^2 a_c}{E} \tag{2.19}$$

where a_c is the critical crack length before fracture. A fundamental assumption of fracture mechanics is that the fracture toughness or G_c rate measured from an experiment

can be applied to a structure, however, it is only valid as long as the material behaviour stays predominantly linear elastic.

2.3.2 Resistance curves

To characterise the crack behaviour of a material the resistance curve or R-curve is commonly used, which is a plot of R versus crack extension, where R is the resistance of a material to crack extension. Brittle materials have a horizontal R-curve, where the material resistance stays constant with crack extension. The crack remains stable when the applied stress is σ_1 and when the stress is σ_2 crack is unstable and fracture occurs, as illustrated in Figure 2.6(a). In the case of a flat R-curve a single critical value of energy release rate can be defined, which characterises the crack behaviour of a linear elastic material.

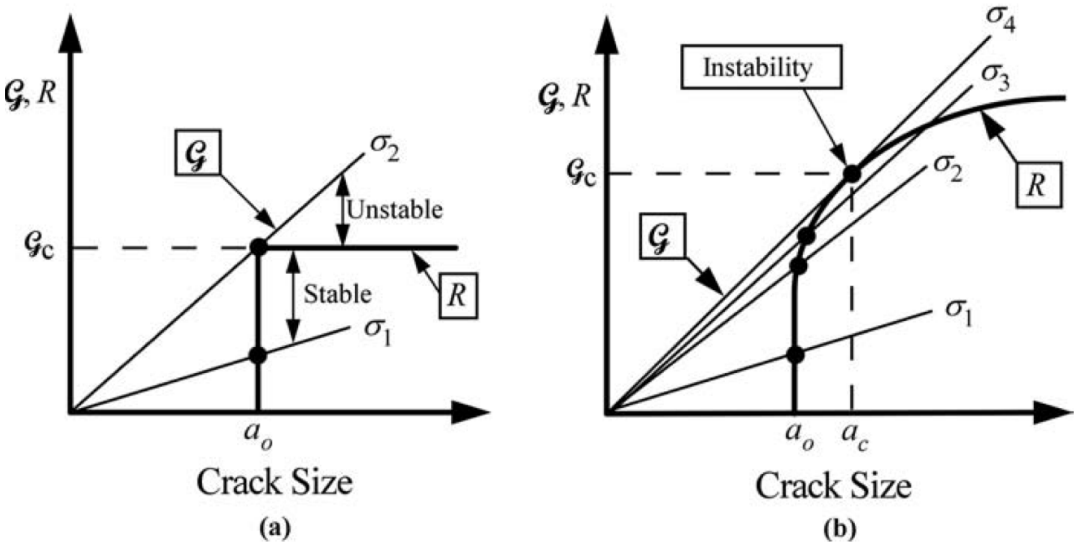

FIGURE 2.6: Schematic of R-curves to illustrate linear-elastic and non-linear critical energy release rates (a) flat R-curve and (b) rising R-curve (Anderson, 2005).

Figure 2.6(b) shows a rising R-curve, where the material exhibits non-linear behaviour. The crack is stable for σ_1, the crack grows by a small amount when the stress is σ_2, yet does not grow if the stress stays constant. When the applied stress increases to σ_3, stable crack growth continues. The stress between σ_2 and σ_3 can be regarded as the threshold value before crack extension. When the stress reaches σ_4 the material is unstable and crack growth continues. Materials, such as metals exhibit ductile fracture, that have a rising R-curve and cannot have a single toughness value that characterises the toughness

and entire crack behaviour of the material. The material resistance is characterised by the surface energy and the plastic dissipation at the crack tip. At the crack tip the plastic zone forms, which increases as the crack grows, resulting in an increase in force to maintain stable crack growth. The R-curve and the fracture toughness are regarded as material properties, which are independent of the geometry of the cracked structure.

2.3.3 Stress intensity approach

The second approach is the stress intensity approach, where the stresses at a crack tip can be characterised by a single fracture toughness parameter or critical stress intensity factor, K_c. It was shown that the stresses around a crack tip could be described by Equation 2.20 with polar coordinates with the origin at the crack tip, as seen in Figure 2.7.

$$\sigma_{ij} = \frac{K}{\sqrt{r}} f_{ij}(\theta) + \sum_{m=0}^{\infty} A_m r^{\frac{m}{2}} g_{ij}^{(m)}(\theta) \tag{2.20}$$

where σ_{ij} is a stress tensor, K is the constant stress intensity factor, r is the distance from the crack tip to the material point under consideration, θ is the angle of r, shown in Figure 2.7, and $f_{ij}(\theta)$ is a dimensionless function of θ. The right side of Equation 2.20 is for higher order terms, which depends on the geometry. Furthermore, Equation 2.20 is asymptotic to $r = 0$ and describes the stress singularity at the crack tip.

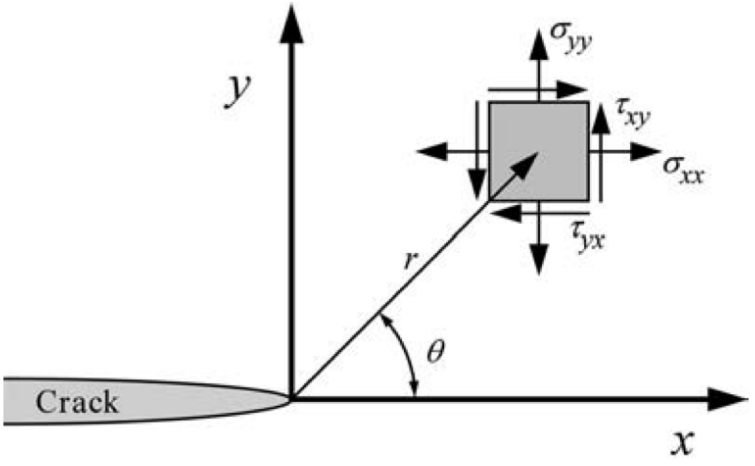

FIGURE 2.7: The polar coordinates defined in front of a crack tip with stresses defined by Equation 2.20 (Anderson, 2005).

There are three different Modes of fracture, illustrated in Figure 2.8: Mode I, where the load is applied normal to the crack plane and the crack grows in the opening direction; Mode II, which is in-plane shear loading and causes one crack face to slide in-plane with respect to the other; and Mode III is out-of-plane shear loading. The stress intensity factor can be used to describe the stresses at a crack tip for different modes and is denoted with the Mode subscript, i.e. K_I, K_{II} or K_{III}. A combination of the loadings can be applied to a cracked body.

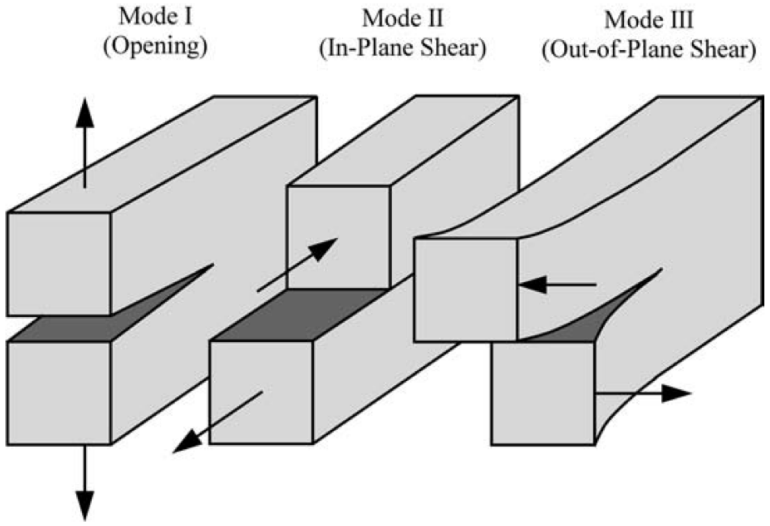

FIGURE 2.8: The three different Modes of loading on a cracked body (Anderson, 2005).

2.3.4 Crack tip plasticity

From the stress intensity approach and Equation 2.20 it was shown that the stress at a sharp crack tip is infinite, however, in a real material the stresses are finite. Particularly in metals, plastic deformation occurs at the crack tip, which lowers the crack tip stresses. Elastic stress analysis becomes increasingly inaccurate as the inelastic region at the crack tip increases. This is where linear-elastic fracture mechanics (LEFM) no longer holds and alternative crack tip parameters are required.

In Figure 2.9 the plastic zones for Mode I and Mode II are illustrated, which were estimated with elastic solutions, where r_y is the radius from the crack tip and σ_{YS} is the von Mises criterion. Both figures indicated the plane-stress and plane-strain zones, respectively.

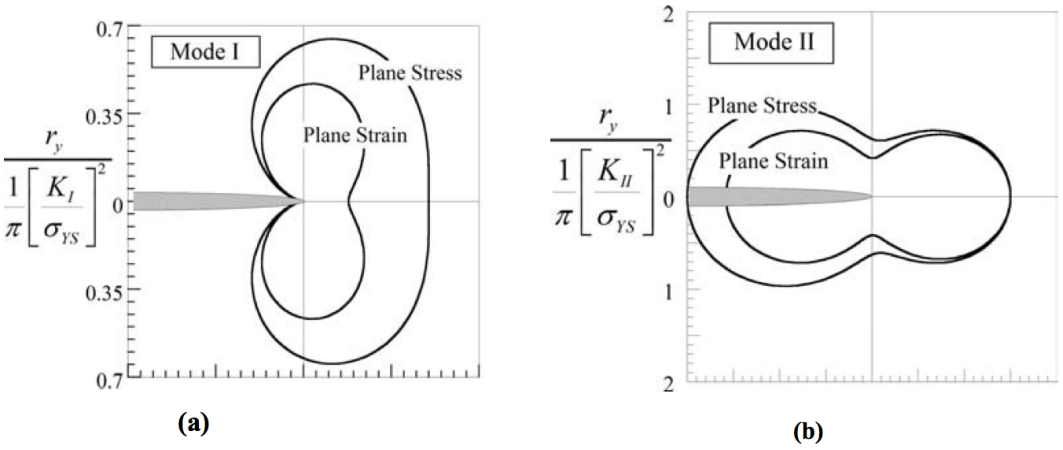

FIGURE 2.9: Plastic zones at the crack tip (a) Mode I and (b) Mode II (Anderson, 2005).

Generally the conditions at a crack tip are neither plane strain nor plane stress. It is a combination of both in three dimensions. Considering a cracked plate loaded in-plane, as seen in Figure 2.8 for Mode I, the material at the surface is in plane stress conditions. The stress normal to the surface is zero, due to no material constraining it in the normal direction. While the interior of material is in plane strain conditions. The surrounding interior material is constraining movement in the normal conditions, hence normal strain is equal to zero. Regardless of the combination of conditions, most classical fracture mechanics solutions simplify the problem to two dimensions.

The energy release rate is uniquely related to stress intensity and G_c, however the two parameters do not consider plastic nor non-linear behaviour at the crack tip. Equation 2.20 does not account for the stress distribution within the plastic zone. Anderson (2005) raised an important question: "is stress intensity a useful failure criterion in material that exhibit inelastic deformation at the crack tip?". Under certain conditions, provided that the plastic zone is small, K still uniquely describes the crack tip conditions.

In thinner specimens, as the plastic zone increases and reaches a considerable fraction of the through-thickness, the overall conditions are then regarded as plane stress. This results in a higher material fracture toughness. Figure 2.10 illustrates this effect. The opposite effect is also illustrated, where the overall conditions tend to plane strain as the thickness increases. K_{Ic} is regarded as the plane strain fracture toughness. Therefore,

testing for K_{Ic}, the material at the crack tip has to be both predominantly in plane strain and remain linear-elastic during fracture.

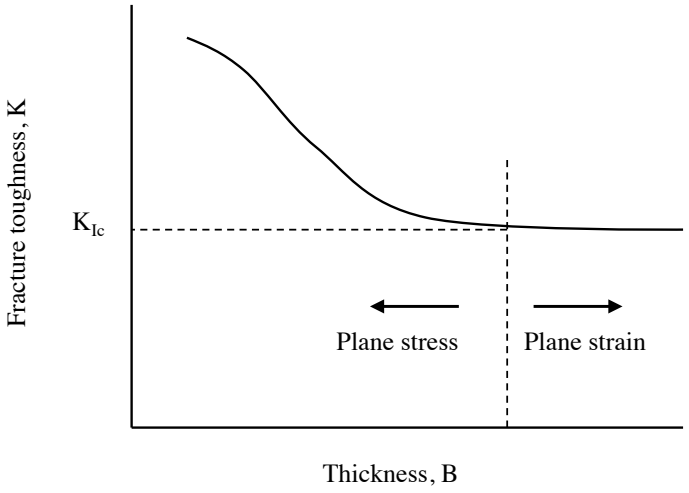

FIGURE 2.10: Effect of specimen thickness on the fracture toughness.

The constraint of through-thickness can also have an influence on the shape of the R-curve, which manifest most in ductile materials. For the same material the R-curve is much steeper in plane stress conditions, while for plane strain it is relatively flat. The difference between a flat and steep R-curve was illustrated in Figure 2.6.

When a material starts exhibiting significant non-linear behaviour, the stress intensity approach should be discarded. Crack tip parameters that take plastic behaviour into account should be considered.

2.3.5 Elastic-plastic fracture mechanics

An alternative fracture parameter was developed by Rice (1968) to characterise the non-linear behaviour ahead of a crack tip. The linear-elastic energy release rate was generalised to account for non-linear materials where the non-linear energy release rate is commonly expressed as a line integral, called the J-integral. The J-integral also relates to stress fields at crack tips of non-linear materials and can also be viewed as a non-linear stress intensity (Hutchinson, 1968, Rice and Rosengren, 1968). The J-integral was successfully used to characterise the fracture toughness of steels (Begley and Landes, 1972). Since its development, numerous design codes have standardised experimental

methods to determined the fracture toughness of materials. Standards such as the British Standard Institution (BSI), International Organization for Standardization (ISO) and American Society for Testing and Materials (ASTM), where the latter was considered and will further be discussed.

Another parameter that is often used is the Crack Tip Opening Displacement (CTOD), where the opening of the crack faces increase due to blunting of an initial sharp crack caused by plastic deformation. The increase in crack blunting was observed to be proportional to the toughness of the material and the CTOD was proposed as a measure of fracture toughness (Wells, 1961). In this project the focus is on utilising the J-integral, therefore the CTOD is not further discussed.

The same definition from Equation 2.17 holds for the non-linear energy release rate, where J replaces G:

$$J = -\frac{d\Pi}{dA} \tag{2.21}$$

In an elastic material, the energy release rate is defined as the potential energy released from crack growth, however, in an elastic-plastic material the strain energy absorbed is not recovered when a crack grows or the material is unload. Also, a growing crack leaves a plastic wake.

The conventional J-integral is given as:

$$J = \int_{\Gamma} (w dy - T_i \frac{\partial u_i}{\partial x} ds) \tag{2.22}$$

where w is strain energy density, u_i is a displacement vector, ds is a length increment along the contour Γ and T_i is a traction vector defined by:

$$T_i = \sigma_{ij} n_j \tag{2.23}$$

where n_j is the vector normal to Γ. Traction is here defined as the stress vector normal to a contour path. The strain energy density is given as:

$$w = \int_0^{\epsilon_{ij}} \sigma_{ij} d\epsilon_{ij} \tag{2.24}$$

where ϵ_{ij} is the strain tensor. Figure 2.11 illustrates the contour around a crack tip from which the J-integral is determined. Also note that the J-integral is independent of the contour and is therefore called a path-independent integral (Rice, 1968).

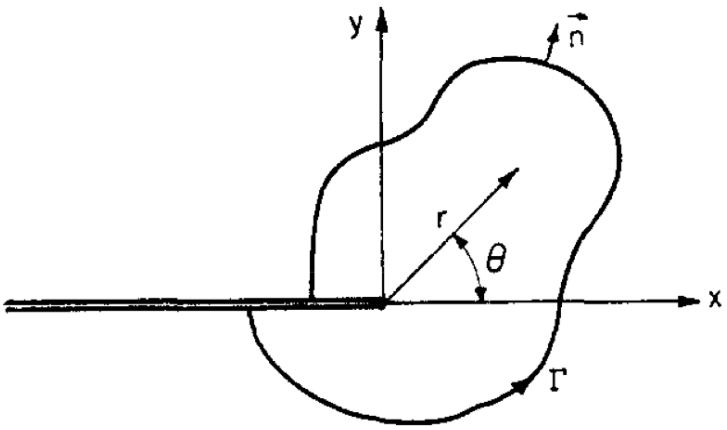

FIGURE 2.11: Arbitrary contour around a crack tip (Rice and Rosengren, 1968).

2.3.6 The relationship between K, G and the J-integral

Up to this point three parameters have been introduced, namely K_c, G_c and the J-integral or J_c, which are all regarded as the fracture toughness. K_{Ic} is the fracture toughness with regards to the critical stress intensity factor and is most commonly used in industry to characterise materials. G_{Ic} is an alternative fracture toughness with regards to the critical energy release rate of a brittle linear-elastic material. Lastly, J_c is an alternative fracture toughness with regards to the non-linear critical energy release rate of ductile materials exhibiting elastic-plastic behaviour. The energy release rate describes the global behaviour and the stress intensity describes the local behaviour.

For a brittle linear elastic material the three parameters can be related as:

$$G = J = \frac{K^2}{E'} \tag{2.25}$$

where for plane stress

$$E' = E \tag{2.26}$$

and for plane strain

$$E' = \frac{E}{1-\nu^2} \tag{2.27}$$

It should be clarified that for a special case, where the energy release is predominately through cracking and minor plastic deformation, $J = G$. When more plastic deformation is present, the assumption can be made that $J \simeq G$. However, when significant plastic deformation occurs $J \neq G$, K is also discarded and elastic-plastic fracture mechanics (EPFM) principles should be followed. This is also when the valid specimen thickness criterion comes into effect, which will be discussed in the next section. Furthermore, when extensive plastic deformation occurs, EPFM no longer holds.

2.3.7 Fracture toughness testing

Fracture toughness testing involves measuring the resistance of a material to crack extension, where a test can yield a single fracture toughness value, such as K or J, or a resistance curve, as illustrated in Figure 2.6. Materials that fail by cleavage, with brittle behaviour, usually only need one parameter, indicated by a constant G_c as seen in the flat R-curve in Figure 2.6(a). Ductile materials have a more stable initial cracking behaviour, where the crack grows by microvoid coalescence and typically yields a rising R-curve as seen in Figure 2.6(b), (Anderson, 2005). When testing ductile materials, the specimen seldom fails immediately, therefore a single parameter or the R-curve can be used to characterise failure. As mentioned, the ASTM has standardised procedures for testing fracture toughness and is the standard the most widely used. The ASTM procedures are consistent with other mentioned standards. The procedures include experimentally determining K_{Ic}, K-R-curves, J_{Ic} and J-R-curves. It should be noted that the procedures are for determining Mode I parameters and currently there are no standarised procedures for determining Mode II, III or mixed Mode parameters. Therefore, alternative methods for testing Mode II and mixed Mode are researched.

The ASTM-E399 covers the test methods to determine K_{Ic} of metallic materials under predominately linear-elastic, plane strain conditions with fatigue pre-cracked test specimens (ASTM-E399, 2009). There are several different types of specimens for characterising crack growth, and determining K_{Ic}. Standard tests include Compact Tension

(CT), Single Edge Notched Tension (SENT), Double Edge Notched Tension (DENT) and Single Edge Notched Bend (SENB). Figure 2.12 shows a typical CT specimen with dimensions and force, P applied in Mode I.

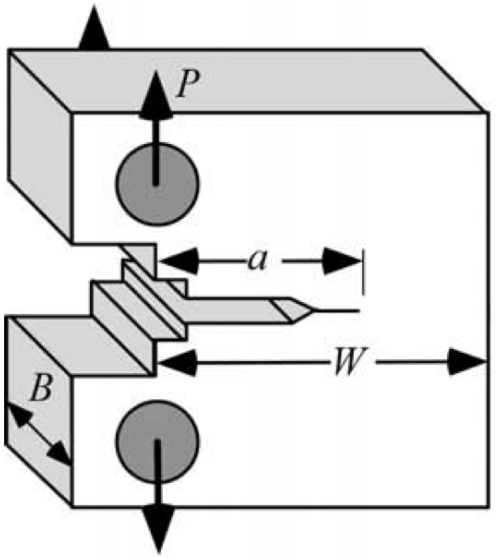

FIGURE 2.12: Typical CT specimen dimensions (Anderson, 2005).

The ASTM-E23 covers tests for impact testing of metallic materials and covers a popular test called the Charpy Impact test, which is used to measure the material toughness (Charpy, 1912). Material toughness is measured in Joules and should not be confused with the fracture toughness, K_{Ic} measured in MPa$\sqrt{\text{m}}$. The Charpy Impact test is used for qualitative toughness measurements. It relates the behaviour of metals subjected to a single application of force which results in multi-axial stresses in cases of low and high temperatures (ASTM-E23, 2007). Standards are available to correlate between the Charpy Impact energy and fracture toughness, however, the relations are empirically derived and only estimated fracture toughness values can be obtained (Bannister, 1998).

To apply fracture mechanics, an infinitely sharp crack is needed before loading, as seen in Figure 2.12. In absence of a sharp crack the fracture toughness measured is typically higher and is rather a measure of the notch toughness. The sharp crack is usually made by fatigue pre-cracking a metallic specimen or razor cutting a sharp crack in non-metallic specimens, which are too brittle to fatigue crack. Fatigue cracks are produced by cyclically loading a specimen typically at a frequency of $10Hz$ between tensile stresses lower than the yield stress. Paris was the first to demonstrate that fracture mechanics can be applied to characterise fatigue crack growth (Paris and Erdogan, 1960, Paris et al., 1961).

In order to pre-crack specimens a basic understanding is needed of the loading procedure, however, characterising fatigue cracking is not the focus of this project. ASTM E647, E1823 and ASTM E399 covers procedures for fatigue cracking metallic materials (ASTM-E1823, 2011, ASTM-E647, 2011). Figure 2.13 shows the typical fatigue crack growth behaviour for metals, where the logarithm of crack increment, da over difference in load cycles, N is plotted against the logarithm of the difference in fracture toughness, ΔK. Zone I indicates where a crack will be initiated at the threshold fracture toughness, ΔK_{th}, Zone II is in the Paris region where stable fatigue crack growth occurs and Zone III is where unstable cracking and fracture occurs. In order to grow a fatigue crack according to standard the cyclic loading has to be within Zone II.

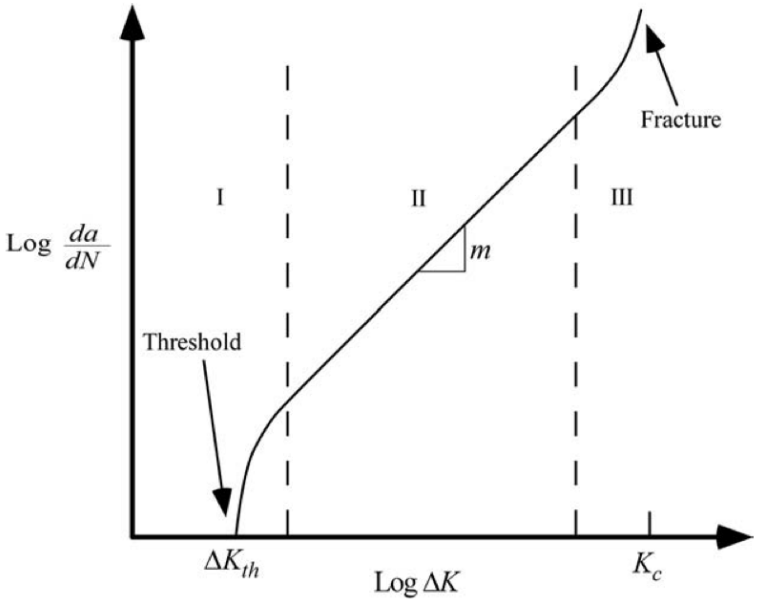

FIGURE 2.13: Typical fatigue crack growth curve of metals (Anderson, 2005).

The load, displacements and crack increments need to be measured during a K_{Ic} test, where the first is usually measured with a load cell, which is connected to the tensile machine. The displacements are conventionally measured with clip gauges or linear variable differential transducers (LVDT). The conventional displacement measuring techniques consequently only measure one-dimensional displacement and have to be attached to the specimen. For each specimen type a different configuration has to be applied and if more than one-dimensional displacement are required, more instrumentation is required on the specimen. This motivates the use of alternative methods to measure displacements, such as non-contact methods like DIC.

The ASTM E399 has requirements for K_{Ic} measurements to be valid, such as the crack length and specimen thickness, given as:

$$0.45 \leq a/W \leq 0.55 \tag{2.28}$$

and

$$B, a \geq 2.5\frac{K_Q}{\sigma_{YS}} \tag{2.29}$$

where $K_Q = K_{Ic}$ when all the requirements are met. The linear-elastic fracture toughness, K_{Ic} can then be computed as:

$$K_{Ic} = \frac{P_{max}}{B\sqrt{W}} f(a/W) \tag{2.30}$$

where P_{max} is the maximum load of a linear-elastic material, B is the specimen thickness, W is the length of the specimen from the applied load (Figure 2.12), a is the crack length from the crack tip location to where P is applied. Therefore the knowledge of the exact crack tip location is very important to accurately determine K. $f(a/W)$ is a dimensionless geometry function of a/W, and polynomial analytical solutions exist for all the standard specimens. Typically initial estimate for K_Q is used in Equation 2.29.

The thickness requirements of ASTM-E399 often requires specimens to be impractically large, especially for structural materials like high strength metals (Anderson, 2005). In the case where LEFM requirements are no longer valid and the specimen exhibits too much plastic behaviour to compute K_{Ic}, the J-integral can be used to characterise the material fracture toughness. ASTM-E1820 covers the procedures to determine the J_{Ic} and the specimen size requirements are much more lenient compared to that of ASTM-E399 (ASTM-E1820, 2011):

$$0.50 \leq a/W \leq 0.70 \tag{2.31}$$

and

$$B, b_o \geq \frac{25J_Q}{\sigma_Y} \tag{2.32}$$

where $b_o = W - a$ and is the remaining material ahead of the crack, $J_Q = J_{Ic}$ when requirements are met, and σ_Y is yield stress.

In order to determine J_{Ic}, the J resistance curve has to be determined. The basic multiple-specimen technique can be used, where different loads are applied to specimens. The specimens are then unloaded and the crack extension is measured. The material at the crack tip effectively softens, which is called the compliance, C. It is determined with the inverse of the gradient of the unloading path, as illustrated in Figure 2.14 and Figure 2.15. The compliance is a result of plastic deformation and cracking. From the plastic area, A_{pl}, the fracture energy can be determined for each unloading.

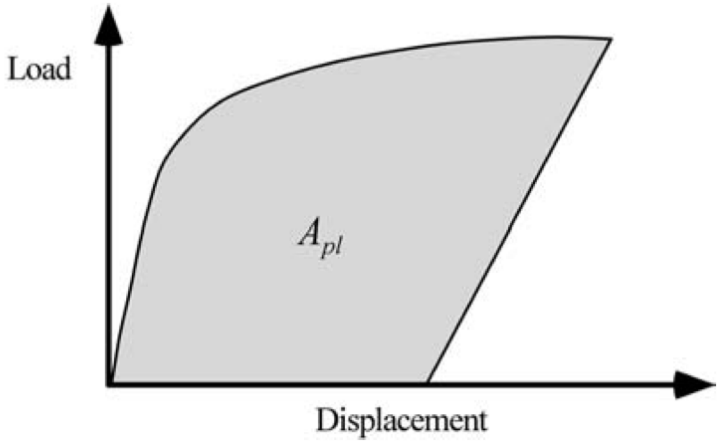

FIGURE 2.14: The basic multiple-specimen technique, where A_{pl} is the plastic energy absorbed after unloading (Anderson, 2005).

The disadvantage of the multi-specimen technique is that several specimens have to be tested to obtain a J-R-curve. A more convenient technique is the unloading compliance method, which is a single-specimen technique. A single specimen is loaded and partially unloaded, and the compliance of each unloading is used to determine the energy absorbed by plasticity and cracking. Figure 2.15 illustrates the load-unloading method and where to obtain the compliance.

The J-integral can be divided into two components, i.e. plastic and elastic:

$$J = J_{el} + J_{pl} \tag{2.33}$$

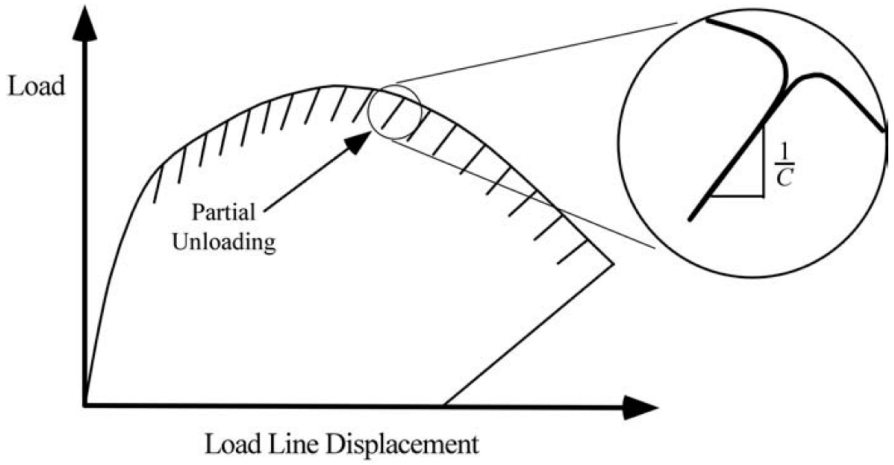

FIGURE 2.15: Unloading compliance method (Anderson, 2005).

The elastic component is given as:

$$J_{el} = \frac{K^2(1-\nu^2)}{E} \tag{2.34}$$

where K is determined with Equation 2.30. The plastic component is computed from the plastic area under the load-displacement curve:

$$J_{pl} = \frac{\eta A_{pl}}{B b_o} \tag{2.35}$$

where η is a dimensionless constant (note that η was also used in peridynamic nomenclature), A_{pl} is the plastic area as shown in Figure 2.14. For a CT specimen:

$$\eta = 2 + 0.522 b_o / W \tag{2.36}$$

When using the unloading compliance method, $J_{pl(i)}$ is computed for each unloading cycle (depicted by the i subscript) using the respective plastic area:

$$J_{pl(i)} = \left[J_{pl(i-1)} + \left(\frac{\eta_{pl(i-1)}}{b_{(i-1)}} \right) \frac{A_{pl(i)} - A_{pl(i-1)}}{B} \right] \left[1 - \gamma_{(i-1)} \left(\frac{a_{(i)} - a_{(i-1)}}{b_{(i-1)}} \right) \right] \tag{2.37}$$

where $A_{pl(i)} - A_{pl(i-1)}$ is the increment of plastic area and,

$$\gamma_{(i-1)} = 1.0 + 0.76 b_{(i-1)}/W \tag{2.38}$$

where $b_{(i-1)}$ is the remaining material at unloading i.

A typical J-R-curve is illustrated in Figure 2.16 with construction lines in accordance to ASTM-E1820. The J-integral values, computed from Equation 2.37, are plotted against crack extension. A power law regression line is fitted to the J values and the J_Q value is read of the 0.15 mm construction line. If all the requirements are met then $J_Q = J_{Ic}$ (ASTM-E1820, 2011). The plot shows a rising R-curve, which indicates that more energy is needed to further extend the crack as the material plastically deforms.

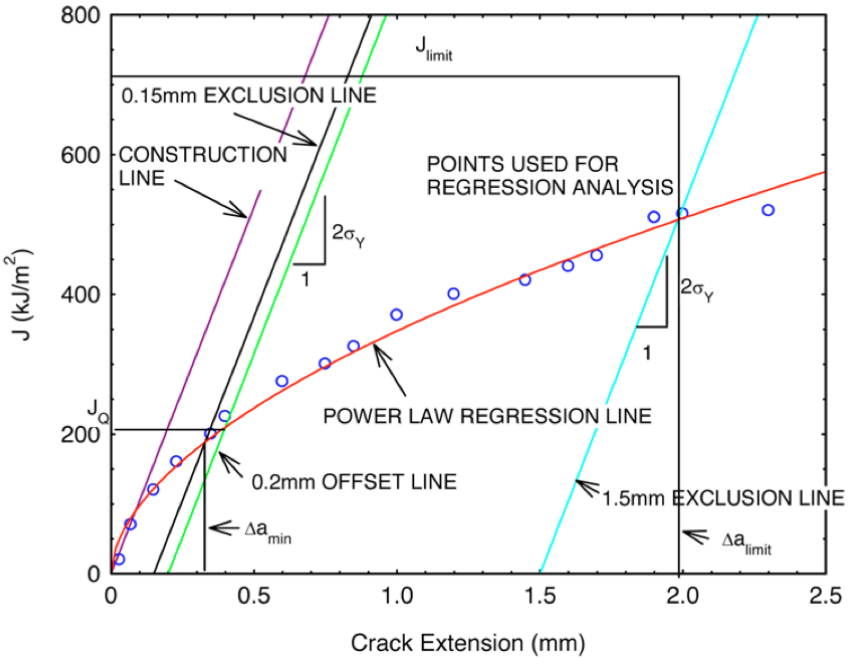

FIGURE 2.16: Typical J-R-curve with construction lines (ASTM-E1820, 2011).

2.3.8 Mixed Mode testing

Structural failure due to cracking rarely or never occurs in pure Mode I, II or III. Structures are always loaded in mixed Mode to a certain degree. Also, note that $K_{Ic} \neq K_{IIc} \neq K_{IIIc}$. This gave motivation to devise experimental methods to test the mixed Mode fracture properties of materials. Existing methods include the mixed Mode Bending (MMB) test (Reeder and Crews, 1990), edge-delamination tension test (O'Brien, 1984),

the mixed Mode flexure (Russel and Street, 1985) and crack-lap shear test (Johnson, 1987). Alternative tests include using Diagonally Loaded Square Plate (DLSP) specimens loaded in tension, where different inclined center notches test different mixed Mode configurations for brittle materials, such as polymethyl methacrylate (PMMA) (Ayatollahi and Aliha, 2009). The same brittle materials were tested for mixed Mode with edge cracked semi-circular specimens to asymmetric three point loading (Ayatollahi et al., 2011). Although the tests are capable of measuring mixed Mode fracture toughness values, they all have restrictions. Several different specimens are required to test different mixed Modes for the same method. Different test configurations are required, which can influence the reliability of results. It was found that the mixed Mode method called the Modified Arcan test resolves many of the issues found with other techniques (Hosseini et al., 2008).

2.3.9 Modified Arcan test

Arcan originally developed a test fixture to perform mixed Mode loading of composite specimens with a solid disk with notches in the middle to induce fracture and holes in the circumference to alternate the loading inclination (Arcan et al., 1978, Banks-Sills et al., 1984). The test was modified by separating the two half disks and connecting a disposable butterfly-shaped specimen in the middle for stable tearing (Amstutz et al., 1995, 1997). Figure 2.17 illustrates the Modified Arcan test and butterfly-shaped specimen with a precut notch of length a.

The Modified Arcan test can be used to measure the fracture toughness in pure Mode I, pure Mode II and mixed Mode, thus K_{IC}, K_{IIC} and K_{IC}/K_{IIC}. The advantage of the test is that the same configuration can be used for different modes, the fixture only needs to be rotated in the desired mode of loading. Also, the same specimen can be used for different loadings.

The Modified Arcan test has been successfully used to determine mixed Mode behaviour of inter-laminar fracture of carbon-epoxy thermoplastic laminated composites (Nikbakht and Choupani, 2008). Furthermore, the mixed Mode fracture behaviour of high strength steel butt welds and friction stir welds were tested (Hosseini et al., 2008, Sutton et al., 2003). In the latter test DIC software was utilised to measure COD values of cracks forming in the welds. The crack behaviour of aluminium alloy was tested, where it was

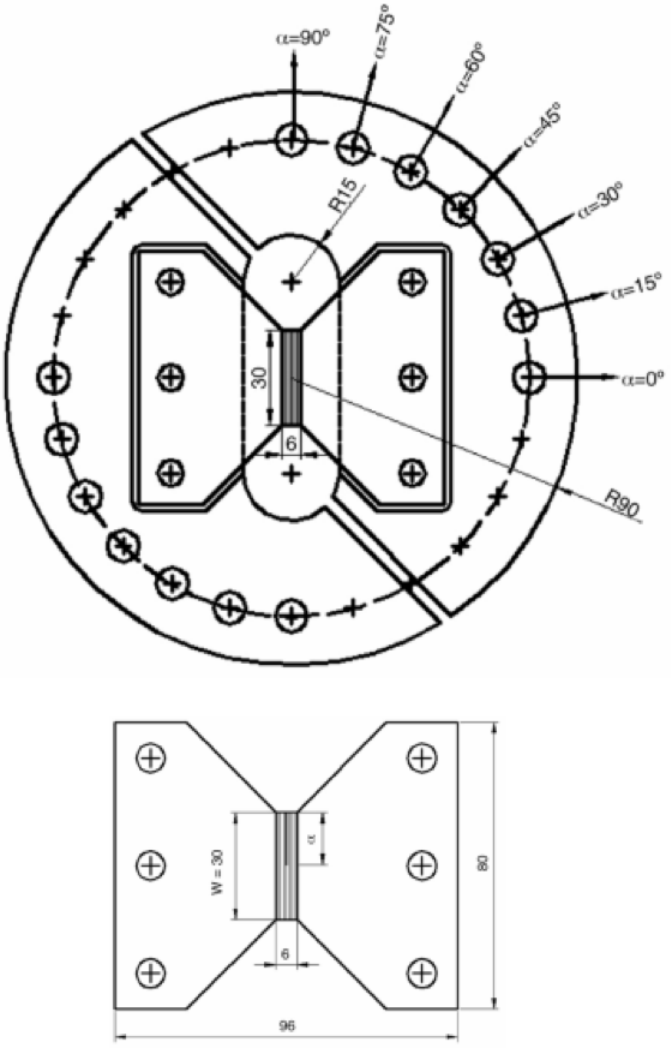

FIGURE 2.17: Typical Modified Arcan Test and Arcan specimen (Nikbakht and Choupani, 2008).

found that below 53.2 degrees the point of crack initiation could not be determined due to plasticity that formed a shear band throughout the whole ligament of the specimen (Hallback and Nilsson, 1994).

2.4 Digital image correlation

The DIC method is an optical technique that measures full surface displacement fields of loaded objects (Sutton et al., 1983). Conventional measuring instrumentation needs to be connected to the specimen and special configurations are required, which often

restricts the desired measurements. Fracture testing measurements are particularly difficult with strain gauges. The measurements are often not valid when the crack path propagates through the strain gauge position, as experienced by Foster (2009). Using LVDT's only allow one-dimensional measurements between two points and does not allow for obtaining data near the crack tip. DIC is a non-contact method, where the instrumentation does not interfere with the specimen. Also, DIC has the advantage of measuring displacements near the crack tip, where the crack behaviour is of interest to characterise failure (Roux and Hild, 2007).

2.4.1 Background on digital image correlation

In the past experimental solid mechanics focused more on laser technology for measurements with coherent light sources. Numerous measurement techniques were used, such as holography (Gabor, 1949), laser speckle (Dainty, 1975), laser speckle photography (Archbold et al., 1970), laser speckle interferometry (Mallik and Roblin, 1972) and holographic interferometry (Vest, 1979).

Peters and Ranson (1982) proposed the use of computer-based image acquisition and deformation measurements in material systems. Sutton et al. (1983) showed the feasibility of DIC by developing numerical algorithms and performing experiments using optically recorded images. The DIC method uses a comparison of small regions, called subsets, throughout the images before and after deformation. The positions of each of the subsets after deformation are located with digital image analysis. Classical continuum mechanics is subsequently used to determine the deformation of the subsets between the initial, reference and deformed images, which results in a deformation mapping function that relates the images.

DIC has been applied to quantify deformations and rotations in solids (Sutton et al., 1985). Further development improved the subset-matching to achieve sub-pixel accuracy throughout the image to determine a dense full field two-dimensional displacement measurements with gradient search methods (Sutton et al., 1986). The Newton-Raphson method was used to improve the coarse-fine search method for obtaining deformations, which allowed determining displacement gradients and using less Central Processing Unit (CPU) time (Bruck et al., 1989, Sutton et al., 2009).

2.4.2 Overview of the digital image correlation method and specimen preparation

DIC requires only one or two Charged Coupled Device (CCD) cameras to record images of a surface of a material before and after deformation. Camera technology is developed and improved at a rapid pace, particularly in high-spatial-resolution digital image acquisition devices. Fortunately, the DIC algorithm is robust and can process any resolution digital images (Pan et al., 2009). Also, it can be used with optical microscopy (Sun et al., 1997), laser scanning confocal (Berfield et al., 2006), scanning electron microscopy (Sabate, 2006) and atomic force microscopy (Chasiotis and Knauss, 2002) to measure microscale and nanoscale deformation. Moreover, it can be used with high-speed recordings for instantaneous deformation measurements (Kawahashi and Hirahara, 2002).

The quality of the images is of great importance and using poor quality imaging systems typically result in erroneous measurements. DIC testing requires a white light source or natural light for illumination. This allows DIC to be used in the lab or for field applications. The surface of the test specimen has to have a random grey intensity pattern or the algorithms will fail to find an unique subset in the deformed images. In the case where the material surface has a natural texture of random grey intensity distribution, the specimen requires no preparation. However, most materials have a consistent surface texture and require an artificial random grey intensity distribution, called a speckle pattern, as seen in Figure 2.18. This can simply be made by spraying paint on the surface. The speckle pattern deforms with the specimen surface and serves as the carrier of the deformation information.

After the digital images of the undeformed and deformed material are recorded, the DIC method computes the motion of each point by comparing the images. The reference image is defined, divided into subsets and the displacements of each center point of a subset determined from the deformed subsets. This results in a full deformation field. The basic principle of DIC is illustrated in Figure 2.19, where a point P on a square reference subset is chosen and used to track a corresponding location in the deformed image. A subset of pixels, rather than a single pixel, is matched as a subset, since it has a more distinct pattern of grey intensities that can be uniquely identified from other subsets in a deformed image.

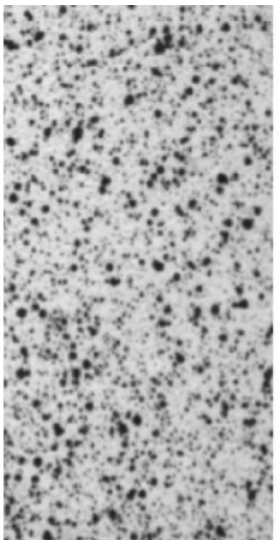

FIGURE 2.18: Typical speckle pattern on the surface of a DIC specimen (Lecompte et al., 2006).

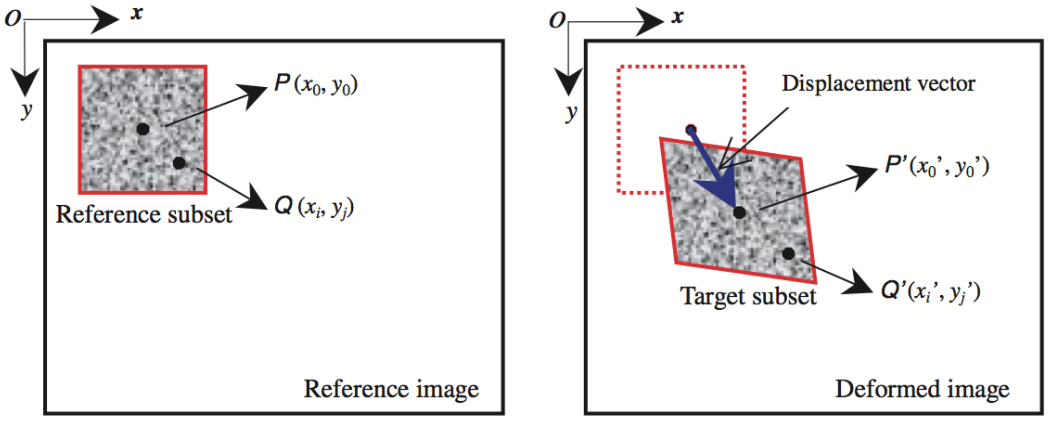

FIGURE 2.19: Reference and deformed subset (Pan et al., 2009).

In order to determine the degree of similarity between the reference and deformed subset a cross-correlation criterion is predefined. The peak position of the correlation coefficient distribution defines if the matching procedure is complete, as illustrated in Figure 2.20. Once the maximum correlation coefficient is detected the position of the deformed subset is determined. The difference between the reference subset center and target deformed subset center positions results in the in-plane displacement vector at P, as shown in Figure 2.19.

The subset deformation is assumed to be continuous, hence neighbouring points in the reference subset remain in the deformed target subset. The coordinates of point $Q(x_i, y_j)$

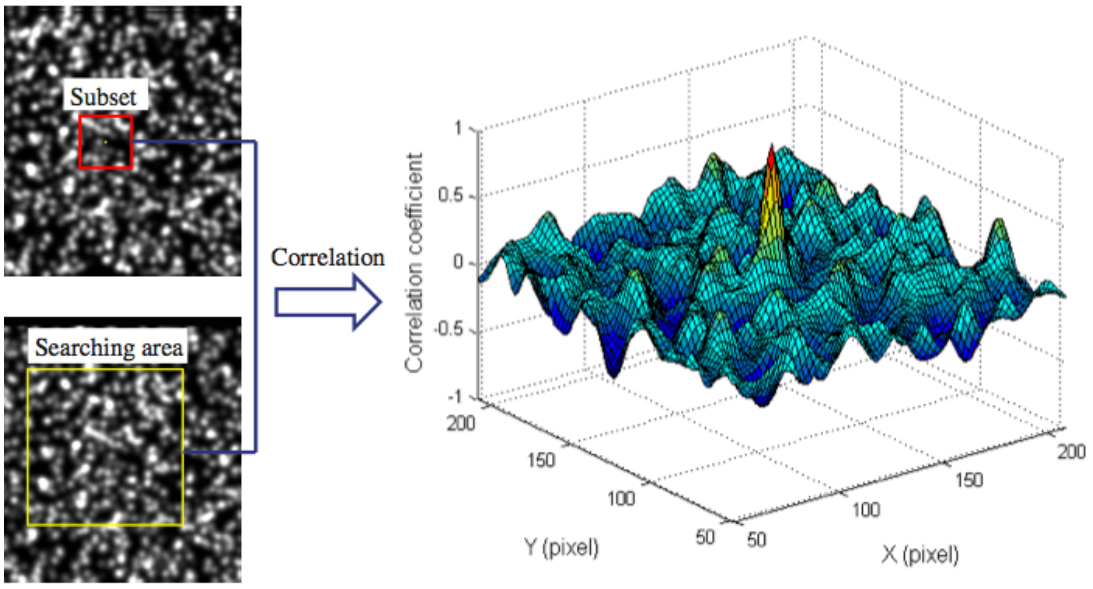

FIGURE 2.20: Whole field cross-correlation distribution of a deformed image subjected to rigid body motion (Pan et al., 2009).

can be mapped to point $Q'(x'_i, y'_j)$ from the reference to target deformed subset with displacement mapping functions (Lu and Cary, 2000) or shape functions (Schreier and Sutton, 2002). The displacement of a point is typically determined using the first-order shape function, which allows for rigid body translation, rotation, shear, normal strains and combinations:

$$x' = x + u + \frac{\partial u}{\partial x}\Delta x + \frac{\partial u}{\partial y}\Delta y \tag{2.39}$$

$$y' = y + v + \frac{\partial v}{\partial x}\Delta x + \frac{\partial v}{\partial y}\Delta y \tag{2.40}$$

The local deformation values and gradients for a subset are the values of u, v, $\frac{\partial u}{\partial x}$, $\frac{\partial u}{\partial y}$, $\frac{\partial v}{\partial x}$ and $\frac{\partial v}{\partial y}$. Second-order shape functions can be implemented to map more complicated deformations (Lu and Cary, 2000).

The Zero Normalised Sum-Squared Difference (ZNSSD) correlation is most commonly used to evaluate the degree of similarity between the reference and deformed subsets. It was found that the ZNSSD correlation is most robust to noise and is insensitive to offset and linear scale in illumination (Pan et al., 2009). The ZNSSD formulation is given as:

$$C_{ij} = 1 - \frac{\Sigma_i \Sigma_j \left[F\left(x_i, y_j\right) - \overline{F}\right]\left[G\left(x'_i, y'_j\right) - \overline{G}\right]}{\sqrt{\Sigma_i \Sigma_j \left[F\left(x_i, y_j\right) - \overline{F}\right]^2 \Sigma_i \Sigma_j \left[G\left(x'_i, y'_j\right) - \overline{G}\right]^2}} \tag{2.41}$$

where $F(x_i, y_j)$ is the grey scale value of the pixel intensity at the point (x_i, y_j) in the undeformed image. $G\left(x'_i, y'_j\right)$ is the gray scale value of the deformed image at point $\left(x'_i, y'_j\right)$. $\overline{F}$ and $\overline{G}$ are the mean values of F and G, respectively.

Typically the coordinates of a point in the deformed subset are between pixels, which results in the acquirement of the intensity value at sub-pixel level. A sub-pixel interpolation scheme is used to determine the intensities. Numerous interpolation schemes are used, such as bilinear interpolation, bicubic interpolation and bicubic B-spline interpolation. The higher-order bicubic spline interpolation schemes are preferred, due to the high registration accuracy and better convergence capabilities (Schreier et al., 1999).

In order to achieve sub-pixel accuracy an initial deformation estimate is determined and then sub-pixel displacement is measured. The initial deformation estimate requires an initial accurate guess, where iterative spatial cross-correlation algorithms, like the Newton-Raphson method, only converges when an initial guess is provided (Pan et al., 2005). Normally in commercial software an initial guess is manually selected in the reference image and the corresponding coordinates can be resolved using least-squares method (Pan et al., 2009).

2.4.3 Speckle pattern and subset size

In order to create a speckle pattern on the surface of specimen, a fine layer of white paint is sprayed on the material surface, following an application of evenly distributed black paint speckles. It was found that a larger subset size gives a more accurate displacement measurement. For homogeneous deformation the pixel displacement information in a larger subset can be smoothed, which results in more accurate surface displacements. When smaller subsets are used, for example when observing displacement fields near cracks, more precise displacement data can be measured. However, smaller speckles have to be applied to the material surface. When small subsets are used with a large speckle pattern the results are very inaccurate and vice versa for larger subsets. Thus for homogeneous deformation, larger subsets with larger speckles yields the most accurate displacement field measurements (Lecompte et al., 2006).

The best relation between subset size (pixels x pixels) and mean speckle size (diameter in pixels) is given as follows (Lecompte et al., 2006):

- Small, subset size 13x13 use speckle size of 3
- Medium, subset size 23x23 use speckle size of 10
- Large, subset size 33x33 use speckle size of <10

2.4.4 Digital image correlation and failure analysis

DIC has been extended to determine failure characteristics in applications of fracture mechanics in numerous studies. McNeil et al. (1987) extended DIC to determine stress intensity factors using least square estimation. DIC was also used to measure COD (Dawicke and Sutton, 1994). Further, DIC methods using high magnification optical systems were developed to measure deformations ahead of stable and propagating cracks in Mode I (Han et al., 1994, 1995). Mixed Mode Arcan tests were performed, where the tensile and shear deformation was measured using DIC (Amstutz et al., 1995, 1997, Wang et al., 2012). Alternative methods were developed using virtual crack extension and auxiliary fields to determine stress intensity factors from CT and mixed Mode tests (Gravouil et al., 2004) and using displacement field identification on three point-bend tests provided Mode I and Mode II stress intensity factors (Hild and Roux, 2006, Roux and Hild, 2006). A method incorporating DIC displacement fields in XFEM was developed to describe the displacement jump and crack face geometry, called eXtended Digital Image Correlation (XDIC). However, stress intensity factors were not a direct output of the method and the obtained values were sensitive to the discontinuity displacement enrichments (Rethore et al., 2007). Further studies resulted in accurately determining stress intensity factors and crack tip positions of 2D and 3D cracks, where the sub-pixel accuracy is able to capture cracks that are invisibly to the eye (Roux et al., 2009). Another methodology was developed where the J-integral was determined using full field measurements and FEM, where data away from the crack is used in the area integral (Becker et al., 2012). Crack behaviour and damage characteristics of Nuclear Block Graphite (NBG10) was determined using the method (Becker et al., 2011). Other methods were also developed implementing DIC to identify damage models using FEM, which estimates the degradation of material properties (Claire et al., 2004, Roux and Hild, 2007).

DIC assumes continues deformation and when discontinuities like cracks appear in the deformed image, non-physical displacements are determined or the correlation criteria is

unable to correspond to the target subset containing the discontinuity from the reference image. This inherent deficiency of DIC often leads to erroneous fracture properties measured near the crack tip. Methods have been developed to improve measurements near cracks. A subset splitting technique was developed that is capable of determining displacement jumps and displacements right by the discontinuity (Poissant and Barthelat, 2010).

Recently a method was developed that uses peridynamics to numerically determine the regions with poor quality correlation by using the accurate displacement field measurements as boundary conditions. The method is capable of determining crack displacements and characterising damage of brittle materials (Turner, 2014).

2.4.5 Summary

This chapter delineated the development over the last century of numerical and experimental methods employed to characterise the cracking behaviour of materials. Significant development was made in fracture mechanics, with characterising brittle and ductile cracking behaviour. Although peridynamics is a relatively new field, where other conventional methods fail, it has found numerous solutions for predicting and analysing crack propagation. Lastly, the DIC method has many advantages above other standard measuring techniques and bridges the essential gap between computational and experimental mechanics.

The following salient points were identified from the literature:

- Peridynamics is capable of naturally solving cracks, due to the integral formulation which is simplified by using the force sum of the intact bonds and the bonds exceeding the critical stretch, s_c does not contribute to the system.
- Peridynamics lacks from experimental investigation to determine s_c, however, it was found that the critical energy release rate, G_{Ic} and fracture toughness, K_{Ic} from LEFM relates directly to s_c (Equation 2.15).
- Tests that validated the use of K_{Ic} for determining the critical stretch input still lacked errors of up to 15%, however, served as validation and motivation that the

relationship between experimental fracture mechanics and numerical peridynamics exists.

- The validation tests followed an approach of applying strain gauges to the material surface ahead of the crack path, which limits the reliability of the measurements after fracture.
- The mixed Mode crack behaviour was also investigated and simulated in peridynamics, where accurate crack inclinations and maximum loads were predicted, which motivates to further investigate mixed Mode crack behaviour.
- The G_{Ic} can be related to the fracture toughness, K_{Ic}, through Young's Modulus of Elasticity, where K_{Ic} can be experimentally determined with guidance from ASTM standards. The ASTM E399, E1820 and E1823 can be used to design specimens, prepare specimens (through fatigue pre-cracking), and determine fracture toughness values and resistance curves of metallic materials.
- In order to determine an accurate fracture toughness the precise position of the crack tip is of great importance (Hild and Roux, 2006).
- Ductile cracking is a complex material behaviour and cannot be characterised by a single failure parameter, and due to the elastic-plastic deformation LEFM no longer holds. EPFM can be utilised, where the J-integral or J-R-curve can be used to characterise the elastic-plastic behaviour .
- The unloading compliance technique has the advantage of using only one specimen to obtain an entire J-R-curve, which saves cost on material and testing time.
- Most mixed Mode test methods have restrictions, where different specimen types and test configurations are needed to test different loading modes, where the Modified Arcan test only need one specimen type. Alternating between different modes simply requires turning the fixture in the desired inclination of loading. Moreover, with the Modified Arcan test it is possible to load a specimen in Mode I, Mode II and mixed Mode, with increments of 15 degrees, which totals to seven different loading modes.
- DIC has the advantage above conventional experimental measuring techniques of measuring full displacement fields without contacting the specimen, therefore it is classified as a non-intrusive method.

- The DIC algorithm can be applied to any resolution digital image, however, it has to adhere to the following prerequisites: good quality and focus of digital images; illumination is required during testing; the test specimen has to have a random grey intensity surface pattern (speckle pattern).

- Using larger subsets with large speckles yield the most accurate displacement measurements for homogeneous deformation and smaller subsets would result in a more refined crack path measurement when cracks appear in the deformed image.

- DIC has been successfully extended to failure models in application of fracture mechanics, however, rarely has work been done with DIC and peridynamics. There exists a large potential with the capabilities of peridynamics to characterise damage and determine failure properties using full field displacement measurements.

- The inherent deficiencies of DIC measurements near cracks introduces a certain degree of inaccuracy in the results, which will need to be taken into account. However, resolving this issue is not the focus of this project.

- Regardless of the deficiency of measuring accurate displacements near cracks, DIC is a powerful experimental technique and is cost effective for obtaining full field kinematic measurements. DIC measured full field displacements can be used to bridge the gap between experiments and numerical models (Roux et al., 2009). This has been shown for solid mechanics applications and can also be used for applications in peridynamics to characterise failure of materials (Turner, 2014).

Chapter 3

Motivation and Research Methodology

The aim of this chapter is to provide background to the project and to formulate the hypothesis. The objectives of this thesis and the research methodology are outlined.

3.1 Background

Foster, Silling and Chen found that the fracture toughness from linear-elastic fracture mechanics (LEFM) can be used to compute the peridynamic critical stretch to predict brittle linear elastic failure. Good qualitative comparisons were shown between simulations and camera data of dynamic crack initiation experiments, as seen in Figure 3.1. Madenci and Oterkus (2014) used the K_{Ic} values from experiments performed by Ayatollahi and Aliha (2009) as inputs to model Mode I, Mode II and mixed Mode loadings, where pure shear was regraded at 62.5 degrees. Good correlation was found for the Mode I and Mode II failure loads compared to the experiments. Relatively close results were obtained for the mixed Mode loads, where the error range was below 15%, as shown in Figures 3.2.

Foster et al. further stated that the critical energy release, G_c rate or J-integral, can be used as direct inputs to model elastic-plastic failure. Foster and Silling attempted to use a K_{Ic} value as peridynamic input in a blind simulations challenge to predict the nucleation, initiation and propagation of ductile failure in engineering materials. The

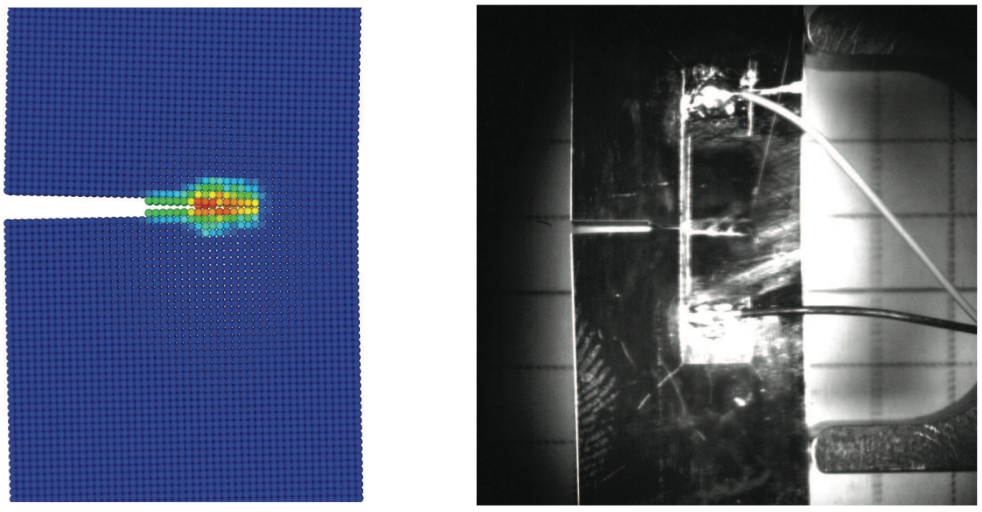

FIGURE 3.1: Visual comparison of peridynamic simulation to experiments (Foster et al., 2011).

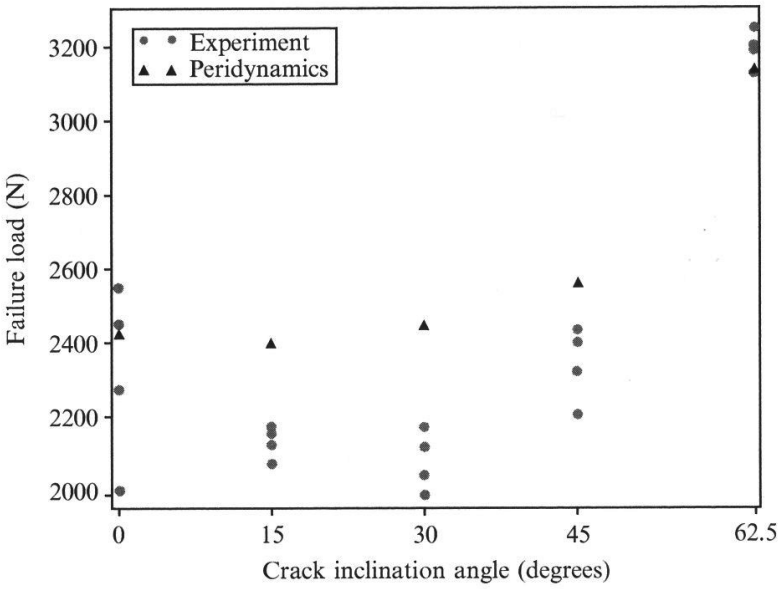

FIGURE 3.2: Comparison of failure loads at crack inclination angles between peridynamics and experiments using K_{Ic} as input (Madenci and Oterkus, 2014).

challenge was proposed in the ductile failure x-prize coordinated by Sandia National Laboratories. The peridynamic peak force results had an error of 39%, where the critical energy criterion was used to determine the critical stretch. The main discrepancy in results was interpreted due to using a linear-elastic energy criterion as input to predict elastic-plastic failure, as stated in Appendix B4. of the report (Boyce et al., 2011). Also, as before mentioned, Madenci and Otterkus stated that for complex material behaviour,

which is regarded as ductile failure, there is currently no simple approach to determine the critical energy or critical stretch.

3.2 Motivation

This thesis was partly motivated by the shown results of Foster et al., where it was found that the elastic energy release rate can be used to determine the critical stretch in peridynamics. However, limited validation work has been found in literature. Also, it was stated that the J-integral can be used to determine the critical stretch to model elastic-plastic failure. To the author's knowledge this has not been implemented. It was interpreted that the discrepancies found in Figure 3.2 for the mixed Mode failure loads could be due to using Mode I failure criteria to model mixed Mode shear failure. As found in literature in Section 1.3.8, Mode I failure criteria cannot be used to describe shear failure.

Foster et al. used strain gauges and digital images to validate the use of a critical energy release rate criterion to determine the critical stretch to model failure in peridynamics. Foster's work further motivated the consideration towards the use of more accurate optical methods of measurement, such as Digital Image Correlation (DIC). Good potential was found in previous work where a novel peridynamic-based algorithm was used to incorporate DIC full displacement fields to accurately plot damage fields caused by cracking (Conradie et al., 2014). The algorithm shows potential for further development by implementing the J-integral to determine the critical stretch of a bond for more reliable estimates.

3.3 Hypothesis

Can the J-integral be used to compute the critical stretch in peridynamics to model material failure?

3.4 Objectives

The objectives of this thesis were divided into four categories.

1. Obtain experimental J-integral values using standardised fracture mechanics tests of brittle and ductile materials. Also, obtain DIC full surface measurements from the tests.

2. Develop a peridynamic-based algorithm that implements the J-integral derived critical stretch and DIC full displacement field measurements to estimate and map crack damage of materials. The results will serve as qualitative validation of the hypothesis.

3. Use the J-integral values from the brittle materials to compute the critical stretch for input in peridynamic simulations for validation of the critical energy release rate based failure criterion, as proposed by Foster.

4. Use the J-integral values from the ductile materials to compute the critical stretches for input in peridynamic simulations to test the validity of the hypothesis.

3.5 Methodology

The methodologies followed to achieve the four objectives are summarised in the corresponding four subsections.

3.5.1 Experimental techniques

Standardised fracture mechanics tests on Compact Tension (CT) specimens are performed to measure the J_{Ic} values of brittle and ductile materials using ASTM-E1820-11.

Polymethyl methacrylate (PMMA), generally referred to as Perspex, is considered to be a brittle linear-elastic material and is used to obtain J_{Ic} values. According to LEFM the critical energy release rate is equal to the J-integral for a linear-elastic material, as shown in Section 1.3.8. The Perspex J_{Ic} values serves as input in peridynamic models to validate the critical energy release rate based failure criterion for predicting Mode I brittle linear-elastic failure, as proposed by Foster et al. (2011).

Stainless steel 304L and aluminium 1200H4 serves as ductile materials. The J-R-curves and J_{Ic} values are obtained according to ASTM-E1820-11. The values are used as inputs in peridynamic models and compared to the experimental Mode I failure loads.

Non-standardised mixed Mode tests on Modified Arcan specimens are performed on Perspex, stainless steel and aluminium for Mode II and mixed Mode fracture. The results and failure loads from the tests are subsequently used to compare to peridynamic models.

Digital Image Correlation (DIC) full field measurements of the fracture surfaces were obtained during testing. Full maximum normal strain fields are used to compare crack propagation paths, visually compare mixed Mode ductile fracture and the displacement fields are used as input in the peridynamic-based algorithm.

3.5.2 Peridynamic-based algorithm

The peridynamic-based algorithm is developed using *MATLAB® R2012a* (2012). It implements a J_{Ic} derived critical stretch and the two-dimensional DIC measured full displacement fields as material points and imposed displacements. It determines a full peridynamic damage field caused by cracking for brittle materials and plots a full damage field caused by plastic deformation of ductile materials.

3.5.3 Modelling brittle cracking

The test measured J_{Ic} value of Perspex is used to determine the critical stretch and is used as input in peridynamic simulations. An open source peridynamic code from the Sandia Corporation, called Mingus (Turner, 2013), was used to model the Arcan tests.

The Mode II and mixed Mode Perspex Arcan tests are also modelled using the Mode I critical energy release rate similar to the approach followed by Madenci and Otterkus. Also, Mode II energy release rates are obtained from literature to determine the critical stretch and used to determine the critical stretch for modelling Mode II and mixed Mode failure of Arcan models. Correlations between the two approaches are made and compared to the test failure results.

3.5.4 Modelling ductile failure

Mode I Arcan tests on stainless steel and aluminium are modelled using Mingus. The J_{Ic} values derived from the J-R-curves are used to determine the critical stretch values of the

particular materials to obtain the ductile failure loads. Furthermore, threshold J values with minimal crack extension, obtained from the J-R-curves, are used to determine the critical stretch values to obtain failure loads. The respective failure load results of the ductile materials are compared to determine whether the critical energy release rate or threshold energy release rate is most appropriate to determine the failure loads.

Chapter 4

Experimental Techniques

This chapter describes the experimental procedures and provide the input parameters required for further processing. The results from the material failure tests and Digital Image Correlation (DIC) analyses are provided in Chapter 5.

4.1 Introduction

The test procedures required to determine the critical energy release rates, i.e. J-integral of brittle and ductile materials, are provided. The J values are of importance to use as input in the peridynamic models. Standard tests were performed on Perspex Compact Tension (CT) specimens to the J_{Ic} values and brittle failure loads. Stainless steel 304L and aluminum 1200H4 CT specimens were tested to obtain the respective J_{Ic} values, J-R-curves and ductile failure loads.

Arcan mixed Mode tests were performed on Perspex to obtain brittle loads at different inclinations. Arcan Mode I failure loads of steel and aluminium tests were required to compare to ductile failure simulations. Furthermore, Perspex specimens were tested in mixed Modes to obtain the different brittle crack growth directions.

DIC measurements were acquired during testing. The results were required to characterise brittle cracking and plastic deformation in different Modes of loading. The full field measurements are needed for visual qualitative comparisons of tests and simulations. Also, the full field surface displacements are required for post-processing.

4.2 Test methods

The CT specimen and fixture designs, preparation and testing were done according to ASTM standards. Below is a list of standards that were used:

- ASTM-E399-09- 'Standard Test Method for Linear-Elastic Plane-Strain Fracture Toughness K_{Ic} of Metallic Materials'
- ASTM-E1820-11- 'Standard Test Method for Measurement of Fracture Toughness'
- ASTM-E647 11-'Standard Test Method for Measurement of Fatigue Crack Growth Rates'
- ASTM-E1823-11-'Standard Terminology Relating to Fatigue and Fracture Testing'

The Arcan test is a non-standardised test, therefore the specimen and fixture designs, and testing was done according to literature. The specimen preparations were, however, also done according to standard:

- ASTM-E1820-11- 'Standard Test Method for Measurement of Fracture Toughness'

4.3 Material and specimen details

4.3.1 Material selection

The main motivation for the materials was to determine the J values to use as input in the peridynamic failure models. Perspex was tested to measure the critical energy release rate of a material which was regarded as a brittle linear-elastic material. Stainless steel and aluminium were tested to obtain the J_{Ic} values and J-R-curves of ductile materials. The main difference between stainless steel and aluminium is ductility. Aluminium tends to plastically deform more extensively than that observed in stainless steel. This is of interest to observe the validity of using fracture mechanics to determine the J-R-curve of aluminium and to subsequently predict failure.

The relevant material properties used in subsequent calculations are given in Table 4.1.

TABLE 4.1: Material properties

Material	E (GPa)	ν	σ_Y (MPa)
Perspex	2.5	0.35	75
Stainless steel 304L	193	0.3	170
Aluminium 1200H4	70	0.3	120

Note that these material properties were not experimentally determined and were obtained from literature. Perspex material properties were obtained from *Material: PMMA* (n.d.), where E range from 1.8 - 3.2 GPa. Young's modulus was assumed at 2.5 GPa. Stainless steel 304L and Aluminium 1200H4 material properties were obtained from *CES EduPack* (2013).

Stainless steel 304L is commonly used in power plants (Ashbya and Smidmana, 2010) and the results from this thesis can relate to specific material interest in the EPPEI program.

4.3.2 Specimen details

CT and Arcan specimens were used for testing, which are shown in Figure 4.1. CT specimens were designed according to ASTM E399 specifications and were used for measuring the J_{Ic} of each material. The Arcan specimens are non-standard and were designed according to literature and practical considerations. Specimen designs are given in Appendix A.

Figure 4.1 indicates the relevant specimen dimensions and Table 4.2 gives the dimensional values for each material specimen. These parameters are subsequently used for fatigue precracking of the ductile specimens.

4.3.3 Specimen preparation

J_{Ic} testing requires that the initial crack be sharp. An artificial sharp crack cannot be achieved by machining a narrow notch in a specimen. The notch would not provide

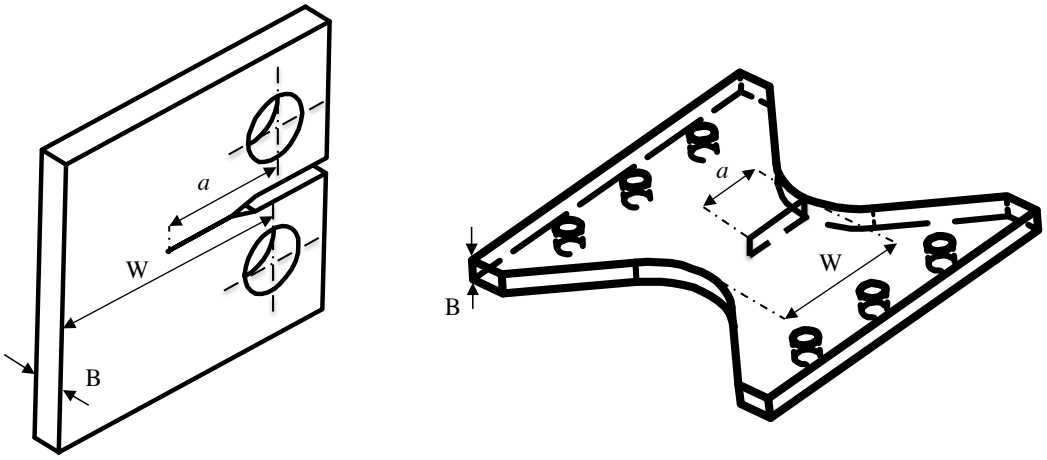

(a) (b)

FIGURE 4.1: CT and Arcan specimen dimensions.

TABLE 4.2: Specimen dimensions

Material	W (mm)	B (mm)	Notch length (mm)
Perspex CT	50	12	12
Perspex Arcan	80	12	no notch
Stainless steel CT	50	3	25
Stainless steel Arcan	80	3	10
Aluminium CT	50	3	25
Aluminium Arcan	80	3	10

satisfactory J_{Ic} measurements. Therefore, specimens are typically loaded in fatigue to grow a natural sharp crack.

Precracking Perspex specimens, however, were made with an initial hacksaw and razor cut to produce a sharp crack in accordance to ASTM-E399, Equation 2.28. Guides were followed according to Section 8.1.2 in Anderson (2005) on precracking of nonmetals (see Figure 4.2 for illustration).

The CT and Arcan stainless steel and aluminium specimens were fatigued in accordance to ASTM-E399, E647 and E1823. The fatigue testing machine was an Instron® servo-hydraulic, which was used to cyclically load the specimens and grow fatigue cracks. The

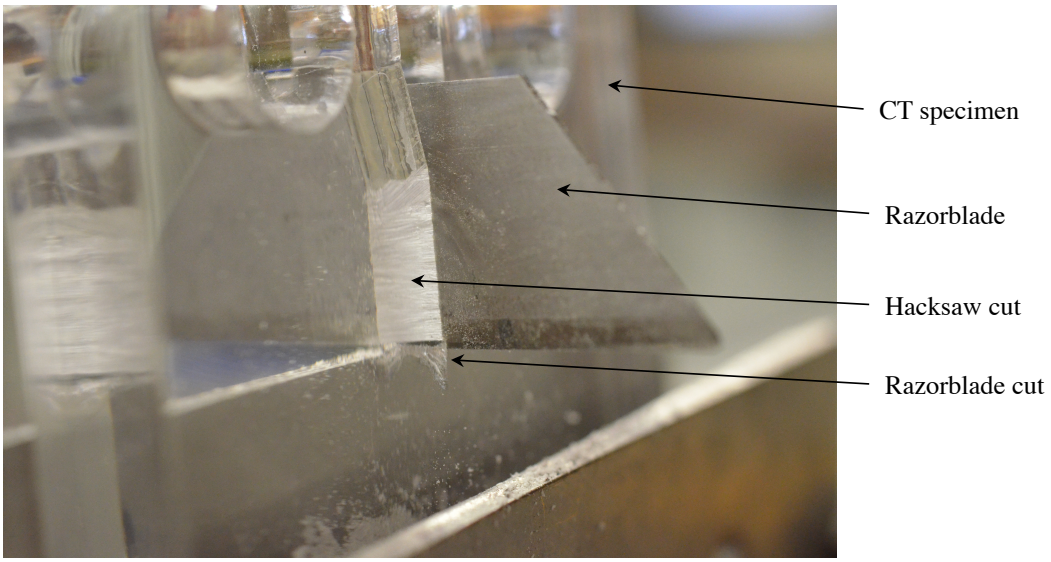

FIGURE 4.2: Sharp crack cut in CT Perspex specimen with razor blade

specimen preparations were done at the University of Cape Town at the Department of Materials Engineering. The fatigue crack growth parameters and load cycles are given in Table 4.3.

The maximum load P_{max} of the CT specimens was determined according to ASTM-E399 with:

$$P_{max} = \frac{Bb^2\sigma_Y}{2W + a}0.6 \tag{4.1}$$

where a was taken as the notch lengths given in Table 4.2.

TABLE 4.3: Fatigue crack growth parameters

Specimen	Material	f (Hz)	P_{max} (kN)	P_{min} (kN)	R	N $cycles$
CT	304L	10	2.74	0.274	0.1	15 000
CT	1200H4	10	2.42	0.242	0.1	11 000
Arcan	304L	10	12	1.2	0.1	50 000
Arcan	1200H4	10	4.5	0.45	0.1	80 000

According to ASTM E399 CT specimens are required to have a minimum fatigue crack length of $0.025W$ or 1.3 mm, whichever is largest. The CT specimens typically required

less cycles before the desired crack length developed. To the author's knowledge there exists no fatigue crack growth approaches for Arcan specimens, therefore loads were estimated according to SENT formulation and loading was monitored until fatigue crack lengths were typically 2 mm. The SENT formulations were found in Anderson (2005). Since the Arcan method is not standarised, a trial and error pre-cracking procedure was followed, where some specimens formed plastic zones near the crack tip during loading. In the case where a fatigue crack plastically deformed, the material effectively toughens and the specimen does not suffice for J_{Ic} measurement.

4.4 Fracture toughness testing

CT specimens were tested to obtain unloading compliance curves according to ASTM-E1820. From the curves the non-linear energy release rates, i.e. J values, were determined to construct the J-R-curves, which were required to obtain the non-linear critical energy release rate, J_{Ic}.

The experimental setup, test procedure, formulations and parameters used to determine the J values and construct the J-R-curve are given in this following section.

4.4.1 Experimental setup

The CT fixture was designed according to ASTM-E399. The fixture design drawings are given in Appendix A. Figure 4.3 shows the typical CT test setup. The figure shows the specimen pinned between the clevises and connected to the tensile machine. CCD cameras are directed towards the specimen surface for full field measurements. The specimens were tested in a Zwick® Z250 tensile machine. The load and displacement information were obtained from a Zwick® 250 kN load cell. The specimens were tested at ambient temperature. The full field measurements were made with LaVision® CCD cameras and software. The tests were performed at Stellenbosch University at the structures laboratory of the Structural Institute of the Department of Civil Engineering.

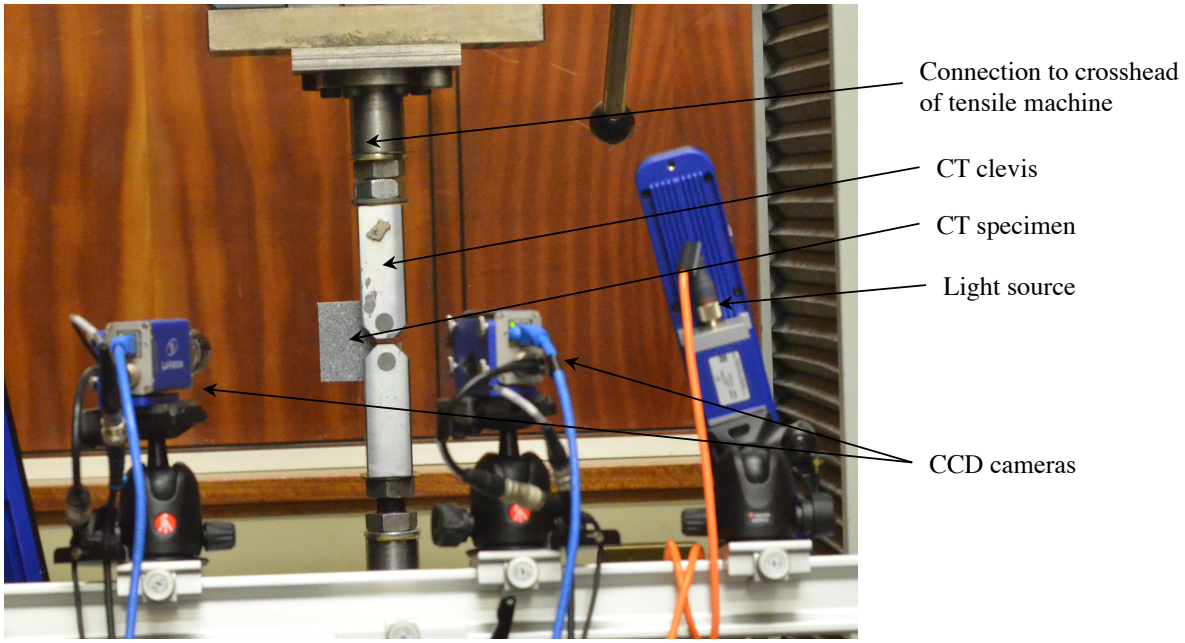

FIGURE 4.3: Typical CT test setup

4.4.2 Test procedure

CT tests were performed in accordance to ASTM-E1820. The unloading-compliance method was used to generate the load/unloading-displacement curve, as illustrated in Figure 2.15.

ASTM-E1820 specifies a load-unload rate of between $0.01b_o$ and $0.005b_o$. The load-unload rate was specified at 1.5 mm/min. To do this, a specimen was loaded by 3 mm and then unloaded by 1.5 mm to construct the load-unloading curve and obtain prominent compliance unloading gradients. The same displacement rate was used for all CT material tests.

The unloading of the specimen allows one to obtain the compliance gradient of each unloading sequence. Ductile materials exhibit elastic-plastic behaviour and several unload sequences were performed. As opposed to Perspex which exhibited a brittle cracking behaviour and only a single unloading sequence was achieved before the crack fully propagated.

4.4.3 Fracture toughness measurement

The J values of Perspex CT specimens require J_{el} and J_{pl}. The J_{el} values were determined with Equation 2.34 and J_{pl} values were determined using Equation 2.37.

Determining the J_{el} values the geometry factor for a normalised crack length a/W for CT specimens was required. The standard formulation is given as:

$$f(a/W) = \frac{2 + a/W}{(1 - a/W)^{3/2}}[0.866 + 4.64(a/W) \\ -13.32(a/W)^2 + 14.72(a/W)^3 - 5.60(a/W)^4] \tag{4.2}$$

The crack length extensions were determined according to the standard formulation for CT specimens as:

$$a_i/W = 1.000196 - 4.06319u + 11.242u - 2106.043u^3 + 464.335u^4 - 650.677u^5 \tag{4.3}$$

where the initial crack length of all the CT specimens are given in Table 4.4 and,

$$u = \frac{1}{[BEC_{c(i)}]^{1/2} + 1} \tag{4.4}$$

where $C_{c(i)}$ is the elastic compliance measured from the unloading line.

In order to determine the J_{pl} values the areas, A_{pl} under the load/unloading curves are required, as was illustrated in Figure 2.14. The gradient of each compliance and the corresponding displacement and load were used to determine the areas. The initial crack lengths given in Table 4.4 and Equation 4.3 were used to determine the a_i values of each unloading sequence.

The Perspex specimens only yielded a single A_{pl} value and therefore only possessed a single J_{Ic} value.

The ductile materials possessed several J values, which where used to construct the J-R curves. The curves plot the J values against crack extension. The crack extension was determined using Equation 4.4 and the initial crack lengths.

The J_{Ic} values of the ductile materials were determined according to ASTM-E1820, where a power curve was fitted to the values and exclusion lines were used to obtain the J_{Ic} values. Also, the standard specifies the evaluation of the K_{JIc}, which is converted

from the measured J_{Ic} values as:

$$K_{JIc} = \sqrt{E' J_{Ic}} \tag{4.5}$$

TABLE 4.4: CT specimens intial crack lengths

Material specimen nr.	$a_{initial}$ (mm)
Perspex CT 1	23.2
Perspex CT 2	24.5
Perspex CT 3	25.0
304L CT 1	22.2
304L CT 2	23.0
304L CT 3	26.8
1200H4 CT 1	27.0
1200H4 CT 2	27.2
1200H4 CT 3	27.0

4.5 Mixed Mode testing

The Modified Arcan test was used to test materials in Mode I, Mode II and several different mixed Mode inclinations. The fixture designs, test configuration and procedure are given in this section.

4.5.1 Experimental setup of the Arcan test

As mentioned the Arcan fixture is not a standarised test, therefore the fixtures and parts where designed according to literature and practical considerations. The designs were derived from work done by Sutton et al. (2003), Nikbakht and Choupani (2008) and Hosseini et al. (2008). However, the fixture and specimens were designed larger than that found in literature with DIC measurements in consideration. The motivation was to obtain larger full field measurements of the surface of the specimens during deformation and cracking.

Figure 4.4 shows a typical Arcan test setup. The design drawings are given in Appendix A. The upper and lower Arcan fixtures can be rotated and pinned at 0 to 90 degrees, with 15 degree increments. In the figure the specimen is positioned at 45-degrees.

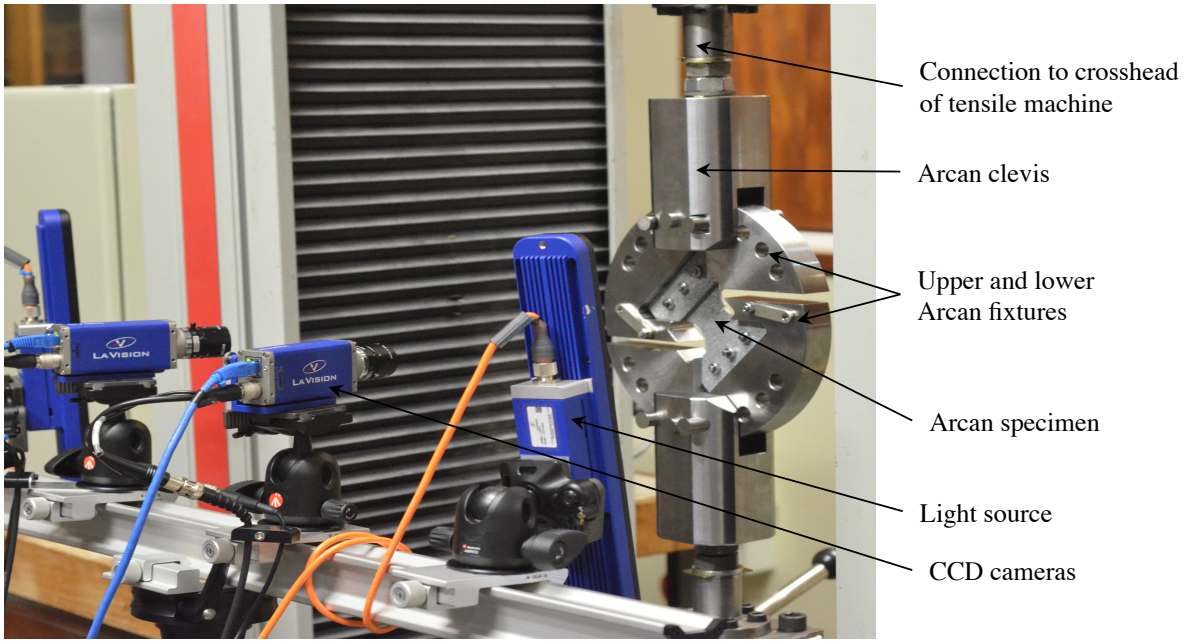

FIGURE 4.4: Typical Arcan test setup in 45-degree mixed Mode loading

The Arcan fixture consists of two half discs with a butterfly shaped indent in the middle to position the specimens. In the circumference of the discs are holes to alternate the Mode of loading by simply pinning the discs to the clevises. The clevises are connected to the tensile machine.

The specimens are connected with three bolts on each side of the fixtures with stainless steel clamps. The specimens were regarded as fixed at the bolts and once the specimens were loaded the sides of the fixture further prevent translation. However, the clamps cannot fully fix the specimens and small amounts of translation and bearing against the bolts were experienced. This was observed especially while testing ductile specimens, where relatively larger loads were concerned. The clamps provided sufficient fixity for the Perspex specimens, which were concerned with relatively low loads. However, the Mode II cracks still propagated into the supports, which could not be prevented. Nonetheless, the current work is concerned with recording load and full field displacement data from

Mode I, Mode II and mixed Mode cracking. In future work, more consideration will be put in the fixity of the specimens when testing different materials.

The specimens were tested in the Zwick® tensile machine and full displacement measurements were made with LaVision® CCD cameras.

Perspex Arcan specimens were tested in Mode I, Mode II and 15-degree mixed Mode increments. The loading rate was specified at 0.1 mm/min, which was assumed as a quasi-static loading rate to better capture the brittle crack propagation while acquiring images.

The stainless steel and aluminium Arcan specimens were tested in Mode I and 45-degree mixed Mode. The tests were performed by following the same procedure provided in the ASTM E1820 for CT tests. The loading rate was also specified at 1.5 mm/min.

The failure loads of the Perspex and maximum loads of the ductile materials were obtained from the 250 kN load cell of the Zwick® tensile machine.

4.6 Digital image correlation

As mentioned, DIC full field measurements were made during testing with LaVision® cameras and software. LaVision® is a 3D system that is capable of measuring out-of-plane deformation. It has an accuracy up to 0.01 pixels in the in-plane deformation and 0.02 pixels out-of-plane. Figure 4.3 and Figure 4.4 showed the camera and lighting setup during CT and Arcan testing, respectively.

4.6.1 Hardware details

The hardware components are listed and described below:

- CCD cameras with 5-megapixel resolution.
- Lenses have a focal length of 35 mm.
- LED lights sources were used. Strobe lights are emitted each time an image is taken. This prevents the influence of temperature increase, which can have an influence on measurements when using a continuous illumination.

- Cable arrangement consists of power cables, providing power to the cameras and the LED light source, and Ethernet cables transmit the image information to the computer through the Programmable Timing Unit (PTU).
- The PTU and a desktop computer feed in image information and analyse the images, respectively.

4.6.2 Specimen preparation

Speckle patterns were applied to the specimen surfaces before testing. This was achieved by spray painting a thin grey base over the specimen, followed by spraying black and white speckles over the surface. Figures 4.5, 4.6 and 4.7 shows typical speckle patterns on Arcan and CT specimens. Tests were performed within a relatively short time after the paint was applied. Aged speckle patterns can cause the paint to flake off and yield inaccurate full field measurements. Furthermore, the speckles were typically larger than three pixels to avoid poor correlation from noise during analysis (Lecompte et al., 2006).

4.6.3 Full field analysis procedure

Images were analysed with LaVision® DIC software. The analysis procedure is listed below:

- The relevant region of analysis was masked off on the specimens in the images, as illustrated in Figure 4.5 and Figure 4.6.
- ZNSSD correlation method was used to match subsets from the reference to the deformed images.
- Strain, in LaVision®, is calculated through central differencing, it is the relative displacement over a gauge length, where the gauge length, in DaVis®, is two times the step size.
- An 6^{th} order spline interpolation scheme, which is the accurate setting in LaVision®, was used for determining sub-pixel coordinates. This interpolation scheme results in less susceptibility to pixel locking.

- Square pixel × pixel subsets sizes were used in analyses. Subsets were overlapped by a specified pixel step size. As mentioned in Section 2.4.3, the subset size is a function of the speckle pattern size.

- There exists a trade-off between subset size and the accuracy of the analysis. Larger subsets yield more accurate strain measurements, where more pixel information effectively smooths out the noise. Smaller subsets yield less accurate strain measurements, where noise has a bigger influence and often results in non-physical strains. However, a more refined crack path is captured using smaller subsets.

4.6.4 Full field measurements and analyses

Images were acquired during Perspex Arcan tests, where specimens were loaded in Mode I, Mode II and 15-degree mixed Mode increments. The analyses were used to compare the crack propagation paths between loading Modes. Figure 4.5 indicates the region of analysis on a typical greyscale image of an Arcan specimen. Furthermore, full field measurements were made during CT testing. The region of interest was ahead of the crack notch were the cracks initiated. Figure 4.6 illustrates the typical region of analysis for CT specimens. Analyses were performed on Perspex CT test images , where coarse and fine subsets and step sizes were used.

Before the images of the tests were analysed noise floor checks where made. The noise floor is the error due to pixel noise determined from standard deviation of the full field displacements and pixels measured between two static images. It is obtained through acquiring two images of the unload specimen and determining the displacements. Table 4.5 gives the displacement and corresponding pixel error of each material specimen that was tested. Typically an acceptable displacement error is less than 10^{-3}, which all the tests adhered to as seen in the table.

Table 4.6 provides the the subset size and step size that was used for the analyses for the particular tests. Moreover, the table gives the pixel error and local strain accuracy of LaVision® for each subset size and step size combination.

The analyses on the CT specimen were performed to compare the difference in using relatively large and small subsets. Using large subsets yield more accurate displacement

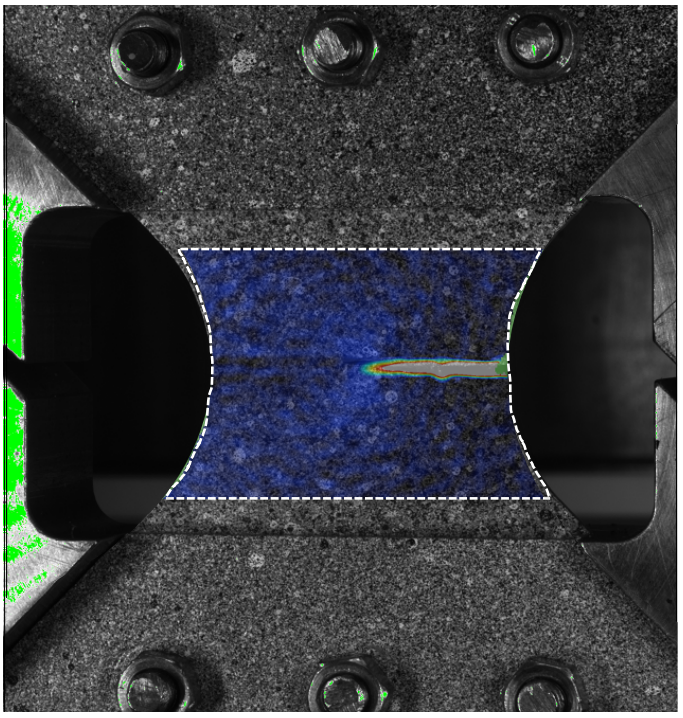

FIGURE 4.5: Typical region of DIC analysis for an Arcan specimen

measurements, however using small subsets would yield a more refined crack path position. The analyses are also subsequently used in the peridynamic-based algorithm to compare the influence of the subsets on the damage fields and crack resolution.

Figure 4.7 shows greyscale images acquired during Arcan tests on stainless steel and aluminium. The results from the analyses of the images are given in the following chapter. These analyses were performed to visually compare the mixed Mode ductile failure behavior of both materials.

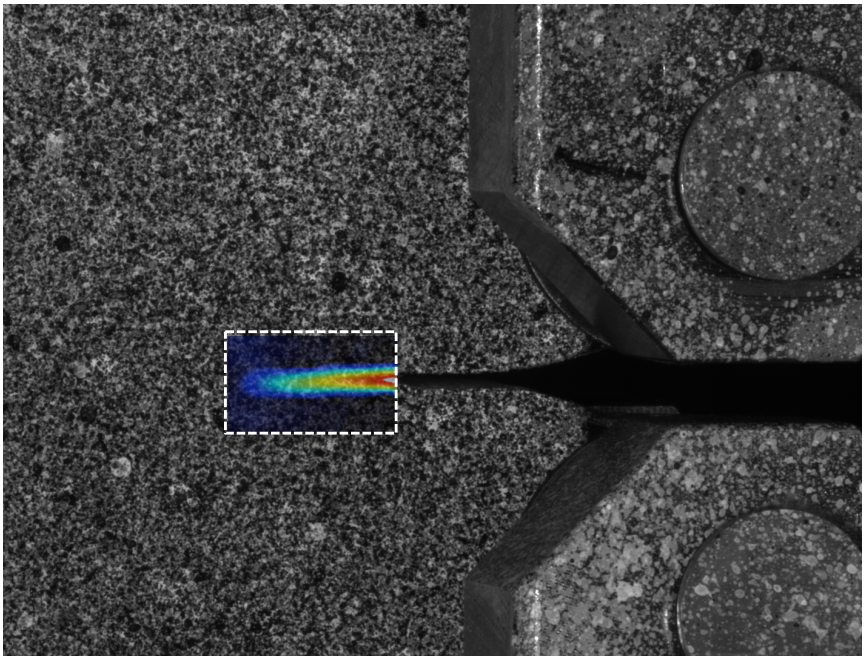

FIGURE 4.6: Typical region of DIC analysis on a CT specimen as indicated over the cracked region ahead of the notch

TABLE 4.5: Noise floor values of DIC tests

Specimen and Material	Displacement error (10^{-4}mm)	Pixel error (10^{-3})
304L CT 3	1.77	4.66
1200H4 CT 2	6.68	18.1
304L Arcan	3.33	80.5
1200H4 Arcan	4.89	11.8
Perspex Arcan 0 degree	14.0	43.0
Perspex Arcan 15 degree	11.0	29.0
Perspex Arcan 30 degree	6.70	17.0
Perspex Arcan 45 degree	3.60	9.50
Perspex Arcan 60 degree	4.88	12.7
Perspex Arcan 75 degree	6.90	18.2
Perspex Arcan 90 degree	3.98	10.4
Perspex CT	2.60	9.90

TABLE 4.6: Subset size and step size accuracies and uncertainties

Analysis type	Subset (pixels×pixels)	Step size (pixels)	Pixel error %	Local strain accuracy/uncertainty %
Arcan tests	31×31	6	0.1	0.117
Static error checks	31×31	15	0.1	0.047
CT coarse	31×31	12	0.1	0.059
CT fine	13×13	4	0.24	0.424

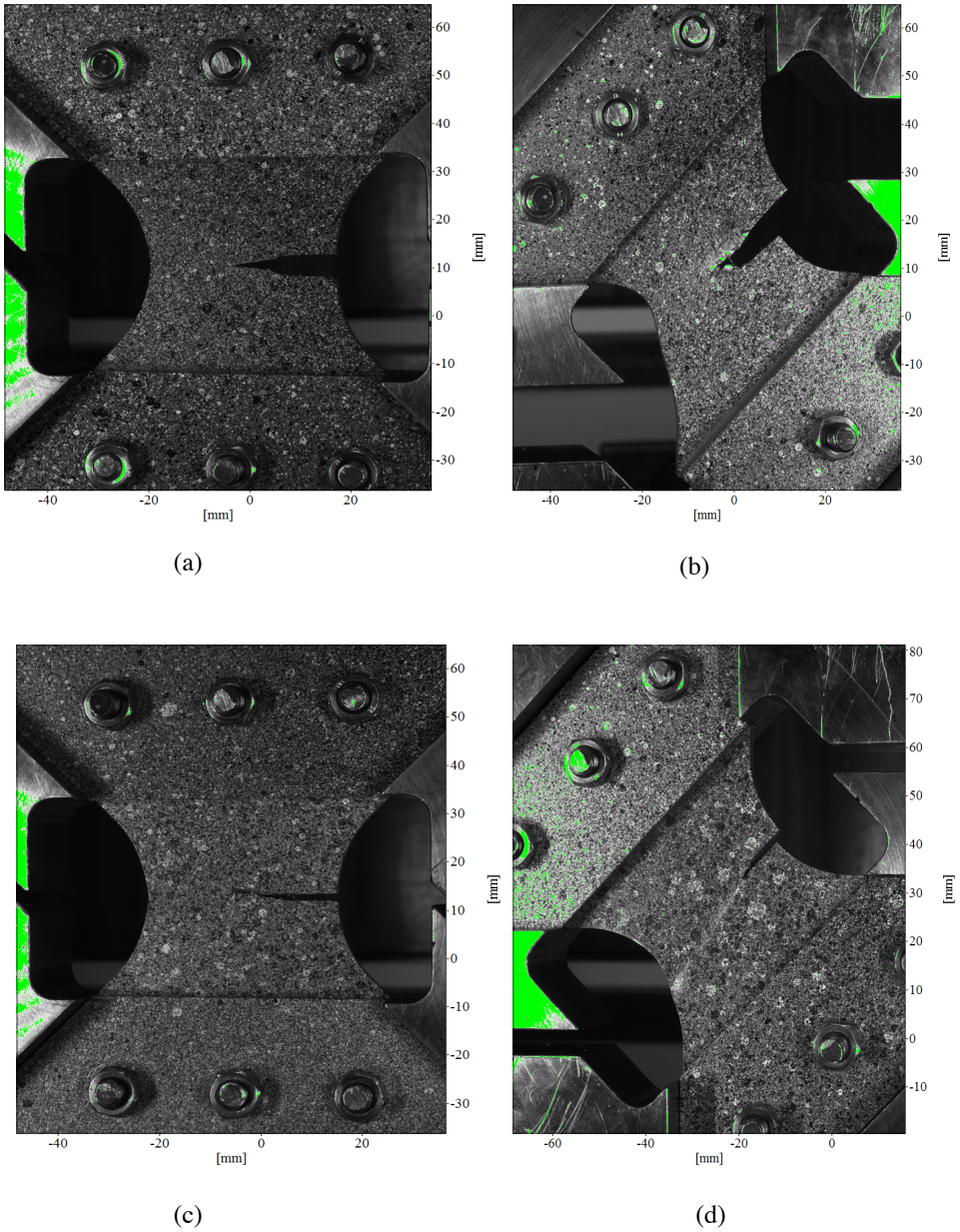

FIGURE 4.7: Greyscale images obtained from LaVision® of Arcan stainless steel loaded in (a) Mode I at $P = 29.25$ kN, (b) 45-degree mixed Mode at $P = 33.6$ kN, and aluminium loaded (c) Mode I at $P = 5.75$ kN, and (d) 45-degree mixed Mode at $P = 6.5$ kN

Chapter 5

Experimental Results

The results from the material tests and Digital Image Correlation (DIC) analyses described in Chapter 4 are presented in this chapter. The full field measurements are used for visual comparisons of mixed Mode fracture behaviours. Furthermore, the results are subsequently used to determine the critical stretch values as peridynamic modeling input parameters in Chapter 6.

5.1 Introduction

The results from the fracture toughness tests described in Section 4.4 comprise of the load-unloading displacement curves, J-R-curves and J_{Ic} values. The J-R-curves were constructed according to ASTM-E1820. The J_{Ic} values of the ductile materials were subsequently obtained from the curves. Furthermore, the full field measurements of the tests were compared for different Modes of loading, as well as using different subsets for the DIC analyses. Lastly, the procedure to obtain the peridynamic critical stretch is given.

5.2 Fracture toughness results

This section provides the J_{Ic} values of the Perspex and ductile materials. Note that J_{Ic} includes the energy absorbed from plastic deformation while cracking. Perspex was

regarded as a linear-elastic material and $J_{Ic} \simeq G_{Ic}$ was assumed. See Section 2.3.6 for difference between G_{Ic} and the J_{Ic}.

5.2.1 J_{Ic} results of Perspex

The load-unloading curves of the Perspex CT specimens are given in Figure 5.1. As seen in the figure, only a single or a pair of unloading sequence was achieved in the tests. This was due to the uncontrollable brittle cracking nature of Perspex.

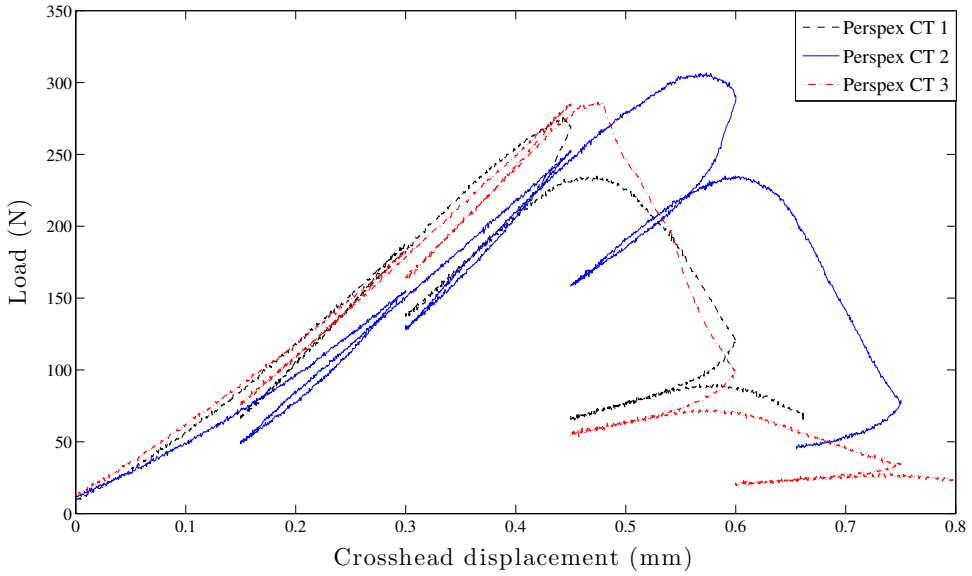

FIGURE 5.1: Unloading compliance of Perspex CT tests

The maximum loads of each specimen are given in Table 5.1. The parameters required to determined the J_{Ic} values for each specimen according to Equation 2.34 and Equation 2.37 are also given in Table 5.1.

The J_{Ic} results correlated well with fracture toughness values found in literature, where the average value correlated within 4%. Ayatollahi and Aliha (2009) found similar results of 0.771 J/mm^2, which was determined from 1.48 MPa$\sqrt{\text{m}}$ according to Equation 2.25, where plane strain was assumed. However, the results were not determined from standarised tests. It is recommended to perform more tests to acquire more accurate J_{Ic} values. As a resolution to reduce the discrepancy between values, the average J_{Ic} value is used as input in simulations.

TABLE 5.1: Perspex fracture toughness results

Specimen	P_{max} (N)	a (mm)	$f(a/W)$	A_{pl} (mm^2)	J_{el} (J/mm^2)	J_{pl} (J/mm^2)	J_{Ic} (J/mm^2)
Perspex CT 1	275	23.2	8.55	86	0.028	0.609	0.636
Perspex CT 2	306	24.5	9.23	105	0.033	0.782	0.815
Perspex CT 3	286	25.0	9.52	101	0.032	0.766	0.798
Average							0.750

5.2.2 J-R-curves and J_{Ic} results of ductile materials

The load-unloading curves of the stainless steel and aluminum CT specimens are given in Figure 5.2 and Figure 5.3, respectively.

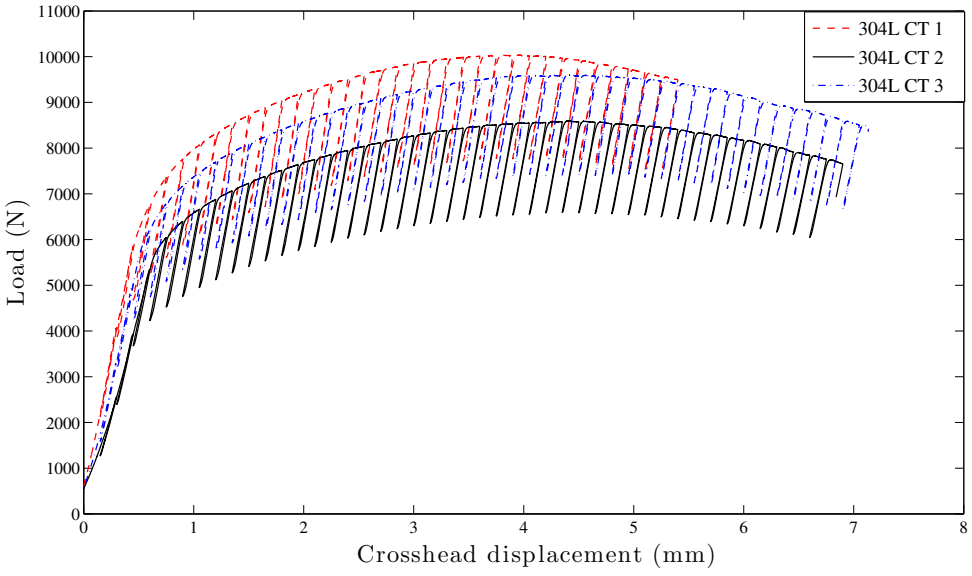

FIGURE 5.2: Compliance unloading curve of stainless steel 304L CT specimens

The expected unloading compliance lines are clearly seen in Figure 5.2 and Figure 5.3. The stainless steel results have a good correlation between specimens. However, the aluminium test results did not yield a good correlation, where 1200H4 CT 2 deviated from the other specimens. It is unsure why the specimen yielded at a lower load. The crack length for 1200H4 CT 2 was larger, however by a negligible difference and could not cause the large discrepancy. Therefore, it is recommended that more tests are required

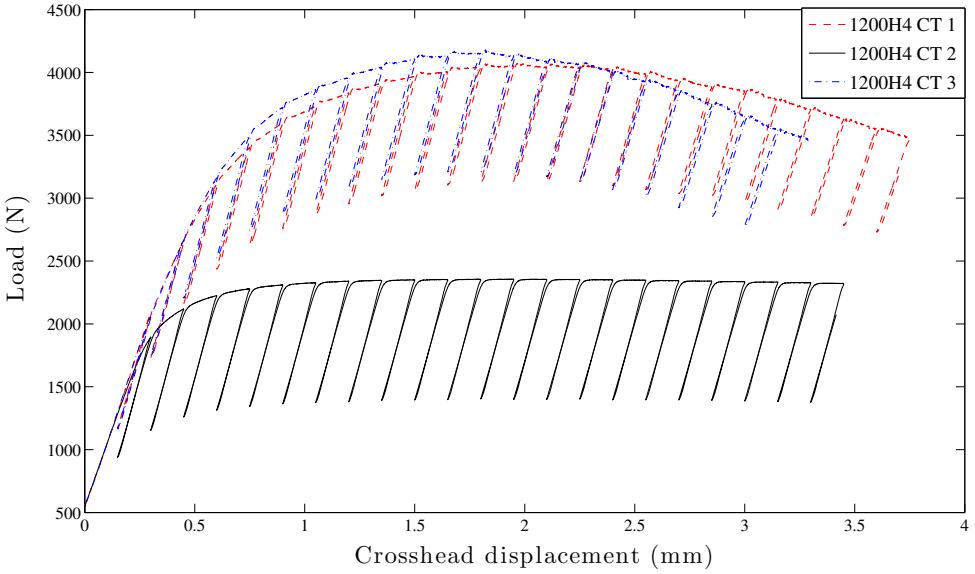

FIGURE 5.3: Compliance unloading curve of aluminium 1200H4 CT specimens

to obtain better correlating results. Nevertheless, the specimen was not discarded and its J-R-curve and J_{Ic} value were used in subsequent simulations to compare to the failure loads. It is argued that even though the specimen deviated from the norm, the dissipated energy should correlate to a similar maximum load in the simulations.

Table 5.2 gives the maximum loads and crack lengths. The crack lengths and the plastic areas underneath the unloading compliance curves were used to determine the J-R-curves according to ASTM E1820. Figure 5.4 and Figure 5.5 shows the J values plotted against crack extension of the stainless steel and aluminium specimens, respectively.

TABLE 5.2: Stainless steel 304L and aluminium 1200H4 fracture toughness results

Material and specimen nr.	P_{max} (kN)	a (mm)	J_{Ic} (J/mm^2)	K_{JIc} MPa$\sqrt{\text{m}}$
304L CT 1	10.0	22.2	408	294
304L CT 2	8.6	23.0	364	277
304L CT 3	9.6	26.8	452	309
1200H4 CT 1	4.1	27.0	176	116
1200H4 CT 2	2.4	27.2	112	93
1200H4 CT 3	4.2	27.0	170	114

Figure 5.4 shows the stainless steel J-R-curve where a single regression line is fit to 304L CT2 J values for illustration. Figure 5.5 shows the regression line of 1200H4 CT 1 and CT 2. It can be seen that the progression of J values for 1200H4 CT 2 are clearly lower. The threshold J values, however, correlated well for all specimens.

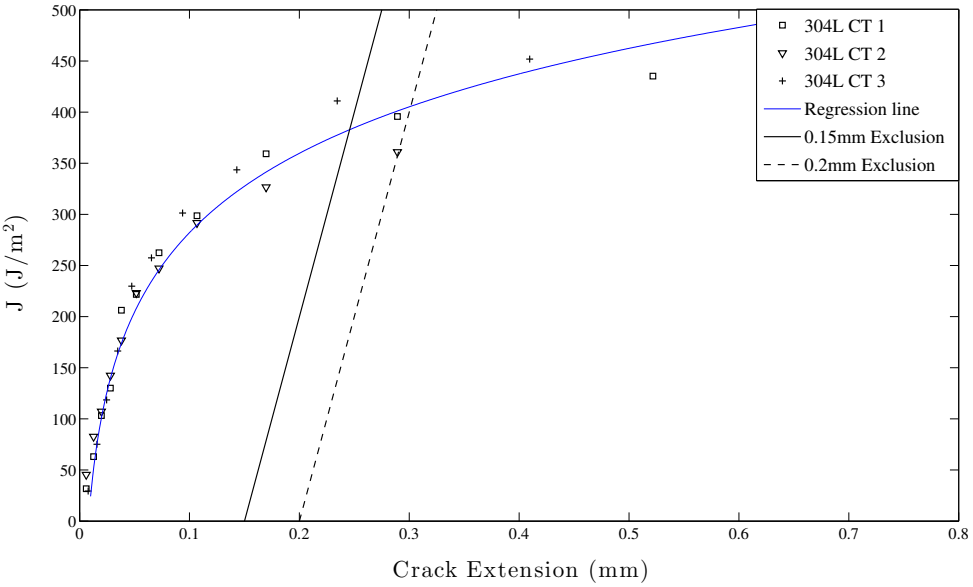

FIGURE 5.4: J-R-curve of stainless steel 304L.

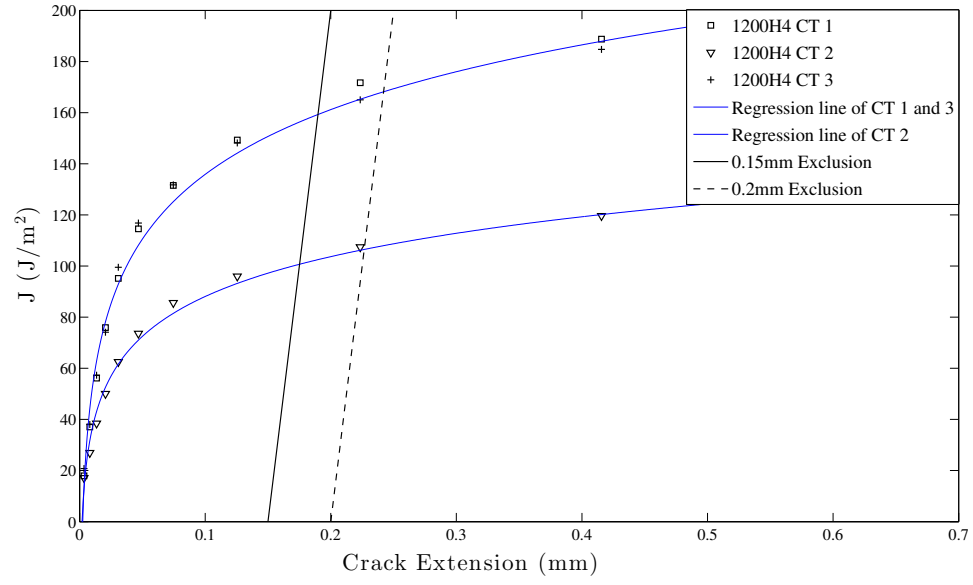

FIGURE 5.5: J-R-curve of aluminium 1200H4.

The K_{JIc} test results of the stainless steel 304L CT 2 shown in Table 5.2 compared the closest with 18% to a K_{Ic} of 228 MPa$\sqrt{\text{m}}$ found in literature (*Stainless steel - Grade*

304, 2014). The K_{JIc} test results of the aluminium 1200H4 CT 1 compared the closest with 6% to a K_{Ic} of 123 MPa$\sqrt{\text{m}}$ found in literature (*CES EduPack*, 2013).

Even though the standard procedures were followed, there are numerous reasons for the discrepancies of the J_{Ic} values. One main reason could be due to microstructural effects and the rolling direction during manufacture of the specimens. Furthermore, K_{Ic} plane strain elastic values from literature are used for reference, where the J_{Ic} test values are under plane stress conditions and specimens have undergone plastic deformation. Nevertheless, the J values closer to the threshold are more uniform, which is of importance for the peridynamic simulations. This point will be made evident in the following chapter.

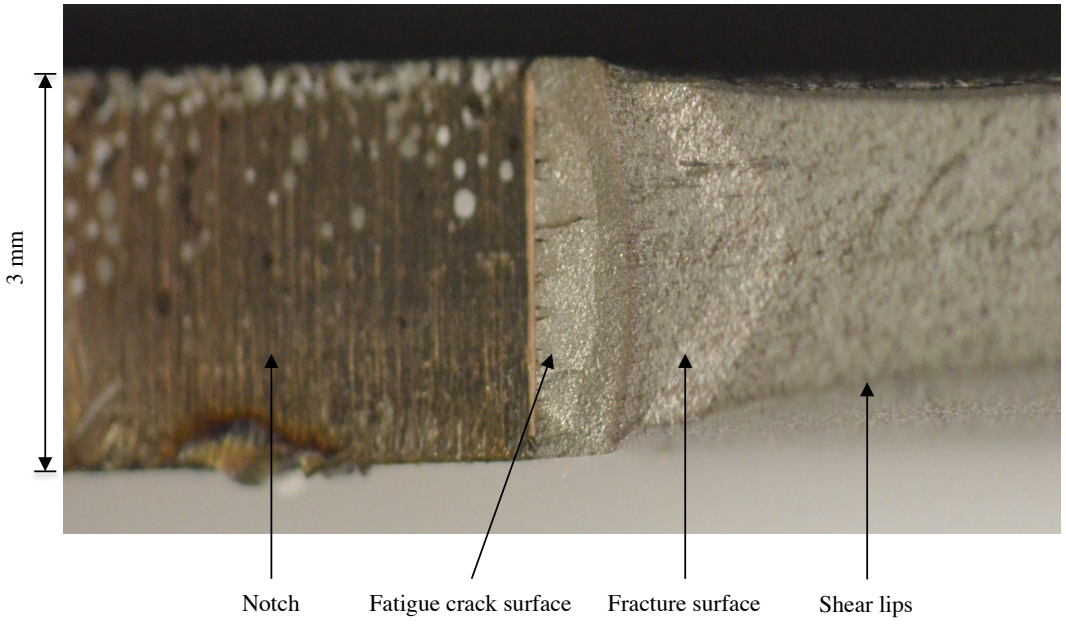

FIGURE 5.6: Typical fracture surface of stainless steel.

Figure 5.6 shows the fracture surface of a typical 3 mm thick CT stainless steel specimen. As seen next to the notch, the fatigued crack surface is indicated, which is followed by the fracture surface. The width of the specimen reduced and shear lips formed. This further motivated the use of the J-integral, which allows for this behaviour when testing thin metal specimens. Moreover, the shear lips are caused by plane stress at the surface of the specimen and plane strain to the center (Zuidema et al., 2003). Refer to Section 2.3.6 for plane strain and plane stress.

5.3 Digital image correlation measurements

The DIC results are provided in the following section. The plastic strain fields of the ductile CT specimens ahead of the notch are provided. Furthermore, the Arcan mixed Mode full fields are provided, where the plastic deformation caused by mixed Mode loading on the ductile materials are shown. Also, the brittle crack paths of the Arcan Perspex specimens are compared. Finally, the influence of using different subset sizes are compared and discussed.

5.3.1 Ductile failure full field results

Figure 5.7 and Figure 5.8 show the full maximum normal strain field measurements of stainless steel and aluminium, respectively. The region of analysis was indicated in Figure 4.6.

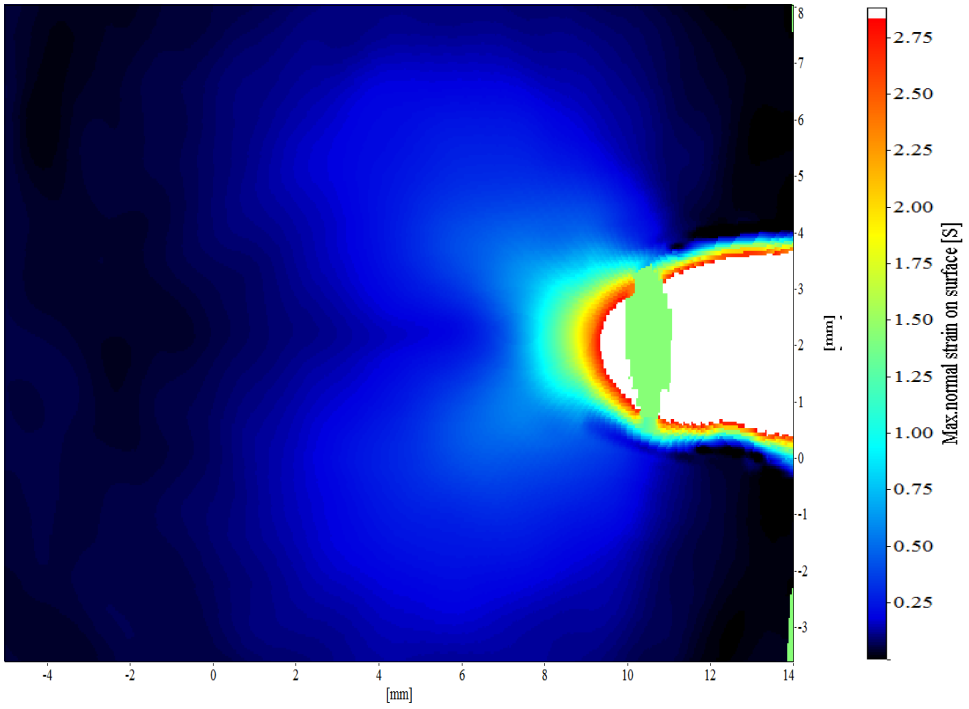

FIGURE 5.7: Full maximum normal strain field of 304L CT 3 at $P = 9.183$ kN

Figure 5.7 shows the typical plastic zone shape found in Mode I loading, as was shown in Figure 2.9. It was assumed that the maximum normal surface strains larger than the yield strain was plastic deformation. This was a simplified approach, however it was

used to illustrate the plastic deformation occurring ahead of the crack in the ductile materials.

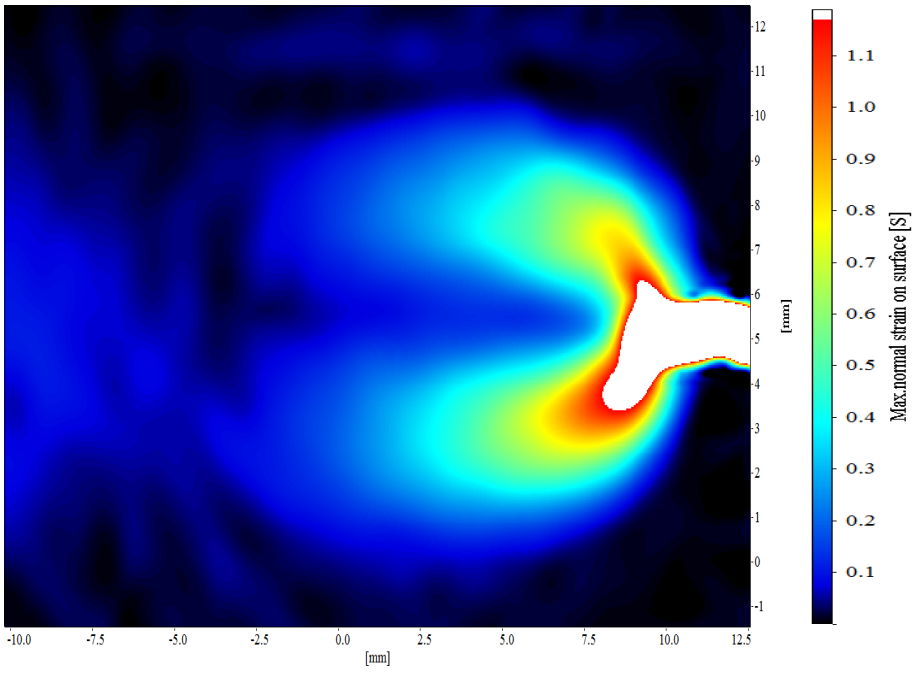

FIGURE 5.8: Full maximum normal strain field of 1200H4 CT 2 at $P = 2.350$ kN

Using Hook's law for a linear-elastic isotropic homogeneous material and Table 4.1 the yield strain of stainless steel 304L was 0.00088. The yield strain of aluminium 1200H4 was 0.0017. It was interpreted from the corresponding yield strains, Figure 5.7 and Figure 5.8 that excessive plastic deformation occurred ahead of the cracks of both ductile materials. However, the subset size of 31x31 pixels could have influenced the accuracy of the analyses. Using a larger subset size could have yielded a more accurate plastic strain representation ahead of the notch.

Also, note in Figure 5.7 the missing shading over the approximate cracked region. This was caused by excessive subset deformation, which results in poor correlation criteria. Commercial software often discards these subsets and leave missing data fields over cracks. This impediment often restricts the capability of DIC to determine the full deformation fields around cracks (Poissant and Barthelat, 2010). Although resolving this issue is not the focus of the thesis, this inherent incapability of DIC introduces a certain degree of inaccuracy that should be taken into account during post-processing.

Moreover, DIC measures non-physical strains over regions containing cracks, due to an assumption of continuous deformation. For example, when a crack forms, black pixels are shown. DIC assumes that the current black pixels in the subset are enlarged, which results in non-physical strain measurements.

Methods to resolve this impediment have been developed by Turner (2014) using a peridynamics-based DIC algorithm, which is suitable for solving discontinuities found in full surface fields. The analyses performed on brittle materials showed great potential. It is recommended to implement this approach for ductile materials. It would be of interest observing the ductile cracking capability of this algorithm when implementing the provided displacement fields.

5.3.2 Mixed Mode ductile failure results

Figure 5.9 and Figure 5.10 show a visual comparison of the full maximum strain fields of the Arcan Mode I and 45-degree mixed Mode of stainless steel and aluminium, respectively. The figures also provided the current load values.

Figure 5.9(a) and (b) show the Mode I and 45-degree mixed Mode stainless steel strain fields. It is seen that both specimens undergone excessive plastic deformation around the crack, where the crack position is regarded as the white shading.

Figure 5.10(a) and (b) shows the aluminium Mode I and 45-degree mixed Mode maximum normal strain results. Figure 5.10(b) shows plastic deformation throughout the whole ligament of the specimen. This phenomenon was also found by Hallback and Nilsson (1994). This suggest that plastic tearing is occurring throughout the specimen, rather than cracking.

It is argued that the plastic deformation from both materials would restrict using a fracture mechanics approach to determine the J-integral using the Arcan method. It is recommended to perform more tests at different mixed Modes using the Arcan method.

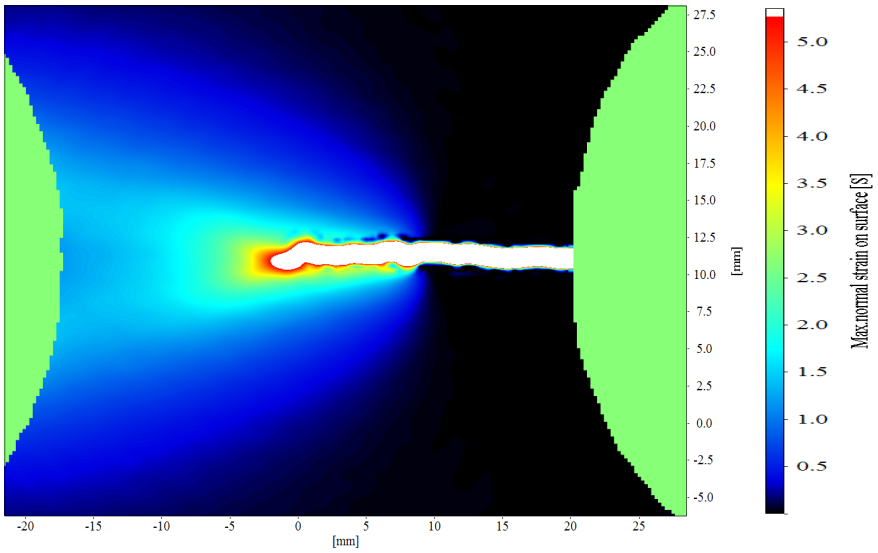

(a)

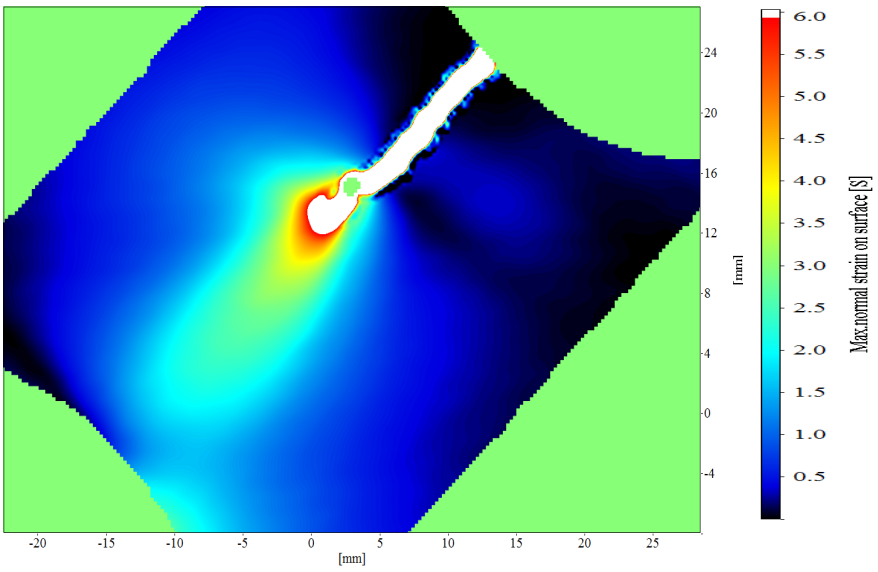

(b)

FIGURE 5.9: Visual comparison of maximum normal strain fields of Arcan stainless steel loaded in (a) Mode I at $P = 29.25$ kN and, (b) 45-degree mixed Mode at $P = 33.6$ kN

5.3.3 Mixed Mode brittle failure results

Figure 5.11 shows the full maximum normal strain field results of the Perspex Arcan tests, which serves as a visual comparison between Modes of loading and crack propagation angles in a brittle material. Full field measurements of Mode I, Mode II and

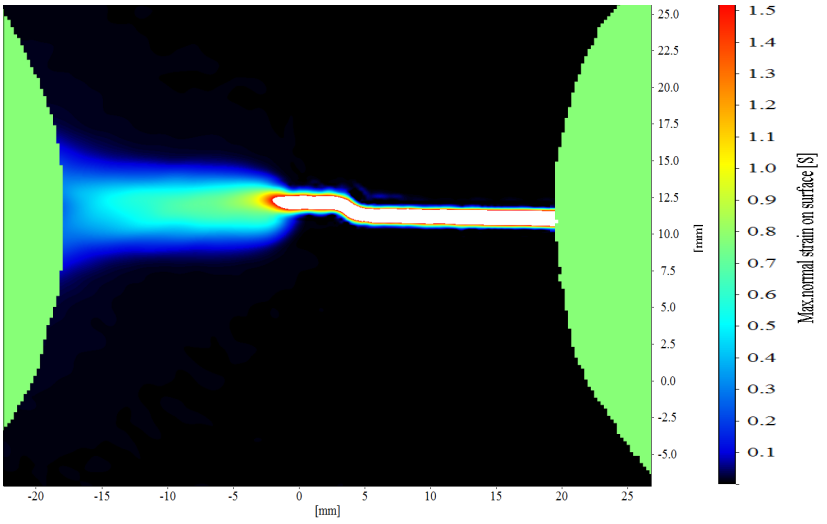

(a)

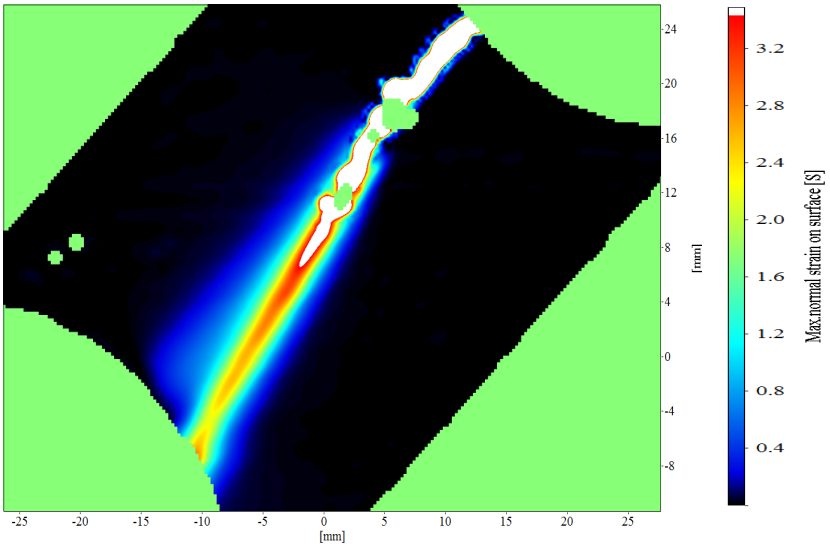

(b)

FIGURE 5.10: Visual comparisons of maximum normal strain fields of Arcan aluminium loaded in (a) Mode I at $P = 5.75$ kN, and (b) 45-degree mixed Mode at $P = 6.5$ kN

15-degree increments are compared. The load and Mode of each analysis are provided in the figure.

It is observed from Figure 5.11(a) to (e) that the crack opening directions are predominately in Mode I between 0 and 45 degrees. This is due to the crack that follows the direction of maximum principle stress. Figure 5.11(f) and (g) show the crack deviated and propagated towards the support of the fixture for loading Modes larger than 75 degrees. It is interpreted that the crack deviation was caused by the relatively large

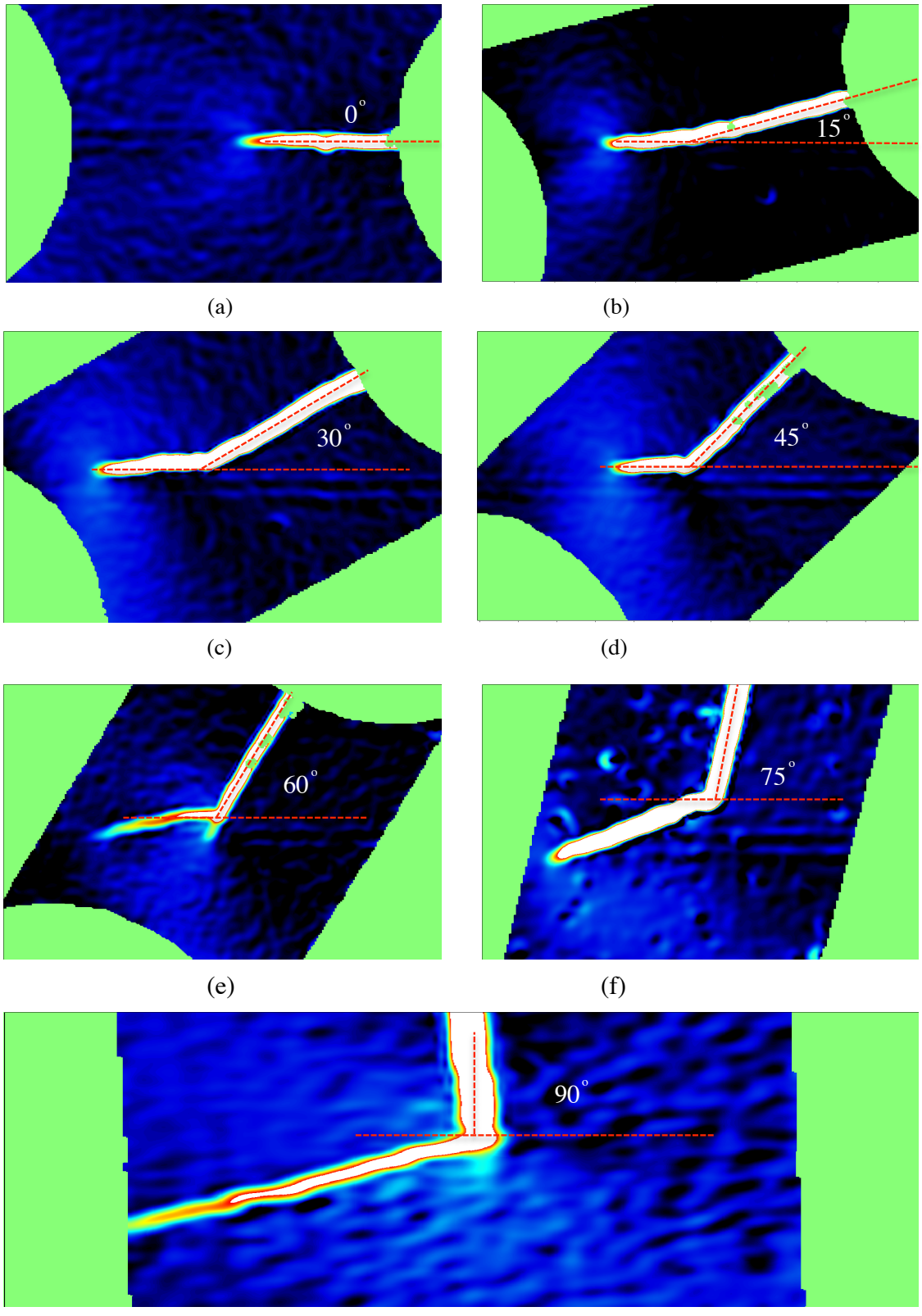

FIGURE 5.11: Crack propagation angle comparison of Perspex Arcan maximum normal strain fields. Specimens are inclined at (a) 0^o, (b) 15^o, (c) 30^o, (d) 45^o, (e) 60^o, (f) 75^o and (g) 90^o.

shear influence on the maximum principle stresses.

5.3.4 Influence of subset sizes

Figure 5.12 shows a full maximum normal strain field comparison of crack path positions when using different size subsets. The analyses were performed using Perspex CT 1 at two different instances of the test. The subset sizes and step sizes are provided for each analysis.

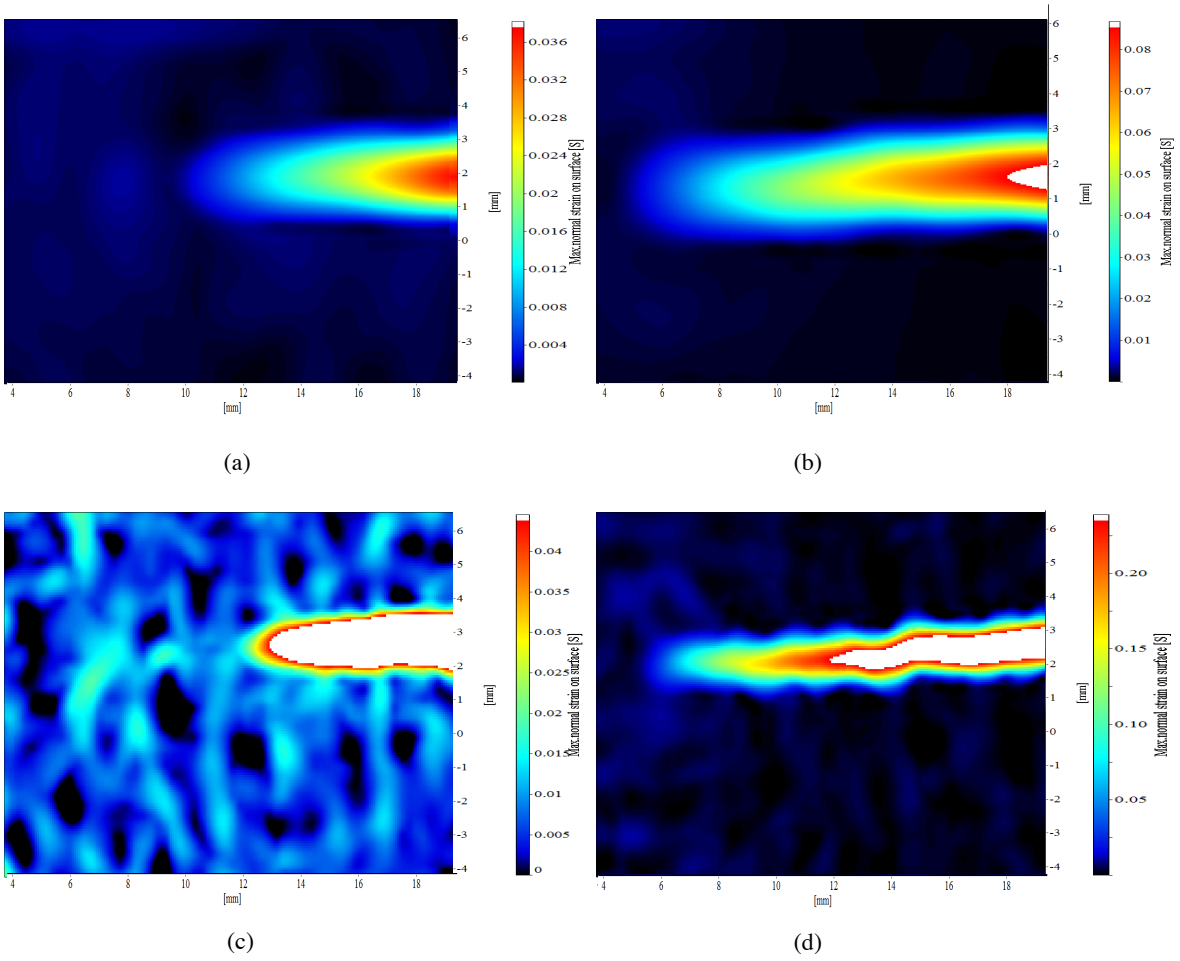

FIGURE 5.12: Comparison of crack path resolution using different subset sizes and step sizes. (a) and (b) used a subset size of 31x31 pixels and step size of 12 pixels and, (c) and (d) used a subset size of 13x13 pixels and stepsize of 4 pixels.

Figure 5.12(a) and (c) were analysed from the same image, which corresponded to the load of $P_{max} = 275$ N at the moment of crack initiation. Figure 5.12(b) and (d) corresponds to a load of $P = 192$ N. The material was regarded as failed and a prominent crack has formed.

It is evident from Figure 5.12(d) that using smaller subsets yield a more refined spatial resolution compared to using a coarser subset seen in Figure 5.12(b). However, using smaller subsets result in less accurate strain measurements due to the small amount of pixels used for correlation (Lecompte et al., 2006). The noise caused by external lighting introduces an inevitable degree of error and using smaller subsets amplifies this error. This effect is seen in the dissimilar Figure 5.12(c).

5.4 Peridynamic parameters

The following section is concerned with the peridynamic parameters that were determined from the fracture toughness results. Also, methods on how to estimate the horizon size are given from literature.

5.4.1 Critical stretch

Linear-elastic peridynamics uses a single bond failure criteria, which is governed by the critical stretch value. The hypothesis of this thesis was to use a critical energy release rate, i.e. J-integral, to determine the critical stretch. It should be noted that a linear-elastic model was used and the non-linear energy release rate is regraded as the J_{Ic} value, which is in effect a linear value. This was formulated by replacing the G_c value in Equation 2.16 for two-dimensions with J_{Ic}:

$$s = \sqrt{\frac{J_{Ic}}{(\frac{6}{\pi}\mu + \frac{16}{9\pi^2}(\kappa - 2\mu))\delta}} \tag{5.1}$$

The average J_{Ic} value from Table 5.1 was used to determine s_c for the Perspex models. The J_{Ic} values from Table 5.2 were used to initially determine s_c values for the stainless steel and alumnium models. As seen from Figure 5.4 and Figure 5.5, the J_{Ic} values correspond to crack extension, however the peridynamic models correspond to crack

initiation. Hence, the J-R-curves were utilised to determine critical stretch values from threshold J values at minimum crack extension.

It can be argued that it is an over simplification assuming a Mode I failure criteria for shear failure in peridynamics. It is further argued that using a Mode II critical energy release rate would result in more appropriate Mode II and mixed Mode failure results. This is proposed as:

$$s = \sqrt{\frac{J_{IIc}}{(\frac{6}{\pi}\mu + \frac{16}{9\pi^2}(\kappa - 2\mu))\delta}} \tag{5.2}$$

5.4.2 Bulk and shear modulus

The peridynamic simulations use the shear and bulk moduli as input and is determined as:

$$k = \frac{E}{3(1-2\nu)} \tag{5.3}$$

and,

$$\mu = \frac{E}{2(1+\nu)} \tag{5.4}$$

5.4.3 Horizon size

Horizon sizes are commonly used as $3\Delta x$ in literature, which was proposed by Silling and Bobaru (2005). However, this approach is regarded as arbitrary and there are no established experimental methods to determine the horizon. Foster et al. (2011) determined the horizon size from the approximate size of the crack tip process zone of AISI 4340 steel. The process zone size was determined by Rosakis et al. (1985) with the Spot Shadow Method. However, no motivation or comparisons in accuracy were made for this approach to determine the horizon size. The sizes of crack tip process zones for the materials used in this thesis were not determined. However, this approach would benefit from further investigation.

5.5 Discussion

In this chapter the experimental results were provided and discussed. The fracture toughness results were determined for the linear-elastic and elastic-plastic ductile materials. These parameters were regarded as the critical energy release rates required to determine the critical stretch values as input for the peridynamic models. Moreover, the J-R-curves were determined for the ductile materials. This curve describes the non-linear energy release rate during crack propagation. The J_{Ic} and J-R-curve are regarded as material properties in literature and serves as the essential bridge between the experimental methods and the peridynamic modelling for ductile failure. Hence, selected J_{Ic} and J values from this chapter are subsequently used as model input parameters in Chapter 6.

The DIC full field measurements were also provided in this chapter. It was interpreted from the full maximum normal strain fields of the ductile materials that the extensive plastic deformation ahead of the crack tips impeded accurate fracture toughness measurements from the experiments. However, this was a speculative assumption and the exact cause of discrepancy was unknown.

Further, it was shown when using smaller subset sizes in DIC analyses the crack is more accurately defined, however, there exists a trade-off between accuracy of full field measurements and accuracy of crack path resolution. Full displacement fields from the DIC measurements from selected tests were subsequently used for post-processing in Chapter 6. Also, the corresponding full maximum normal strain fields provided in this chapter are used for visual comparison between results.

Chapter 6

Peridynamic Modelling

This chapter contains two sections consisting of the peridynamic-based algorithm, peridynamic modelling and the respective results.

6.1 Introduction

The peridynamic-based algorithm is presented in this chapter. It incorporates full displacement fields containing discontinuities and reveals the crack path position using the critical energy release rate as bond failure criteria. The algorithm plots a full peridynamic damage field (Equation 2.13) as output. DIC full displacement field measurements from Chapter 4 are incorporated into the algorithm and the damage plots are compared to the full maximum normal strain fields that were presented in Chapter 5. The J_{Ic} values from the CT Perspex and ductile tests were incorporated into the code, respectively. The damage plots were compared to the corresponding DIC measurements.

The second section presents the peridynamic modelling in Mingus. The expected output from the peridynamic modelling was to determine the validity of using a non-linear energy release rate, i.e. J-integral, as input to model ductile failure. The J_{Ic} and J-R-curves from Chapter 5 were used as the non-linear energy release rate inputs required to test this hypothesis. Furthermore, the J_{Ic} results from the Perspex tests were used as input in linear-elastic models to validate the energy release rate based failure criterion proposed by Foster et al. (2011). Also, a Mode II energy release rate obtained from

literature was used to determine a critical stretch to model Mode II and mixed Mode failure, compared to using a Mode I derived critical stretch.

6.2 Peridynamic-based algorithm

A peridynamic based algorithm was developed to detect crack paths using full field displacements containing discontinuities as input. The intent was to implement DIC full displacement measurements of cracked materials to plot the peridynamic damage. The failure criteria was govern by the critical stretch, which was determined from the corresponding critical energy release rates of the material.

6.2.1 Overview of algorithm

The algorithm was developed in *MATLAB® R2012a* (2012). It was based on the discritization of full field displacements. The coordinates were regarded as material points, which were connected to distant other material points within a finite radius through bonds. Imposing the displacement field to the material points causes the connecting bonds to stretch. When a bond exceeds the critical stretch, it is regarded as irreversibly broken.

The inputs of the algorithm were the horizon size, the critical energy release rate and material properties, namely the Young's modulus of elasticity and Poisson's ratio. Also, the DIC full displacement field measurements of a cracked material were used as input. The reference subset coordinates generate the material body, as initial material points, and the deformed subset values are imposed on the material points as displacements.

The critical stretch was determined using the critical energy release rate, using Equation 5.1 of the corresponding material.

The output of the algorithm was the peridynamic damage, determined using Equation 2.13.

6.2.2 Initial work

Initial development of the algorithm included using an arbitrary critical stretch value as failure criteria to detect cracks from DIC measurements. It was capable of autonomously detecting crack path positions from DIC displacement fields of brittle materials. The initial tests used DIC displacement field measurements from Double Torsion (DT) tests on nuclear block graphite (NBG), which were performed by Becker et al. (2011). The results are shown in Figure 6.1, which were presented at SACAM (Conradie et al., 2014).

Table 6.1 gives the parameters used as input.

TABLE 6.1: Input parameters for nuclear block graphite model.

parameter	value
Horizon	1.5 Δx
Δx	0.578 mm
Critical stretch	0.055
Elasticity	11.9 GPa
Poisson's ratio	0.2

Figure 6.1 shows the bond representation of the region of analysis and a full field plot of the peridynamic damage.

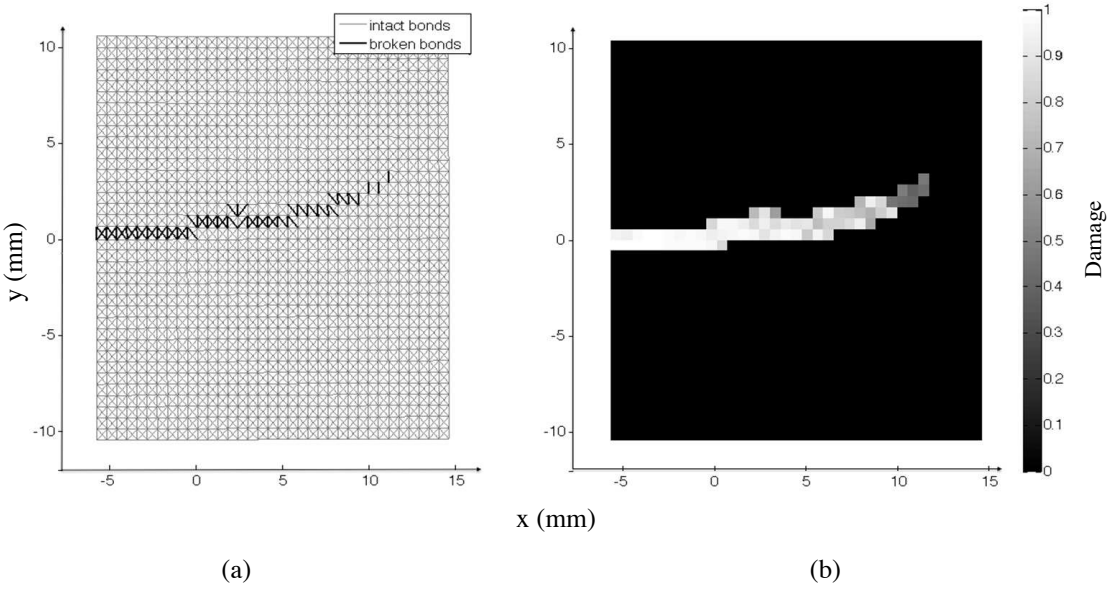

FIGURE 6.1: Bond failure and peridynamic results of cracked nuclear block graphite, (a) bond representation, (b) damage field (Conradie et al., 2014).

Figure 6.1(a) shows the material point and bond representation. The crack is indicated as broken bonds in the crack opening direction. In Figure 6.1(b) the crack path is interpreted as white shading with damage value of 1.0, the greyscale shading represents the crack tip and damage ahead of the crack tip. The black shade with zero damage value is undamaged material. Although an arbitrary value was used for the critical stretch, the results revealed an accurate crack path position and crack tip position compared to that observed in the digital image.

The algorithm showed great potential for locating the crack tip position from DIC measured displacement fields. Locating the crack tip position from digital images are often difficult. The crack widths can be less than a pixel width and undetectable through visual inspection. The precise location of the crack tip is of importance for measuring the crack length when determining accurate fracture toughness values. This was also stated by Hild and Roux (2006) when determining stress intensity factors using DIC.

6.2.3 Material models

The material models consisted of the CT Perspex, stainless steel and aluminium specimen displacement field measurements and the corresponding material parameters. The peridynamic damage fields were compared to the corresponding DIC full maximum normal strain fields.

The Perspex full field was regarded as a linear elastic material model, where the bond failure was interpreted as material cracking. The expected output was a full damage field revealing the crack path and crack tip position. This also test the hypothesis of using a linear elastic energy based failure criteria to predict cracking, as proposed by Foster et al. (2011).

The stainless steel and aluminium full fields were regarded as elastic-plastic material models. Bond failure was interpreted as plastic deformation. The expected output from the ductile materials was a full damage field that reveals plastic deformation occurring ahead of the crack. This also tests the hypothesis stated in Chapter 3 to qualitatively validate the use of a non-linear energy release rate as input to predict ductile failure using peridynamics.

6.2.4 Brittle crack damage

The Perspex CT DIC displacement fields from Section 5.3.4 were implemented in the algorithm. The purpose was to obtain the damage fields caused by cracking and compare the crack path resolution using small and large subsets. The large subsets resulted in a coarse grid spacing and the small subsets yielded a more dense fine grid spacing. Table 6.2 gives the input parameters and critical stretch values using coarse and fine grid spacing.

TABLE 6.2: Input parameters used for Perspex CT models for coarse and fine grid spacings.

Parameter	Coarse grid spacing	Fine grid spacing
Δx	0.382 mm	0.305 mm
Horizon	$3\Delta x$	$3\Delta x$
Critical energy release rate	0.750 J/mm^2	0.750 J/mm^2
Critical stretch	0.0184	0.0206
Modulus of elasticity	2.5 GPa	2.5 GPa
Poisson's ratio	0.35	0.35

Figure 6.2 shows both the full damage fields of the coarse and fine analyses.

Figure 6.2 shows a good visual representation of the crack position. It can be seen that the damaged section is the crack path and the zero damaged region is pristine material. It is evident from the results that the algorithm is capable of detecting and mapping the brittle linear-elastic crack position using the J_{Ic} and the full displacement field. The results are regarded as qualitative validation of using the critical energy release rate as bond failure criteria for brittle linear-elastic materials, as stated by Foster et al. (2011).

Silling and Bobaru (2005) regarded damage of 0.5 as a crack, where half of the bonds are required to separate to spheres. However, in Figure 6.2(d) the crack path is interpreted as the shading with value higher than 0.6. In the figure it can be seen that the damage higher than 0.6 is over the presumed crack path, where the crack tip is estimated at coordinates (1 ; 3) in Figure 6.2(d). Moreover, this allows the determination of the current crack length. Hild and Roux (2006) regarded the determination of accurate crack lengths from DIC as essential to determine accurate stress intensity factors.

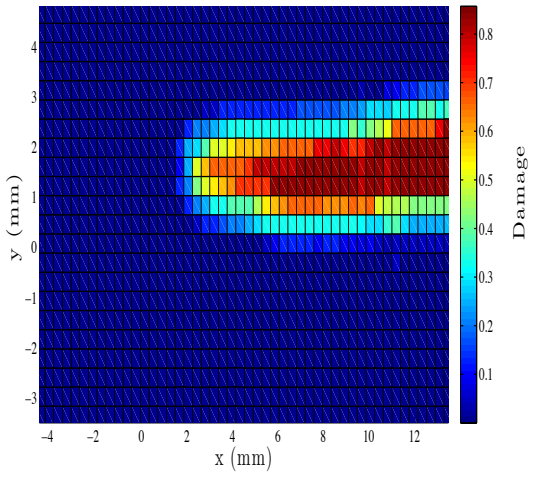

(a)

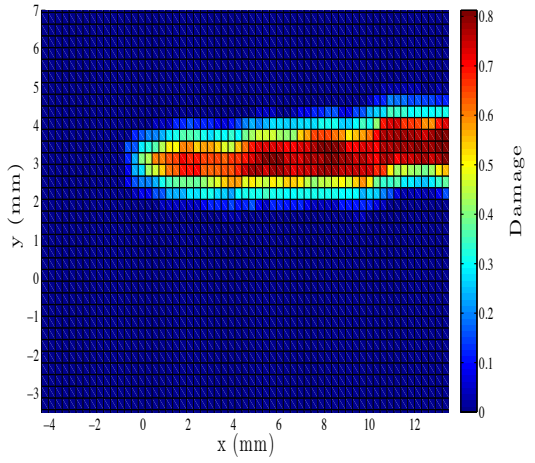

(b)

FIGURE 6.2: Peridynamic full damage fields of the cracked Perspex specimen, where the damage was computed of Perspex CT 1 at $P_{max} = 257.5$ N. (a) used a subset size of 31×31 and (b) a subset size of 13×13.

Figure 6.2(a) compared to Figure 6.2(b) shows that the crack path resolution is greatly improved when using smaller subsets. However, decreasing the subset sizes in DIC analyses decreases the precision of the displacement fields. As opposed to a refinement of the peridynamic crack damage results. Hence, there exists a trade-off between the DIC subset sizes and crack damage resolution. As mentioned before , the accuracy of the DIC displacement fields are less accurate around cracks. This introduces a certain degree of inaccuracy in the damage fields. However, this is a cause of the inherent limitations of DIC and not of the algorithm. It is recommended to implement methods found in literature to improve the DIC measurements around discontinuities such as cracks.

Nevertheless, the main focus was on predicting the crack path using the peridynamic-based algorithm from the full field displacement measurements and using the critical energy release rate as input, which was accurately achieved. It is recommended that more tests are performed on different brittle materials. Figure 6.1 show potential in applications of detecting cracks in nuclear grade graphite, which can further contribute to interests of the EPPEI program.

6.2.5 Ductile failure damage

The DIC displacement fields of CT stainless steel and aluminium tests, given in Section 5.3.1, were implemented in the algorithm. The input parameters and grid spacing of both materials are given in Table 6.3.

TABLE 6.3: Input parameters used for stainless steel and aluminium CT models.

Parameter	Stainless steel	Aluminium
Δx	0.227 mm	0.227 mm
Horizon	$3\Delta x$	$3\Delta x$
Critical energy release rate	408 J/mm^2	112 J/mm^2
Critical stretch	0.0645	0.0560
Modulus of elasticity	193 GPa	70 GPa
Poisson's ratio	0.3	0.3

Figure 6.3 shows the full damage fields of both the stainless steel and aluminium analyses.

The damage fields seen in Figure 6.3(a) and (b) are interpreted as plastic deformation, where the region of analyses were of the uncracked material surface. It can be argued that the damage fields are exaggerated and diffused, however, it was found that when using a relatively lower critical stretch value, the damage fields were excessively diffused. Therefore, the results are interpreted as qualitative validation for the hypothesis of using a non-linear critical energy release rate for determining the critical stretch. However, more analyses and work is required to further validate this assumption.

Note that J_{Ic} values were used to plot the damage fields, where the values correspond to a certain crack extension. In Figure 6.3 the plots correspond to crack extensions that were typically higher than that found at the critical energy release rate from the

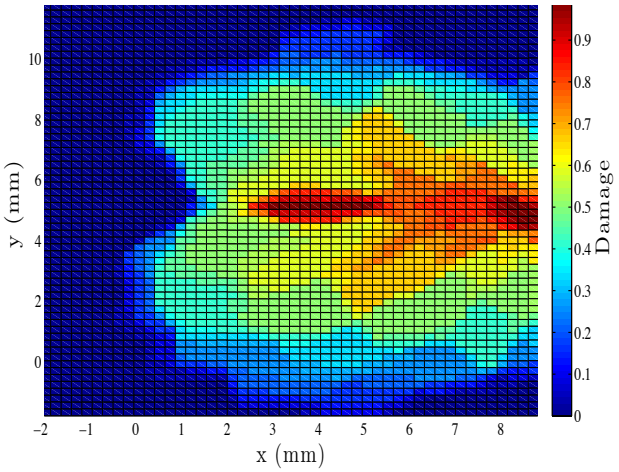

(a)

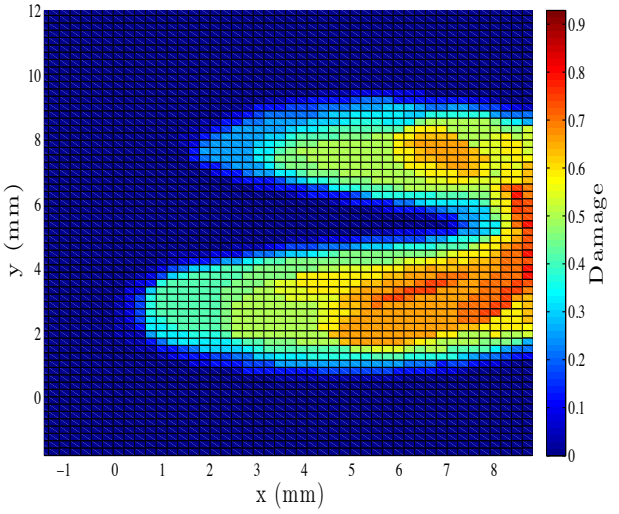

(b)

FIGURE 6.3: Peridynamic full damage fields of (a) stainless steel and (b) aluminium.

corresponding J-R-curves. It is argued that if energy release rates with corresponding crack lengths are implemented the analyses would yield more accurate damage fields. These toughened J values would typically be found on the J-R curve with relatively higher crack extension than that found at the critical crack extension. This assumption is a subject for future work.

It is evident that more work is required in interpreting bond failure for ductile materials using the peridynamic-based algorithm. A more complex damage model could be implemented, where after the bonds exceed the critical stretch, the critical stretch value effectively increases to simulate the toughening of the material. This was illustrated by

Gerstle, Sau and Silling (2007) for a microelastic peridynamic damage model.

6.3 Peridynamic modelling

The peridynamic modelling was performed with Mingus, which is an open source code developed by (Turner, 2013) from Sandia Corporation. Mingus uses state-based peridynamics (Equation 2.3) of a linear elastic peridynamic material, which was described in Section 2.2.1. Mingus requires a meshed geometry file, modelling material properties and boundary conditions as inputs. The desired outputs were the load-displacement results, where the failure loads were compared to the tests. Also, the model visualization was used to compare the simulated crack paths to that observed in the tests.

6.3.1 Model geometry and mesh

Figure 6.4 shows the geometry and mesh of the Arcan model used in Mingus. The geometry and mesh were generated in *Cubit® Version 12.2* (2010). The model was simulated in 2D, where an unit thickness was considered and plane strain conditions were assumed. The respective thickness of the specimens were subsequently multiplied with the results to obtain the failure loads to compare with the test results. The geometry dimensions were the same as the specimen design given in Appendix A.

The model was divided into three sections, as seen by the distinct shadings in Figure 6.4. This was used to define boundary conditions and material properties in Mingus.

Quadratic mesh elements were assigned to the model. The middle section was assigned a relatively fine mesh with element size of 1 mm. The supports were assigned an element size of 4 mm. Note the mesh refinement from the supports towards the middle section. This served as the mesh transition from the rigid supports towards the deformable material. Note the middle section has a rectangular mesh grid. The mesh choice was motivated for straight crack growth in Mode I.

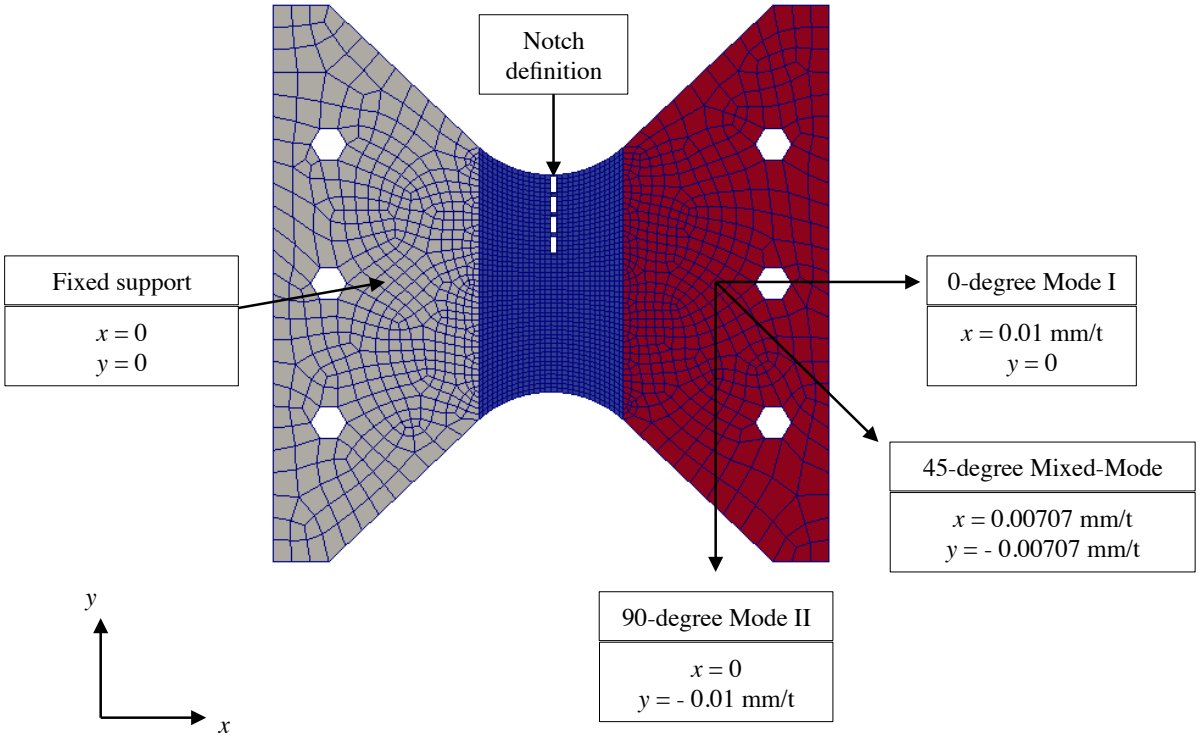

FIGURE 6.4: Arcan model indicating boundary conditions, Mode of loading and notch definition.

6.3.2 Boundary conditions

The boundary conditions are indicated in Figure 6.4. The center shaded section was regarded as the deformable material. The left section was regarded as the fixed support, where translation in the x-direction and y-direction were constrained. Through constraining the nodes against translation, effectively prevents moments about the z-axis. The arrows indicate the different loading Modes. Note the whole right section was assigned a displacement increment per timestep, t.

As seen in Figure 6.4 the Mode I model had a displacement rate of 0.01 mm/t at zero-degrees in the x-direction. The Mode II model had a displacement rate of 0.01 mm/t at 90-degrees in the negative y-direction. The mixed Mode model had a displacement rate of 0.00707 mm/t at 45-degrees in the x-direction and negative y-direction.

The precrack in the specimen was defined as a notch definition, where the length was assigned in Mingus by removing the bond interactions over the region indicated in Figure 6.4.

The supports were specified to be resistant to bond breakage and the middle section was assigned a critical stretch value. It is worth mentioning that no external criteria was assigned to where the crack should appear or propagate towards, other than the notch definition.

6.3.3 Brittle failure results

Perspex Arcan models were simulated in Mode I, Mode II and 45-degree mixed Mode loading. The input parameters for the respective models are given in Table 6.4. The parameters correspond to the formulations given in Section 2.2.1 for a linear-elastic peridynamic material. The shear and bulk moduli were determined using Equation 5.4 and Equation 5.3, respectively. Poisson's ratio was taken as 0.35 as given in Table 4.1, however Young's modulus was determined at 1.7 GPa from an analytical solution for CT specimens. Equation 4.3 and Equation 4.4 were used to determine E. Moreover, the shear modulus of the Mode II and mixed Mode models were reduced with 25%. It was found that adjusting the shear modulus within 25% captured the shear behaviour more accurately. However, this adjustment needs to be further researched and verified. Also, it was found that a horizon size of 5 yielded the most accurate failure loads in Mode I. For Mode II and mixed Mode, however, a horizon size of 4 yielded the most accurate results. Furthermore, the influence function, ω was taken as 1.0. The particular critical stretch values given in Table 6.4 were derived from the average J_{Ic} of 0.750 J/mm^2, which was used in the initial Mode I, Mode II and 45-degree mixed Mode simulations.

TABLE 6.4: Input parameters used in Perspex Arcan models, using the test Mode I derived critical stretch.

Parameter	Mode I	Mode II	45-degree mixed Mode
Notch definition length (mm)	20	20	20
Horizon	$5.0\Delta x$	$4.0\Delta x$	$4.0\Delta x$
Critical stretch	0.0106	0.0132	0.0132
Shear modulus (MPa)	629	472	472
Bulk modulus (MPa)	1888	1888	1888

The results obtained from Mingus were processed and visualised using *Paraview® 4.1.0* (n.d.). The peridynamic forces were determined by dividing the force output of the

translated support (left shaded section in Figure 6.4) with the area, (2929 mm^2) of the section and multiplying with the thickness of B = 12 mm.

Table 6.5 gives the peridynamic maximum forces compared to the respective test maximum load results, using the Mode I test derived critical stretch values. Also, the table provides a comparison of the Mode II and mixed Mode failure loads obtained from using a Mode II derived critical stretch from literature. In addition, a comparison between maximum loads were made using a calibrated critical stretch value for the 45-degree mixed Mode.

TABLE 6.5: Comparison of peridynamic and Perspex Arcan test maximum loads, for Mode I, Mode II and 45-degree mixed Mode.

Critical stretch type	s_c value	Peridynamic P_{max} (N)	Error (%)
Mode I (P_{max} = 1320 N)			
Mode I test	0.0106	1320	5.5
Mode II (P_{max} = 989 N)			
Mode I test	0.0132	603	26.9
Mode II literature	0.0162	882	10.8
45-degree mixed Mode (P_{max} = 1430 N)			
Mode I test	0.0132	989	30.8
Mode II literature	0.0162	1072	25.0
Calibrated value	0.022	1387	3.0

Table 6.5 shows that the Mode I results correlated closely with 5.5%. Also, as seen from Figure 6.5 the load-displacement curves compared accurately and the maximum displacement correlated within 7.0%. Furthermore, Figure 6.6 shows the peridynamic damage results. As seen in Figure 6.6(a) the crack initiated at 0.13 mm and has fully propagated at 0.14 mm, as seen in Figure 6.6(b), which corresponds to Figure 6.5. The damage results compared closely to the Perspex Mode I crack behaviour that was observed in the tests, where the crack initiated and rapidly propagated. These results are regarded as validation for using the critical energy release rate, i.e. J_{Ic} of brittle linear-elastic materials loaded in Mode I for determining the critical stretch.

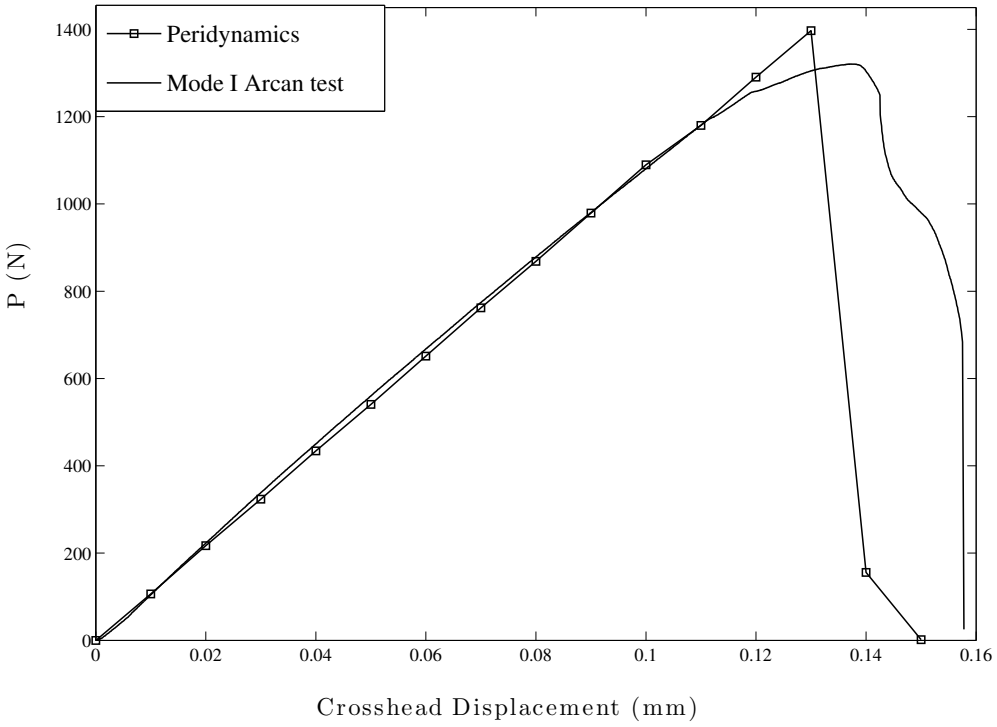

FIGURE 6.5: Mode I peridynamic load-displacement compared to Arcan test results.

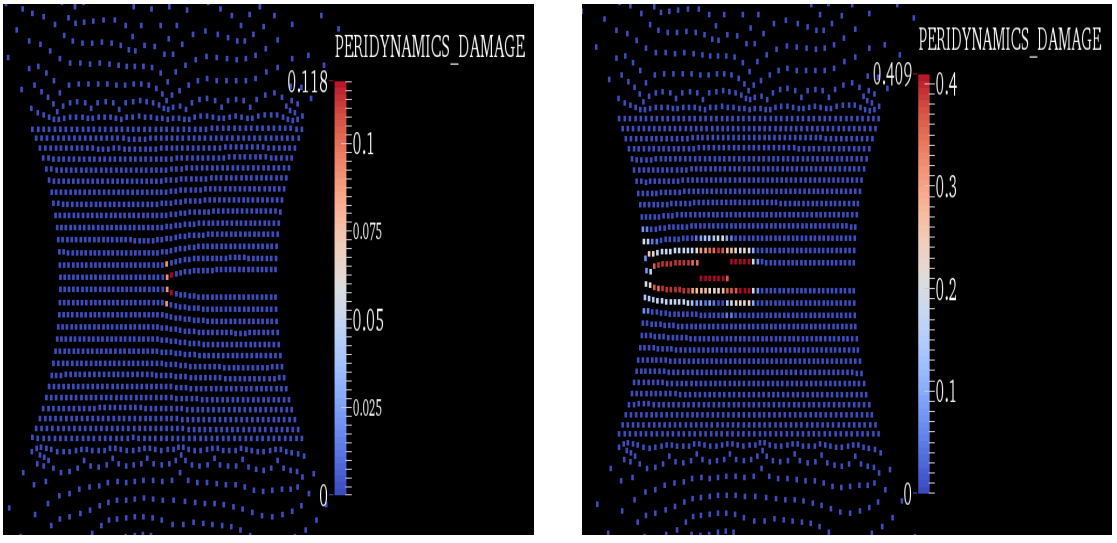

FIGURE 6.6: Mode I crack and damage results from Mingus at displacements (a) 0.13 mm and (b) 0.14 mm.

As mentioned, this approach was proposed by Foster and also validated by Madenci and Otterkus, however the same approach was followed for Mode II and mixed Mode

simulations. As seen in Table 6.5, the mixed Mode and Mode II results correlated poorly when using a Mode I derived critical stretch. Madenci and Otterkus also found discrepancies in the mixed Mode results, which was interpreted as faults with the test specimens. However, here it was argued that using a Mode I critical energy release rate to describe shear failure is a fundamentally incorrect approach. As stated in Section 2.3.8, Mode I normal failure criteria is not equal to Mode II shear failure criteria. Hence, it was proposed to implement a Mode II derived critical stretch to use as input for the Mode II and mixed Mode models. A K_{II} value of 1.479 $MPa\sqrt{m}$ obtained from tests performed by Ayatollahi et al. (2011) was used to determine the critical stretch. The stress intensity factor was converted to a J_{II} value, assuming plane strain with Equation 2.25 and the critical stretch was determined at 0.0162 with Equation 5.2 with a horizon size of 4.

Table 6.5 showed a closer correlation between the Mode II model and test failure loads using the Mode II derived critical stretch. Figure 6.7 shows the load-displacement curves. It is seen from the figure that the Mode II derived critical stretch yielded more accurate results compared to using a Mode I derived critical stretch. Furthermore, Figure 6.8 shows the peridynamic damage results obtained from Mingus. Figure 6.8(a) shows the damage initiation at 0.31 mm displacement and Figure 6.8(b) shows the damage at 0.45 mm displacement, which corresponds to Figure 6.7. It can be seen that the crack deviates similarly to the crack observed from the DIC analyses of the Mode II tests, as was shown in Figure 5.11(g). However, the simulated crack deviates from the support. It is interpreted that the boundary conditions of the model resulted in this discrepancy compared to the test. Nevertheless, it is interpreted from the results that using a Mode II critical energy release rate, i.e. J_{IIc} to model Mode II failure is a more appropriate approach. However, more research is required to validate this approach.

Figure 6.9 shows the peridynamic 45-degree mixed Mode results compared to the Arcan test. In the figure the results from using critical stretch values derived from the Mode I test, Mode II literature and a calibrated critical stretch are compared. The errors are provided in Table 6.5.

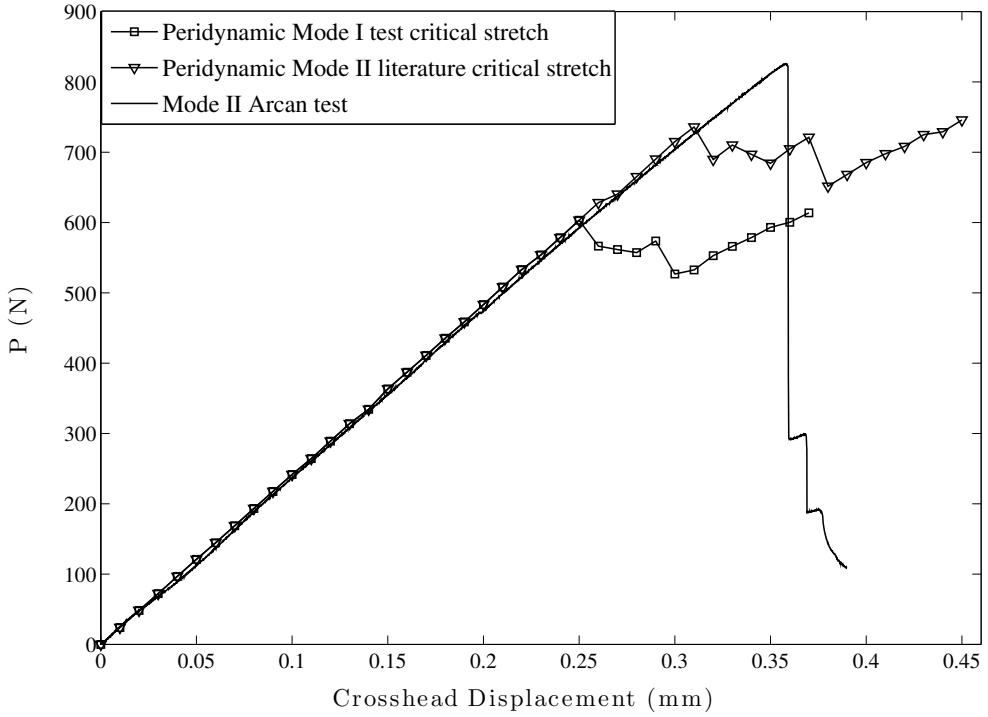

FIGURE 6.7: Mode II peridynamic load-displacement results compared to Arcan test results .

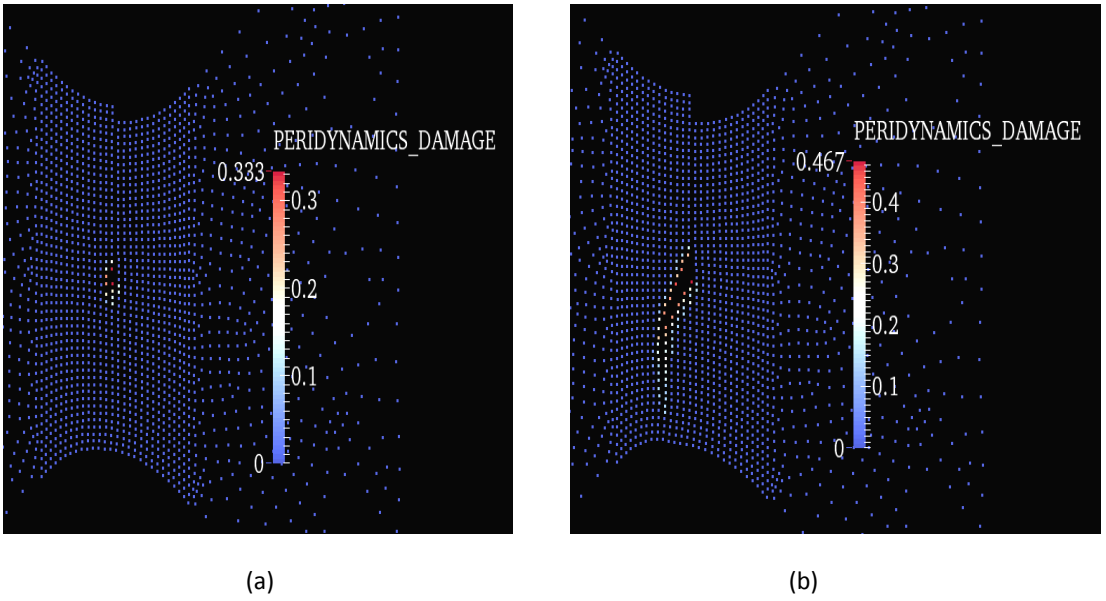

FIGURE 6.8: Mode II crack and damage results from Mingus at displacements (a) 0.31 mm and (b) 0.45 mm.

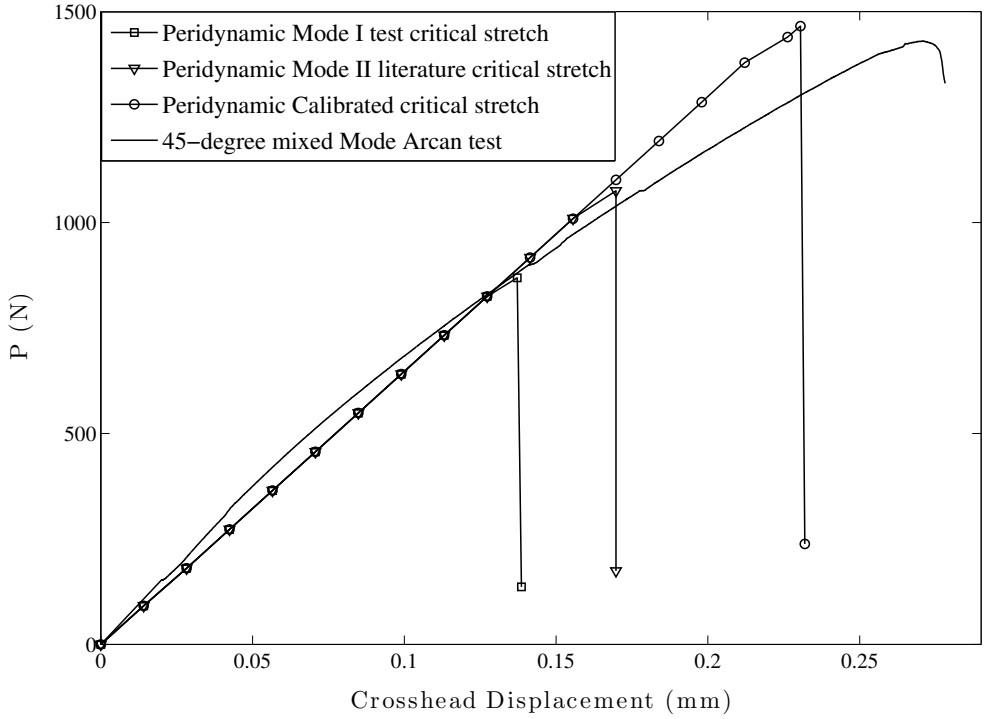

FIGURE 6.9: 45-degree mixed Mode peridynamic load-displacement compared to Arcan test results, comparing theresults of a Mode I test, Mode II literature derived and calibrated critical stretch, respectively.

In Figure 6.9 it can be seen that the results from the Mode I and Mode II derived critical stretches did not correlate closely to the test results, with 30.8% and 25.0%, respectively. It is argued that using the mixed Mode critical energy release rate to determine the critical stretch would yield more accurate results. However, this approach need to be further investigated and validated. Nevertheless, it was argued that the appropriate critical stretch could be calibrated in order to obtain accurate mixed Mode failure results. The peridynamic results are also shown in Figure 6.9 and compares closely to the test results. Note that the test results exhibited minor plastic deformation, which could be a reason of discrepancy between the calibrated model and test results.

At this point in time the discrepancies in Mode II and mixed Mode results are unclear to the author. Therefore, it is evident that more investigation is required to establish the appropriate critical energy release rate that should be used to determine the critical stretch for different Modes in order to better capture the shear behaviour and cracking in peridynamics. Despite the discrepancies for the Mode II and mixed Mode results, it was found that the approach of using a critical energy release rate based failure criterion

for predicting Mode I failure of brittle linear-elastic materials worked well and served as validation.

6.3.4 Ductile failure results

Stainless steel and aluminium Arcan specimens were modelled in Mode I using the material properties and critical stretch values determined from the respective J_{Ic} values. The input parameters and initial critical stretch values of both simulations are given in Table 6.6. The same modelling procedure was followed as for the brittle materials. However, only the failure loads were obtained and compared to the test results.

TABLE 6.6: Input parameters used in stainless steel and aluminium Arcan Mode I models

Parameter	Stainless steel	Aluminium
Notch definition length (mm)	11.5	12.0
Horizon	$4.0\Delta x$	$4.0\Delta x$
Bulk modulus (GPa)	160.83	58.33
Shear modulus (GPa)	74.23	26.92
Critical stretch, s_{Ic}	0.0266	0.0232

The critical stretch values, denoted by s_{Ic} for stainless steel and aluminium correspond to the J_{Ic} values, which is indicated in Figure 6.10. Through implementing the s_{Ic}, would test the hypothesis of using a non-linear critical energy release rate to model ductile failure.

The results using the corresponding J_{Ic} values to determine the s_{Ic} values as input are given in Table 6.7 for stainless steel and aluminium, respectively. The maximum loads of 35.4 kN for stainless steel and 9.7 kN for aluminium are respectively provided in Table 6.7. The table also shows a comparison of failure results from using critical stretch values derived from J values with less crack extension obtained from the respective J-R-curve. The J values are also indicated in Figure 6.10(a) and (b) for stainless steel and aluminium, respectively.

As seen in Table 6.7 the error between failure loads are very inaccurate when using the s_{Ic} values as input for both materials. Note s_{Ic2} was used as input, were the s_{Ic1} value

TABLE 6.7: Comparisons of using critical stretch values determined from the *J*-*R*-curves of ductile materials

Critical stretch	J values (J/mm^2)	Crack extension (mm)	Critical stretch value	Peridynamic P_{max} (kN)	Error %
			Stainless steel 304L (P_{max} = 35.4 kN)		
s_{Ic}	408	0.30	0,0266	80.9	128
s_1	140	0.025	0,0159	48.3	36
s_{th}	60	0.02	0,0106	32.1	9
			Aluminium 1200H4 (P_{max} = 9.7 kN)		
s_{Ic2}	122	0.21	0,0232	25.7	166
s_1	40	0.02	0,0139	15.2	58
s_{th}	18	0.015	0,00926	9.4	3

would yield an even larger error for the aluminium model. This large discrepancy was also found by Foster and Silling when using a critical stretch determined from K_{Ic} to model ductile failure (Boyce et al., 2011).

It is argued that a measure of material toughening has occurred in the tests, which results in more energy needed for crack extension. Implementing an energy release rate derived from an extended crack, which underwent toughening is considered not representative. In other words, stainless steel and aluminium J_{Ic} corresponds to a crack extension of 0.30 mm and 0.21 mm, respectively. The peridynamic models assume brittle linear-elasticity and the failure load is reached at crack initiation. Therefore, it would be more appropriate using a J value at threshold or with less crack extension.

Critical stretches denoted by s_{th} were determined using J values closer to threshold, indicated in Figure 6.10. The threshold crack extension for stainless steel and aluminium was regarded as 0.02 mm and 0.015 mm, respectively. Also, critical stretches denoted by s_1 were determined with J values with relatively larger crack extension to compare the difference in accuracy, as given in Table 6.7. The corresponding failure loads using the respective critical stretch values are given in Table 6.7 and are compared to the P_{max} values from the tests.

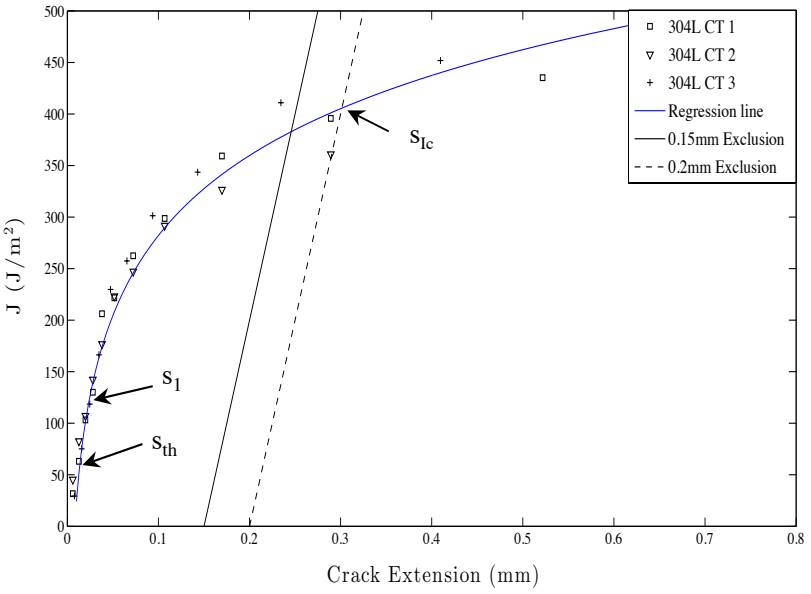

(a)

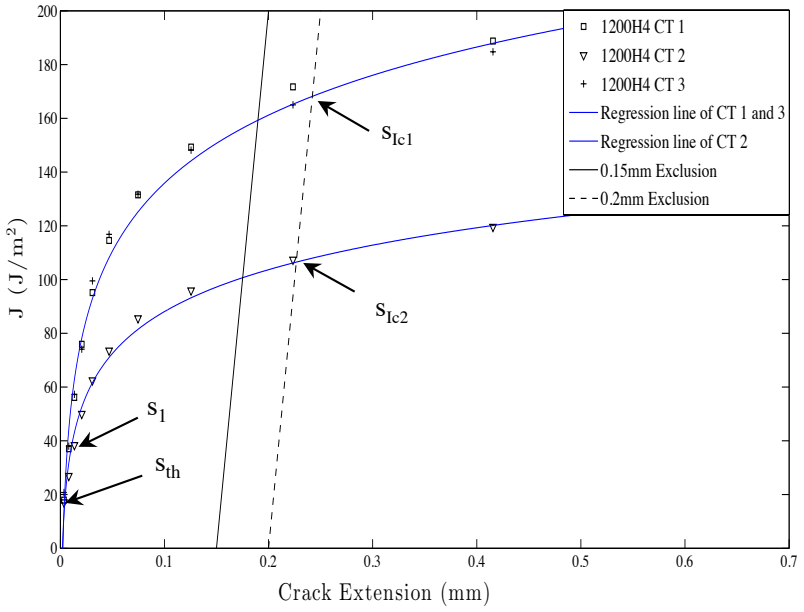

(b)

FIGURE 6.10: *J-R* curves of (a) stainless steel and (b) aluminium, where the critical stretch values given in Table 6.7 are indicated

From Table 6.7 it is seen that using critical stretch values derived from J values with less crack extension than J_{Ic} yielded improved results. The aluminium results correlated relatively well to the results within 3%. However, notice that a lower load is obtained using threshold J values closer to zero crack extension.

The failure loads found in Table 6.7 are interpreted as validation for hypothesis of using a

non-linear energy release rate determined critical stretch to predict ductile failure loads, however, the original argument of using the critical energy release rate, i.e. J_{Ic}, is not valid, as interpreted from the relatively large discrepancy in results.

Regardless of the discrepancies, the approach of using a threshold non-linear energy release rate shows potential for predicting failure loads of ductile materials. It is evident that further research is required to validate this approach and determine the reasons of discrepancy.

6.4 Discussion

In this chapter it was validated that the J_{Ic} can be used to determine the critical stretch for linear-elastic brittle materials. The relatively accurate peridynamic modelling results compared to the test failure results served as quantitative validation. The full damage field results compared to the DIC measured full maximum normal strain fields served as qualitative validation. Moreover, it was interpreted from the relatively inaccurate results that Mode II and mixed Mode failure should not be modelled using a Mode I derived critical stretch. Mode II and mixed Mode critical energy release rates would be more appropriate to determine the critical stretch for modelling the respective Modes of loading. However, this statement needs to be further investigated and validated.

Finally, it was shown that using a threshold J value with minimal crack extension as input for modelling ductile failure in peridynamics, yielded considerably more accurate results compared to using J_{Ic}. It was argued that the peridynamic models yielded a failure load at crack initiation and using an energy release rate derived from the J-R-curve with crack extension closer to threshold was more appropriate. This suggests the hypothesis of using a non-linear energy release rate to determine the critical stretch for modelling ductile failure. However, this poses a new question of what values on the J-R-curve should be used for input when modelling ductile failure in peridynamics. Moreover, it is suggested that rather than using a single value as input, the J-R-curve can be used to describe the bond behaviour for modelling ductile failure. The following Chapter 7 further discusses the salient points found in this thesis.

Chapter 7

Further Discussions and Recommendations

This chapter aims to further discuss the key findings of this thesis. Also, secondary findings from the previous chapters are reiterated and discussed. Furthermore, future work and recommendations are discussed for each specific aspect in this chapter.

7.1 Introduction

The main discussion covers the hypothesis of implementing a J-integral determined critical stretch for modelling ductile failure using peridynamics. Additionally, the validation of using the critical energy release rate based criterion for modelling brittle cracking is discussed. Concerns of using a Mode I energy release rate based failure criterion for modelling pure shear and mixed Mode failure are emphasized.

The peridynamic-based algorithm was developed to incorporate full displacement field measurements to accurately reveal crack positions in brittle materials and estimate damage caused by plastic deformation in ductile materials. The benefits and limitations of this approach are discussed. Also, the future course of development of the algorithm is given.

7.2 Non-linear energy release rate based failure criterion for ductile failure modelling

The hypothesis of this thesis was derived from the difficulties experienced by Foster and Silling in the ductile failure X-prize held by Sandia National Laboratories (Boyce et al., 2011). Here it was found that modelling failure of ductile materials is a complex problem and that there was no forthright solution for predicting the ductile failure loads. This was also found by Madenci and Oterkus (2014), which recently stated: "*For complex material behavior, there is no simple approach for determining the critical stretch or critical energy*". To address this problem, it was proposed in this work to implement a non-linear energy release rate based failure criterion, i.e. J-integral, to determine the critical stretch. The points below address the problem of determining the critical energy and the critical stretch, respectively. Also, future recommendations are given.

- The critical energy that Madenci and Oterkus mentioned was regarded as the non-linear energy release rate. This parameter was related to elastic-plastic fracture mechanics (EPFM), where the J-integral and the J-R-curve were considered. These critical energy parameters can simply be obtained from standardised ASTM tests on ductile materials. It is argued that the non-linear energy release rate, i.e. J-integral is the essential bridge between experimental fracture mechanics and determining the peridynamic critical stretch.

- In this thesis it was proposed that the critical stretch used for modelling ductile failure can be determined from a threshold J value derived from the J-R-curve. Accurate ductile failure loads were obtained when determining the critical stretch using threshold J values with minimal crack extension. It was argued that the threshold J value corresponds to crack initiation, therefore it is an appropriate input parameter for a linear-elastic peridynamic model, which yields the failure load at crack initiation. Determining the discrepancies found in failure loads and input J values are subjects of future work. Nevertheless, it was shown that using a non-linear energy release rate is a more appropriate approach for modelling ductile failure. This spans in contrasts to the supposition made by Foster et al. (2011) to use the critical non-linear energy release rate, i.e. J_{Ic}, to determine the critical stretch.

- It was stated by Foster et al. (2011) that peridynamic analysts lack in experimental context. It is proposed that the J-R-curves of alloys could be used as a guide to determine the critical stretch values for estimating ductile failure loads in peridynamics. In retrospect of the ductile failure x-prize, only the K_{Ic} value and tensile data were provided (Boyce et al., 2011). Using a Mode I linear elastic failure criterion as input restricted analysts to predict failure of a non-linear mixed Mode problem. It is projected that providing the J-R-curves of the alloys would have resulted in more accurate failure load predictions.

7.3 Critical energy release rate based failure criterion for brittle crack prediction

In this thesis it was shown that the critical energy release rate based failure criterion proposed by Foster et al. (2011) was a valid approach for determining the critical stretch for brittle linear-elastic materials. However, new research questions concerning failure Modes when modelling brittle cracking in peridynamics resulted from this thesis. The concerns of modelling different Modes of loading are emphasised and proposed solutions are given below:

- The discrepancies from Figure 3.2 were interpreted by Madenci and Oterkus as specimens lacking sharp crack tips. It was stated that the results validated the critical stretch values, even for mixed Mode simulations. However, here the results for Mode II and mixed Mode were interpreted as fundamentally inaccurate. As discussed in Sections 2.3.3 and 2.3.8, normal failure criteria (K_{Ic}) cannot be used to describe shear failure (K_{IIc}). It is argued that J_{Ic} cannot in principle be used to determine the critical stretch for Mode II or mixed Mode problems. The correlation in Mode II failure loads from Figure 3.2 between the simulations and mixed Mode tests are considered purely coincidental. Perspex is an isotropic homogeneous material and that might have contributed to the close correlation. It is argued that Mode II simulations of non-homogeneous materials would not yield accurate results using a Mode I energy failure criterion.

- It was proposed to use a Mode II derived critical stretch, using Equation 5.2, to model Mode II and mixed Mode failure. It was found that using J_{IIc} to determine

the critical stretch yielded closer correlating results, yet these were still relatively inaccurate compared to the test results. It is evident from the results that more investigation is required in establishing an appropriate critical energy release rate to determine the critical stretch to better capture the shear failure behaviour in peridynamcis.

7.4 Peridynamic-based algorithm

This section focuses on the novel peridynamic-based algorithm and discusses the benefits as well as limitations. Furthermore, future development and recommendations are given.

- The approach of using peridynamics and DIC full field measurements showed great potential for crack path mapping. Implementing the full displacement field and J_{Ic} of a cracked material revealed accurate crack path predictions. Also, the algorithm has the capability of revealing an estimate of the crack tip location, which is difficult to detect from pixel data when evaluating digital images. The knowledge of the crack tip locations is of great importance to determine the fracture toughness in further applications of fracture mechanics (Hild and Roux, 2006).

- From the damage plot results it was found that the crack damage width was broader than the crack (Figure 6.2). In reality brittle cracks are very fine and only a few pixels or less than a pixel in width. The spatial resolution of the damage field is limited to the size of the peridynamic material points. This resolution is dependent on the density of the full field measurements. A larger subset size is required for accurate displacement correlations, as found by Lecompte et al. (2006) and Pan et al. (2009), which results in a coarser peridynamic mesh. Thus, a trade-off exists between the DIC subset size and peridynamic discretisation. A large subset size yields more accurate displacement measurements and a finer material point discretisation results in a more refined representation of the crack path position and peridynamic damage evaluation.

- The inherent incapability of DIC to measure displacement of target subsets containing discontinuities introduces a further measure of inaccuracy in plotting damage. This is also unavoidable and can be solved with more advanced crack detecting

methods of DIC, such as methods developed by Poissant and Barthelat (2010) or Turner (2014).

Chapter 8

Conclusion

This thesis set out to use Digital Image Correlation (DIC) full surface field measurements and peridynamic crack predicting capabilities to characterise failure of ductile structural materials. It was found that the use of experimentally obtained energy release rate based failure criteria from fracture mechanics to determine the peridynamic critical stretch is a valid approach for predicting brittle linear-elastic failure. Also, the same approach was used for predicting ductile failure of alloys. It was found that the non-linear energy release rate criterion relates to the resistance to crack extension of a ductile material, i.e. the J-R-curve. Through standard tests the curve was determined and the critical stretch was derived from the J-R-curve. The results showed that using threshold J values with minimal crack extension to determine the critical stretch yielded relatively accurate results. It was argued that the energy release rate at crack initiation was the most appropriate input value to simulate ductile failure in peridynamics. As opposed to using the critical non-linear energy release rate, i.e. J_{Ic}. This was in disagreement to the original anticipated approach of using the J_{Ic} value as peridynamic input to model elastic-plastic failure, as stated by Boyce et al. (2011) and Foster et al. (2011). Peridynamic analysts can potentially use this approach as a guideline to model future ductile failure problems.

Although the critical energy release rate based failure criterion was validated for predicting failure of brittle linear-elastic materials in peridynamics. It was found through discrepancies in brittle linear elastic cracking results and results from Madenci and Oterkus (2014), that using Mode I failure criteria to model Mode II and mixed Mode

failure is in principle an inappropriate approach. It was proposed to use Mode II and mixed Mode energy release rate based failure criteria for the appropriate Mode of loading in the peridynamic models.

In addition, a novel peridynamic-based algorithm was further developed to accurately estimate crack growth paths using DIC full displacement field measurements from cracked brittle materials. Implementing the J_{Ic} values and displacement fields of brittle linear-elastic materials showed close correlation with the tests. It was shown that the DIC measured full field displacements naturally fitted the peridynamic material points, which allows both accurate brittle crack mapping and reveals plastic damage of ductile materials. The results also served as qualitative validation of the critical energy release rate based failure criterion as proposed by Foster et al. (2011). Furthermore, implementing the full field surface displacements of the ductile materials and the corresponding J_{Ic} values, revealed relatively accurate damage fields compared tests, which were interpreted as the plastic zones. However, the algorithm is in an early stage of development and requires further research in material failure models, in particularly for ductile behaviour.

In conclusion, it was shown in this thesis that using DIC full displacement fields and peridynamics presents a powerful tool for capturing and mapping crack damage. Also, it was shown through limited testing effort to obtain modelling material failure parameters that relatively accurate material cracking failure estimates could be obtained. Instead of using doubtful assumptions of material failure criteria, a straightforward method was followed of using the characteristic energy resistance to crack extension of ductile materials as a guideline for modelling inputs in peridynamics. Although ductile failure in general remains a complex problem to model and predict, this thesis provided a step forward in the development of fracture-modeling capabilities.

References

Amstutz, B. E., Sutton, M. A. and Dawicke, D. S. (1995), 'Experimental study of mixed mode I/II stable crack growth in thin 2024-T3 aluminum', *Fatigue and Fracture* **26**, 256–273.

Amstutz, B. E., Sutton, M. A., Dawicke, D. S. and Boone, M. L. (1997), 'Effects of mixed mode I/II loading and grain orientation on crack initiation and stable tearing in 2024-T3 aluminum', *Fatigue and Fracture* **27**, 217–224.

Anderson, T. L. (2005), *Fracture Mechanics - Fundamentals and Applications*, 3 edn, Taylor and Francis.

Arcan, M., Hashin, Z. and Voloshin, A. A. (1978), 'Method to produce uniform plane-stress states with applications to fiber-reinforced materials', *Experimental Mechanics* **28**, 141–146.

Archbold, E., Burch, J. M. and Ennos, A. E. (1970), 'Recording of in-plane surface displacement by double exposure speckle photography', *Optica Acta* **17**, 883–898.

Ashbya, M. F. and Smidmana, M. (2010), Materials for nuclear power systems, Technical Report 1.1, Engineering Department, Cambridge University, UK.

Askari, E., Bobaru, F., Lehoucq, R. B., Parks, M. L., Silling, S. A. and Weckner, O. (2008), Peridynamics for multiscale materials modeling, *in* 'Journal of Physics: Conference Series', Vol. 125.

Askari, E., Xu, J. and Silling, S. A. (2006), Peridynamic analysis of damage and failure in composites, *in* 'AIAA Aerospace Sciences Meeting and Exhibit', Vol. 44, American Institute of Aeronautics and Astronautics.

ASTM-E1820 (2011), Standard test method for measurement of fracture toughness, Technical report, American Society for Testing Materials, West Conshohocken.

ASTM-E1823 (2011), Standard terminology relating to fatigue and fracture testing, Technical report, American Society for Testing Materials, West Conshohocken.

ASTM-E23 (2007), Standard test methods for notched bar impact testing of metallic materials, Technical report, American Society for Testing Materials, West Conshohocken.

ASTM-E399 (2009), Standard test method for linear-elastic plane-strain fracture toughness kic of metallic materials, Technical report, American Society for Testing Materials, West Conshohocken.

ASTM-E647 (2011), Standard test method for measurement of fatigue crack growth rates, Technical report, American Society for Testing Materials, West Conshohocken.

Ayatollahi, M. R. and Aliha, M. R. M. (2009), 'Analysis of a new specimen for mixed mode fracture tests on brittle materials', *Engineering Fracture Mechanics* **76**, 1563–1573.

Ayatollahi, M. R., Aliha, M. R. M. and Saghafi, H. (2011), 'An improved semi-circular bend specimen for investigating mixed mode brittle fracture', *Engineering Fracture Mechanics* **78**, 110–123.

Banks-Sills, L., Arcan, M. and Bortman, Y. (1984), 'A mixed mode fracture specimen for mode II dominant deformation', *Engineering Fracture Mechanics* **20**(1), 145–157.

Bannister, A. C. (1998), *BE95 -1426, 'Determination of fracture toughness from charpy impact energy: procedure and validation'*, British Steel plc, Rotherham S60 3AR.

Becker, T. H., Marrow, T. J. and Tait, R. B. (2011), 'Damage, crack growth and fracture characteristics of nuclear grade graphite using the double torsion technique', *Journal of Nuclear Materials* **414**, 32–43.

Becker, T. H., Mostafavi, M., Tait, R. B. and Marrow, T. J. (2012), 'An approach to calculate the j-integral by digital image correlation displacement field measurement', *Fatigue and Fracture Engineering Materials and Structures* **35**(971-984).

Begley, J. A. and Landes, J. D. (1972), *The J-Integral as a fracture criterion*, American Society for Testing Materials.

Belytschko, T., Bazant, Z. P., Hyun, Y. W. and Chang, T. P. (1986), 'Strain-softening materials and finite element solutions', *Computers and Structures* **23**(2), 163–180.

Belytschko, T. and Black, T. (1999), 'Elastic crack growth in finite elements', *Int. J. Numer. Meth. Engng* **45**, 601–620.

Berfield, T. A., Patel, H. K., Shimmin, R. G., Braun, P. V., Lambros, J. and Sottos, N. R. (2006), 'Fluorescent image correlation for nanoscale deformation measurements', *Small* **2**(631-635).

Bobaru, F., Yang, M., Alves, L. F., Silling, S. A., Askari, E. and Xu, J. (2009), 'Convergence, adaptive refinement, and scaling in 1d peridynamics', *Int. J. Numer. Meth. Engng* **77**, 852–877.

Boyce, B. L., Bishop, J. E., Cordova, T., Cox, J. V., Crenshaw, T. B., Dion, K., Dowding, K., Emery, J. M., Foster, J. T., FoulkIII, J. W., Littlewood, D. J., Mota, A., Ostien, J., Robbins, J., Silling, S. A., Spencer, B. W. and Wellman, G. W. (2011), Ductile failure x-prize, Technical report, Sandia National Laboratories.

Bruck, H. A., McNeill, S. R., Sutton, M. A. and Peters, W. H. (1989), 'Digital image correlation using newton-raphson method of partial differential correction', *Experimental Mechanics* **29**, 261–267.

CES EduPack (2013).

Charpy, A. G. A. (1912), Report on impact tests and work of committee 26, *in* 'Proceedings of the Sixth Congress of the International Association for Testing Materials', New York, pp. 1–10.

Chasiotis, I. and Knauss, W. G. (2002), 'A new microtensile tester for the study of mems materials with the aid of atomic force microscopy', *Experimental Mechanics* **42**, 51–57.

Claire, D., Hild, F. and Roux, S. (2004), 'A finite element formulation to identify damage fields: the equilibrium gap method', *International Journal for Numerical Methods in Engineering* **61**, 189–208.

Conradie, J. H., Turner, D. Z. and Becker, T. H. (2014), Characterising damage in structural materials using digital image correlation and peridynamics, *in* 'South African Conference on Computational and Applied Mechanics', Vol. 9, Somerset West, South Africa.

Cubit® Version 12.2 (2010).

Dainty, J. C. (1975), *Laser specle and related phenomena*, Springer.

Dawicke, D. S. and Sutton, M. A. (1994), 'CTOA and crack-tunneling measurements in thin sheet 2024-T3 aluminum alloy', *Experimental Mechanics* **34**(4), 357–368.

Eskom EPPEI (2014), Available from: `<http://www.mateng.uct.ac.za/mateng/eppei.>`. [31 August 2014].

Foster, J. T., Silling, S. A. and Chen, W. (2011), 'An energy based failure criterion for use with peridynamic states', *Journal for Multiscale Computational Engineering* **9**(6), 675–687.

Foster, J. T., Silling, S. A. and Chen, W. W. (2009), 'Viscoplasticity using peridynamics', *Int. J. Numer. Meth. Engng* **81**, 1242–1258.

Foster, T. F. (2009), Dynamic crack initiation toughness: Experiments and peridynamic modeling, Technical report, Sandia National Laboratories, Albuquerque, NW and Livermore, CA.

Gabor, D. (1949), 'Microscopy by reconstructed wavefronts', *In Proceedings of the Royal Society* **A197**, 454–487.

Gerstle, W., Sau, N. and Aguilera, E. (2007), Micropolar peridynamic constitutive model for concrete, *in* 'SMiRT', Vol. 19.

Gerstle, W., Sau, N. and Silling, S. A. (2007), 'Peridynamic modeling of concrete structures', *Nuclear Engineering and Design* **237**, 1250–1258.

Gravouil, J. R. A., Morestin, F. and Combescure, A. (2004), 'Estimation of mixed-mode stress intensity factors using digital image correlation and an interaction integral', *International Journal of Fracture* **132**, 65–79.

Griffith, A. A. (1921), 'The phenomena of rupture and flow in solids', *Philosophical Transactions, Series A* **221**(163-198).

Ha, Y. D. and Bobaru, F. (2011), 'Characteristics of dynamic brittle fracture captured with peridynamics', *Engineering Fracture Mechanics* **78**, 1156–1168.

Hallback, N. and Nilsson, F. (1994), 'Mixed-Mode I/II fracture behaviour of an aluminium alloy', *J. Mech. Phys. Solids* **42**(9), 1345–1374.

Han, G., Sutton, M. A. and Chao, Y. J. (1994), 'A study of stationay crack tip deformation fieldsin thin sheets by computer vision', *Experimental Mechanics* **34**(2), 751–761.

Han, G., Sutton, M. A. and Chao, Y. J. (1995), 'A study of stable crack growth in thin sec specimens of 304 stainless steel', *Engineering Fracture Mechanics* **52**(3), 525–555.

Hild, F. and Roux, S. (2006), 'Measuring stress intensity factors with a camera: Integrated digital image correlation (I-DIC)', *Comptes Rendus Mechanique* **334**, 8–12.

Hillerborg, A., Modeer, M. and Petersson, P. E. (1976), 'Analysis of crack formation and crack growth in concrete by means of fracture mechanics and finite elements', *Cement and Concrete research* **6**, 773–782.

Hjelmstad, K. D. (2005), *Fundamentals of Structural Mechanics*, Vol. 2, Springer Science+Business Media.

Hosseini, S. R., Choupani, N. and Gharabaghi, A. R. M. (2008), 'Experimental estimation of mixed-mode fracture properties of steel weld', *Engineering and Technology* **2**, 527–523.

Hutchinson, J. W. (1968), 'Singular behavior at the end of a tensile crack tip in a hardening material', *Journal of the Mechanics and Physics of Solids* **16**, 13–31.

Inglis, C. E. (1913), 'Stress in a plate due to the precence of cracks and sharp corners', *Transactions of the Institute of Naval Architects* **55**, 219–241.

Irwin, G. R. (1956), 'Onset of fast crack propagation in high strength steel and aluminum alloys', *Sagamore Research Conference Proceedings* **2**, 289–305.

Irwin, G. R. (1957), 'Analysis of stress and strains near the end of a crack traversing a plate', *Journal of Applied Mechanics* **24**, 361–364.

Johnson, W. S. (1987), 'Stress analysis of cracked-lap-shear specimen', *Journal of Testing and Evaluation* **15**(6), 303–324.

Kawahashi, M. and Hirahara, H. (2002), 'Velocity and density field measurements by digital speckle method', *Opt. Laser Technol.* **32**, 575–582.

Lecompte, D., Smits, A., Bossuyt, S., Sol, H., Vantomme, J., Hemelrijck, D. V. and Habraken, A. M. (2006), 'Quality assessment of speckle patterns for digital image correlation', *Optics and Lasers in Engineering* (44), 1132–1145.

Lemaitre, J. (1971), Evaluation of dissipation and damage in metals, submitted to dynamic loading, *in* 'Proc. I.C.M.', Vol. 1, Kyoto Japan.

Lemaitre, J. (1984), 'How to use damage mechanics', *Nuclear Engineering and Design* **80**, 233–245.

Lu, H. and Cary, P. D. (2000), 'Deformation measurements by digital image correlation: Implementation of a second-order displacement gradient', *Experimental Mechanics* **42**, 393–400.

Maceka, R. W. and Silling, S. A. (2007), 'Peridynamics via finite element analysis', *Finite Elements in Analysis and Design* **43**, 1169–1178.

Madenci, E. and Oterkus, E. (2014), *Peridynamic Theory and Its Applications*, Vol. 1, Springer Science+Business Media New York.

Mallik, S. and Roblin, M. L. (1972), 'Speckle pattern interferometry applied to the study of phae objects', *Optics communications* **6**, 45–49.

Material: PMMA (n.d.), Available from: `<http://www.mit.edu/~6.777/matprops/pmma.htm>`. [27 Augustus 2014].

MATLAB® R2012a (2012).

McNeil, S. R., Peters, W. H. and Sutton, M. A. (1987), 'Estimation of stress intensity factor by digital image correlation', *Engineering Fracture Mechanics* .

Nikbakht, M. and Choupani, N. (2008), 'Fracture toughness characterization of carbon-epoxy composite using arcan specimen', *Engineering and Technology* **2**, 495–501.

O'Brien, T. K. (1984), 'Mixed-mode strain-energy-release rate effects on edge delamination of composites', *Effects of Defects in Composite Materials* pp. 125–142.

Pan, B., Qian, K., Xie, H. and Asundi, A. (2009), 'Two-dimensional digital image correlation for in-plane displacement and strain measurement: a review', *Measurement Science And Technology* .

Pan, B., Xie, H., Xu, B. and Dai, F. (2005), 'Performance of sub-pixel registration algorithms in digital image correlation', *Measurement Science And Technology* **17**, 1615–1621.

Paraview® 4.1.0 (n.d.).

Paris, P. C. and Erdogan, F. (1960), 'A critical analysis of crack propagation laws', *Journal of Basic Engineering* **85**, 528–534.

Paris, P. C., Gomez, M. P. and Anderson, W. P. (1961), 'A rational analytic theory of fatigue', *The Trend in Engineering* **13**, 9–14.

Peters, W. H. and Ranson, W. F. (1982), 'Digital imaging techniques in experimental stress anlysis', *Optical Engineering* **21**(3), 427–431.

Pijaudier-Cabot, G. and Bazant, Z. P. (1987), 'Nonlocal damage theory', *Journal of Engineering Mechanics* **113**(10), 1512–1533.

Poissant, J. and Barthelat, F. (2010), 'A novel "subset splitting" procedure for digital image correlation on discontinuous displacement fields', *Experimental Mechanics (2010) 50:353–364* .

Reeder, J. R. and Crews, J. R. (1990), 'Mixed-mode bending method for delamination tesing', *AIAA Journal* **28**(7), 1270–1276.

Rethore, J., Hild, F. and Roux, S. (2007), 'Extended digital image correlation with crack shape optimization', *International Journal for Numerical Methods in Engineering* **73**, 248–272.

Rice, J. R. (1968), 'A path independent integral and approximation analysis of strain concentrations by notches and cracks', *Journal of Applied Mechanics* **35**, 379–386.

Rice, J. R. and Rosengren, G. F. (1968), 'Plain strain deformation near a crack tip in a power-law hardening material', *Journal of the Mechanics and Physics of Solids* **16**(1-12).

Rosakis, A., Duffy, J. and Freund, L. (1985), 'The determination of dynamic fracture toughness of AISI 4340 steel by the Shadow Spot Method', *Journal of the Mechanics and Physics of Solids* **32**(6), 443–460.

Roux, S. and Hild, F. (2006), 'Stress intensity factor measurements from digital image correlation: post-processing and integrated approaches', *International Journal of Fracture* **140**, 141–157.

Roux, S. and Hild, F. (2007), 'Digital image mechanical identification (dimi)', *Experimental Mechanics* **48**, 495–508.

Roux, S., Rethore, J. and Hild, F. (2009), 'Digital image correlation and fracture: an advanced technique for estimating stress intensity factors of 2D and 3D cracks', *Journal of Physic D: Applied Physics* **42**, 1–21.

Russel, A. J. and Street, K. N. (1985), 'Moisture and temperature effects on the mixed-mode delamination fracture of unidirectional graphite/epoxy', *Delamination and Debonding of Materials* pp. 349–370.

Sabate, N. (2006), 'Measurement of residual stresses in micromachined structures in a microregion', *Appl. Phys. Lett.* **88**(071910).

Schlangen, E. and van Mier, J. G. M. (1992), 'Simple lattice model for numerical simulation of fracture of concrete materials and structures', *Materials and Structures* **25**(9), 534–542.

Schreier, H. W., Braasch, J. R. and Sutton, M. A. (1999), 'Systematic errors in digital image correlation caused by intensity interpolation', *Optical Engineering* **39**, 2915–2921.

Schreier, H. W. and Sutton, M. A. (2002), 'Systematic errors in digital image correlation due to undermatched subset shape functions', *Experimental Mechanics* **42**, 303–310.

Seleson, P., Parks, M. L., Gunzburger, M. and Lehoucq, R. B. (2009), 'Peridynamics as an upscaling of molecular dynamics', *Multiscale Model. Simul.* **8**(1), 204–227.

Silling, S. A. (2000), 'Reformulation of elasticity theory for discontinuities and long-range forces', *Journal of the Mechanics and Physics of Solids* .

Silling, S. A. and Askari, E. (2005), 'A meshfree method based on the peridynamic model of solid mechanics', *Computers and Structures* **83**, 1526–1535.

Silling, S. A. and Bobaru, F. (2005), 'Peridynamic modeling of membranes and fibers', *International Journal of Non-Linear Mechanics* **40**, 395–409.

Silling, S. A., Epton, M., Weckner, O., Xu, J. and Askari, E. (2007), 'Peridynamic states and constitutive modeling', *Journal of Elasticity 88:151-184* .

Stainless steel - Grade 304 (2014), Available from: <http://www.azom.com/properties.aspx?ArticleID=965>. [27 Augustus 2014].

Sun, Z. L., Lyons, J. S. and McNeil, S. R. (1997), 'Measuring microscopic deformations with digital image correlation', *Optics and Lasers in Engineering* **27**, 409–428.

Sutton, M. A., Cheng, M. Q., Peters, W. H., Chao, Y. J. and McNeil, S. R. (1986), 'Application of optimized digital correlation method to planar deformation analysis', *Image and Vision Computing* **4**(3), 143–150.

Sutton, M. A., Chu, T. C., Ranson, W. F. and Peters, W. H. (1985), 'Applications of digital image-correlation techniques to experimental mechanics', *Experimental Mechanics* pp. 237–238.

Sutton, M. A., Orteu, J. J. and Schreier, H. W. (2009), *Image Correlation for Shape, Motion and Deformation Measurements - Basic Concepts, Theory and Applications*, Springer Science+Business Media.

Sutton, M. A., Reynolds, A. P., Yang, B. and Taylor, R. (2003), 'Mixed mode I/II fracture of 2024-T3 friction stir welds', *Engineering Fracture Mechanics* **70**, 2215–2234.

Sutton, M. A., Walters, W. J., Peters, W. H., Ranson, W. F. and McNeil, S. R. (1983), 'Determination of displacements using an improved digital correlation method', *Image Vis Comput* .

Turner, D. Z. (2013), *Mingus*, Sandia Corporation.

Turner, D. Z. (2014), 'Peridynamics-based digital image correlation algorithm suitable for cracks and other discontinuities', *J. Eng. Mech* .

Vest, C. M. (1979), *Holographic Interferometry*, Wiley.

Wang, P., Pierron, F. and Thomsen, O. T. (2012), 'Identification of Material Parameters of PVC Foams using Digital Image Correlation and the Virtual Fields Method', *Experimental Mechanics* **53**, 1001–1015.

Wells, A. A. (1961), Unstable crack propagation in metals: cleavage and fast fracture, *in* 'Procedings of the crack propagation symposim', Vol. 1.

Westergaard, H. M. (1939), 'Bearing pressure and cracks', *Journal of Applied Mechanics* **6**, 49–53.

Zuidema, J., Veer, F. and van Kranenburg, K. (2003), Square and slant crack growth in (thin) sheets, *in* 'Proceedings of Fatigue Crack Paths'.

Appendix A

Specimen and Fixture Design Drawings